Department of Physics and Astronomy

University of Heidelberg

Master thesis

in Physics

submitted by

Dominik Stolzenburg

born in Balingen

2014

On the krypton background in the Xenon100 and Xenon1T dark matter search experiments

This Master thesis has been carried out by Dominik Stolzenburg

at the

Max Planck Institute for Nuclear Physics

under the supervision of

Prof. Dr. Manfred Lindner

On the krypton background in the XENON100 and XENON1T dark matter search experiments:

The currently running XENON100 experiment and its successor, XENON1T, use liquid xenon as target and detection material in the search for *weakly interacting massive particles*, a well motivated candidate for dark matter in our universe. As the expected signal rate is less than a couple of events per year, it is absolutely mandatory to understand and reduce the possible background contributions. The man-made and almost pure β-emitter ^{85}Kr is a very dangerous background candidate, as krypton is intrinsically present on the ppb (parts per billion level $\widehat{=}$ 10^{-9}) in commercially available xenon. Both further purification and the corresponding analytics are therefore equally important for these kind of experiments. This thesis describes two krypton in xenon measurement procedures and their impact on the understanding of the krypton background in the XENON experiments. First, a mass spectroscopic set-up using gas-chromatographic pre-separation is introduced, and the improvements in terms of stability and sensitivity down to the ppq (parts per quadrillion $\widehat{=}$ 10^{-15}) regime are highlighted. Subsequently several xenon assay results are presented: the evolution of the krypton concentration in XENON100 over a time period of more than a year is reconstructed and linked to the observed radon decay rates. Furthermore, several distillation procedures are examined, showing the high potential of cryogenic distillation for xenon purification. Thereby, a measurement of ultra pure xenon with an so far unprecedented purity is presented. Finally, a second analysis method is investigated, applying a delayed coincidence analysis to the XENON100 dark matter search data. This in-situ method is limited to the ppt (parts per trillion $\widehat{=}$ 10^{-12}) regime, but achieves very good agreements with the mass spectroscopic results and confirms its absolute calibration.

Der Krypton Untergrund in den Xenon100- und Xenon1T-Experimenten:

Das sich derzeit in Betrieb befindende XENON100-Experiment und sein Nachfolger, XENON1T, nutzen flüssig Xenon-Detektoren für den Nachweis von *Weakly Interactive Massive Particles*, ein gut motivierter Kandidat für Dunkle Materie in unserem Universum. Die erwartete Signalstärke liegt jedoch nur im Bereich von einigen Ereignissen pro Jahr, weshalb es absolut notwendig ist den möglichen Untergrund des Experiments zu identfizieren und zu reduzieren. Das Isotop ^{85}Kr ist ein radioaktiver β-Strahler und deshalb eine der gefährlichsten Untergrundquellen, da Krypton im ppb (parts per billion $\widehat{=}$ 10^{-9}) Bereich in käuflich erhältlichem Xenon vorhanden ist. Sowohl die zusätzliche Reinigung als auch die dazugehörende Analysemethode sind gleichsam bedeutend für den Erfolg der XENON-Experimente. Diese Arbeit beschreibt zwei verschiedene Krypton-in-Xenon Messverfahren und ihren Einfluss auf das Verständnis des ^{85}Kr-Untergrundes. Zunächst wird ein Aufbau bestehend aus einem Massenspektrometer in Kombination mit einem Gaschromatografischen Trennverfahren präsentiert. Dabei werden die Verbesserungen in Bezug auf Signal-Stabilität und Sensitivität bis in den ppq (parts per quadrillion $\widehat{=}$ 10^{-15}) Bereich hervorgehoben. Anschließend werden verschiedene Ergebnisse von Xenon-Proben vorgestellt: Der Verlauf der Krypton-Konzentration im XENON100-Experiment über eine Zeitspanne von über einem Jahr wird rekonstruiert und eine Verbindung zur beobachtenen Radonzerfallsrate wird hergestellt. Darüber hinaus werden mehrere Destillationsvorgänge untersucht, die das Potential von cryogener Destillation als Xenonreinigung aufzeigen. Dabei wird auch die Messung einer Probe mit noch nie zuvor erreichten Sauberkeit vorgestellt. Abschließend wird noch ein zweites Analyseverfahren eingeführt, das auf den Daten des XENON100-Experiments basiert. Diese Methode sucht nach ^{85}Kr-Zerfällen mit besonderer Signatur und ist auf den ppt (parts per trillion $\widehat{=}$ 10^{-12}) Bereich limitiert. Sie erreicht jedoch eine sehr gute Übereinstimmung mit den Ergebnissen des Massenspektrometers und bestätigt dessen absolute Kalibration.

Contents

1. Introduction

The question of "What makes up the universe?" is one of the oldest questions in science. During the long history of physics our understanding of the basic constituents of the universe changed several times. Up to now the Standard Model of particle physics describes the fundamental parts of ordinary matter up to an unprecedented precision. It explains the structure of protons and neutrons as well as the interactions inside an atom. The success of the Standard Model in subatomic physics is one of the biggest milestones in physics.

But looking at different scales, the above question cannot be answered that easily. There is very strong astrophysical and cosmological evidence that only a small fraction of our universe is based on matter which can be described by the Standard Model. Stars, intergalactic plasma and black holes consist of the building stones of the Standard Model, but only make up 20 % of the mass observed in the universe. The other 80 % are called *dark matter*, influencing the gravitational behavior of huge objects, such as galaxies, galaxy clusters or even the impressive afterglow of the Big Bang, the *Cosmic Microwave Background*. It is called dark, because its true nature is simply not known, but only its property of not emitting light. It remains dark for the knowledge of physics so far.

Newton's and Einstein's laws of gravity could be redesigned completely in order to explain the mass discrepancies observed on many scales in our universe. But the best motivated approach for the problem of missing mass in our universe comes from particle physics. If there is physics beyond the Standard Model, it would most probably provide a particle candidate which could be dark matter.

There are manifold ideas how to proof this conjunction of cosmology and particle physics. Complementary to searches for new physics at the LHC, direct dark matter detection experiments aim for the proof of dark matter particles interacting with our ordinary matter on earth. This Master thesis is carried out in the context of the dark matter direct detection experiments XENON100 and XENON1T, using liquid xenon as a target for dark matter particles.

One of the main challenges for these experiments are the predicted very low interaction rates of such dark matter particles. Therefore background suppression and event selection are very important for a direct detection of particle-like dark matter. In the case of the XENON experiments, the man-made radioactive isotope ^{85}Kr is one of the most dangerous background sources. It is present in xenon on the trace level, and therefore both purification and the corresponding possibility of quantifying such trace amounts of krypton in xenon are

mandatory.

In chapter 2 an introduction into the evidences for dark matter and into the XENON experiments is given, setting the framework of this thesis. Chapter 3 deals with the external monitoring of the ^{85}Kr background with a rare gas mass spectroscopic set-up (RGMS). It focuses on the improvement in sensitivity achieved for the upcoming XENON1T experiment. In chapter 4 results of xenon assay with this set-up are discussed. It presents the great impact krypton measurements can have on the experimental operations, including the detection of tiny air leaks, background predictions for a science run and improvements on the purification procedures. It concludes with the so far purest xenon sample measured in regard of krypton concentrations. Finally, chapter 5 introduces a different approach of quantifying krypton amounts: an in-situ method which uses the available XENON100 datasets and confirms the mass spectroscopic results. A comparison of the two analytics methods together with a summary of the great improvements in xenon purity achieved over time due to RGMS measurements is given in chapter 6.

2. Dark matter and the XENON direct detection experiments

Classical astronomy dealt with the prediction of trajectories of astronomical bodies, mainly of planets, stars and galaxies. Newton's and later on Einstein's theories of gravity had overwhelming success in making such predictions. But several observations during the 20^{th} century indicated that these theories only hold if there is way more non-luminous matter in our universe, so called dark matter. These astrophysical evidences are pointed out in more detail in section 2.1. A possible solution to this problem might be *Weakly Interactive Massive Particles* (WIMPs) which arise in many theories beyond the Standard Model of particle physics. Together with possible detection techniques, this is explained in section 2.2. Afterwards, in section 2.3, the XENON project is presented, introducing the two dark matter search experiments XENON100 and XENON1T, the former currently one of the leading experiments in the field of direct dark matter detection and the latter designed for taking data from 2015 on. The chapter finishes in section 2.4 with a focus on one of the most challenging background sources in the XENON project: the radioactive isotope ^{85}Kr, which is the main topic of this work.

2.1. Cosmological evidence for dark matter

It was Fritz Zwicky in 1933 who introduced the idea of a large non-luminous but massive amount of matter in our universe [1]. He observed the velocity dispersion of galaxies in the Coma cluster and found, that the galaxies were moving much faster than expected. One way to explain his observations was the introduction of a huge amount of non-luminous but gravitating matter. That however implied a mass to light ratio much larger than expected from the surrounding of our solar system.

The idea of dark matter gained much more attention as possible solution of another problem at a different scale. Rubin, Thonnard and Ford measured the rotation curves of different galaxies in 1978, i.e. they measured the velocities of stars at different distances to the galactic center [2]. From classical dynamics one would expect

$$v_{rot}(r) = \sqrt{\frac{GM(r)}{r}} \, . \tag{2.1}$$

As the integrated mass distribution $M(r)$ should be constant for large r outside of the luminous disk of the galaxy, a $r^{-1/2}$ dependence is expected for the outer stars of a galaxy. However, the measurement of a variety of galaxy rotation curves $v_{rot}(r)$ showed a non declining behavior for large r. This can be explained by adding a dark matter halo to the mass distribution of the galaxy. Figure 2.1 shows an example of such a rotation curve as measured nowadays for a variety of different galaxies.

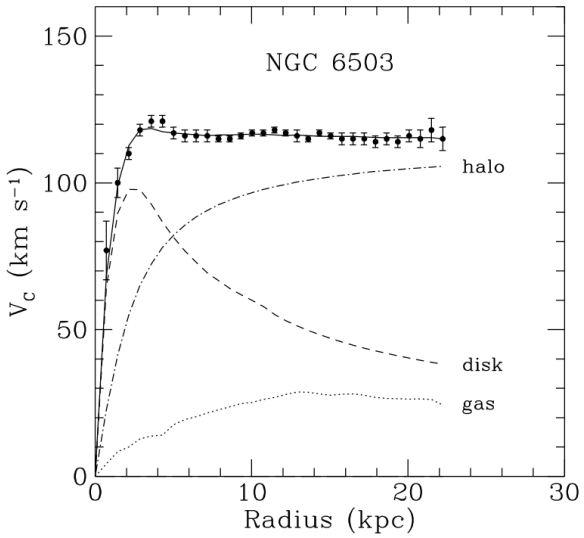

Figure 2.1.: The rotation curve of NGC 6503. The different contributions of luminous matter, gaseous matter and dark matter are shown as well. Figure taken from [3].

Another very impressive evidence for dark matter comes from gravitational lensing. In 1911 Einstein proposed that light gets deflected in strong gravitational fields [4]. This implies that the image of an astronomical source located beyond a very large gravitational potential will show strong distortions for an earthbound observer. This effect, very similar to deviation of light through an optical lens, was first observed in 1919 [5] and called gravitational lensing. If the distance to the gravitational potential is known, the mass of the lens can be inferred from the observed distortion.

It was again Zwicky who proposed to use gravitational lensing for the determination of the amount of dark matter in galaxy clusters [6]. One of the most demonstrative examples of mass discrepancies between the determination by gravitational lensing and the estimation of the luminous amount of matter is the so called Bullet-Cluster. The mass distributions of two colliding galaxy clusters were inferred from gravitational lensing. They do not match the distribution of the hot plasma, observed in the X-ray regime with the Chandra Telescope [7]. As the plasma is the dominant baryonic component of such colliding galaxy clusters, the discrepancy shown in Figure 2.2 can only be explained by dark matter shifting the center of gravity due to its collisionless character.

Astronomical results confirmed the existence of dark matter on many scales, but the de-

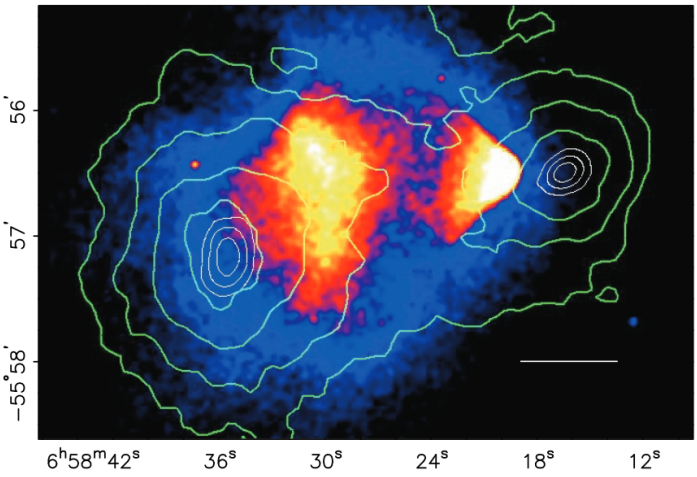

Figure 2.2.: The Bullet-Cluster 1E0657-558. The colored part represents an image of the x-ray emission from visible matter, the yellow contours show the total mass distribution inferred from gravitational lensing [7].

termination of its absolute abundance got only possible with the discovery of the *Cosmic Microwave Background* (CMB) by Penzias and Wilson in 1965. At about 400 000 years after the Big Bang photons decoupled from matter as hydrogen atoms were formed and most part of the universe got uncharged and therefore transparent. Today these photons are strongly redshifted and follow a blackbody spectrum with $T \sim 2.7$ K [8]. Various experiments measured the temperature anisotropies of the CMB. Up to now, the Planck measurement, published in 2013, is the most current and accurate one [9]. The CMB map is shown in Figure 2.3 (left).

Of big interest is the expansion of the CMB map into spherical harmonics, the so called power spectrum, which is as well shown in Figure 2.3 (right). Important cosmological parameters such as the relic abundance of dark matter in our universe, Ω_{DM}, can be inferred from the height and position of the first acoustic peaks in the power spectrum. Within the current and most favored *Lambda Cold Dark Matter* (ΛCDM) model a fit to the Planck result yields $\Omega_{DM} \sim 26$ % [10].

Directly linked to the structure of the CMB and the amount of dark matter present in our universe, is the question of structure formation. The large-scale structure of our universe is indeed coupled to the density fluctuations of the CMB as it can be demonstrated by computer simulations. It is one of the most impressive evidences for cold dark matter, that only its presence can reproduce the nowadays observed large-scale structure within these simulations [11].

Cosmology indicates that there is more massive but non-luminous matter. We can even estimate the absolute relic abundance of dark matter in our universe, but there is one keystone missing. What is dark matter? One astrophysical solution for dark matter halos of galaxies would be *Massive Compact Halo Objects* (MACHOs), which could be giant gas planets or small black holes. But in recent studies they are not abundant enough to explain dark matter

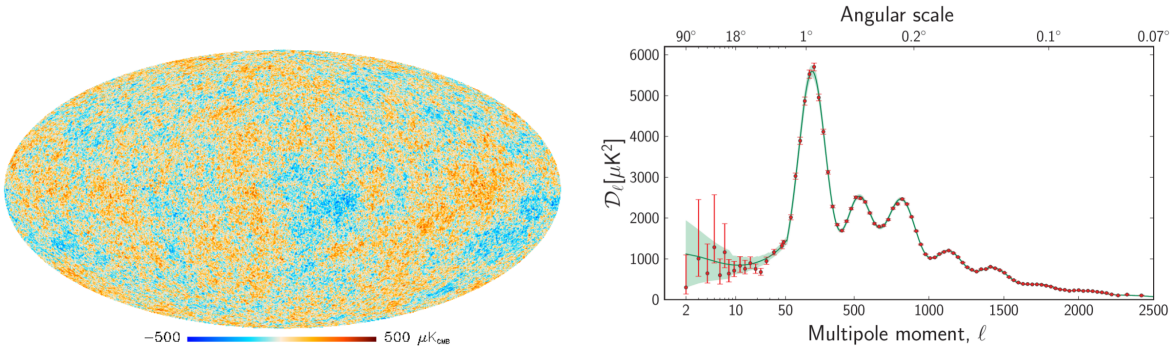

Figure 2.3.: (Left) CMB map published by the Planck collaboration [9] and (right) the expansion into spherical harmonics of the CMB map of the Planck experiment and the fitted 6-parametric ΛCDM model [10].

halos of galaxies [12]. Another solution are the so called *Modified Newtonian Dynamics* (MOND), which abandon our known laws of gravity and modify them in order to explain the observed mass discrepancies [13]. But it is not so easy to implement the dark matter problem on all known scales with a modification of the laws of gravity only. Particle physics might have a simpler solution to the question of the origin of dark matter. This will be described in the next section.

2.2. Particle dark matter and direct detection

A particle, neither interacting electromagnetically nor strongly, but with the property of being massive, could easily explain dark matter. It would, for example, show the collisionless character needed for the observation of the Bullet-Cluster phenomena. In the Standard Model of particle physics, one such particle is well known: the neutrino. But there are a few problems with neutrinos as dark matter candidates: due to their low mass neutrinos are highly relativistic particles. As such hot dark matter particles they would erase local density anisotropies and therefore prevent the formation of small scale structures in our universe [14].

There exist already many theories beyond the Standard Model in order to face remaining problems such as neutrino mass or matter-antimatter asymmetry. In many of them new particles arise with the properties of being massive, only weakly interacting and stable. This class of particles is generally referred to as *Weakly Interactive Massive Particles* (WIMPs).

Furthermore, such WIMPs naturally are produced at the right abundance to match the observed density of dark matter in our universe today. The hot dense plasma after the Big Bang provides a system in thermal equilibrium, following a Boltzmann energy distribution. WIMP production and annihilation reactions from and into Standard Model particles occur likewise. As the universe is cooling down, not enough energy remains for WIMP production and the annihilation process begins to dominate. Once the particle density drops below a

critical value due to the increasing expansion rate of the universe, it becomes unlikely for two dark matter particles to meet and to annihilate. Therefore the WIMPs "freeze-out" from the thermal medium. The relic density of WIMPs can then be calculated according to [15] with the simple equation

$$\Omega h^2 \approx \frac{3 \cdot 10^{-27} \mathrm{cm}^3\,\mathrm{s}^{-1}}{\langle \sigma_{ann}\, v \rangle} \,. \tag{2.2}$$

As it is obvious, higher cross-sections for the annihilation σ_{ann} lead to a lower relic density, which is illustrated in Figure 2.4. It is very compelling, that by plugging in typical cross-sections for weak interactions, the calculated relic density from CMB fluctuations is reproduced. An input coming from particle physics creates the desired matching with cosmology, which is called the WIMP miracle.

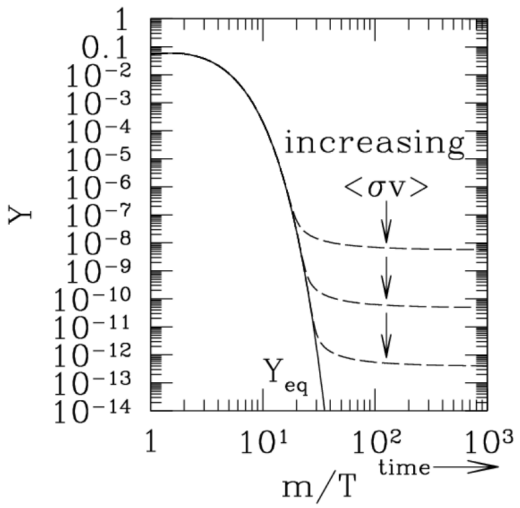

Figure 2.4.: Evolution of the dark matter number density in the early universe as function of m/T, which is proportional to the time after the Big Bang. A higher annihilation cross-section leads to a smaller relic abundance [15].

Particle physics therefore offers a solution to a cosmological problem with the possibility of being tested experimentally. Particles interacting on typical weak cross-sections could be directly detected through their elastic scattering off atomic nuclei and the measurement of their recoil energy. This can be understood by looking at equation (2.3) from [16]. It describes the expected differential event rate $\frac{\mathrm{d}R}{\mathrm{d}E_R}$ of such interactions with an earthbound target. The rate depends on several astrophysical and particle physics input parameters and is usually expressed in units of events/keV/kg/day generally referred to as *differential rate unit* (DRU)

$$\frac{\mathrm{d}R}{\mathrm{d}E_R} = \frac{\rho_\chi}{m_\chi m_N} \int_{v_{min}}^{v_{esc}} v f\,(v)\, \frac{\mathrm{d}\sigma_{WN}}{\mathrm{d}E_R}\,(v, E_R)\,\mathrm{d}v \,. \tag{2.3}$$

Necessary astrophysical parameters are the dark matter density ρ_χ, the velocity distribution $f\,(v)$ in the galactic region close to our solar system and the galactic escape velocity v_{esc}

for dark matter particles. Standard assumptions are made in order to compare the results of different direct dark matter detection experiments: a maxwellian velocity distribution is assumed and ρ_χ is set to $\sim 0.3\,\mathrm{GeV/cm^3}$ as supported by recent results [17]. $v_{esc} = (544 \pm 50)$ km/s is known from measurements [18]. However, ρ_χ and $f(v)$ are strongly model dependent, for example the velocity distribution is not assumed to be isotropic but tri-axial and anisotropic in more complex models [19].

There is also some particle physics input on the expected event rate. First the lower bound of the integration is the minimal velocity $v_{min} = \sqrt{(m_N E_R)/(2\mu^2)}$ with μ the reduced mass of the WIMP nucleon system. v_{min} is needed for a recoil of energy E_R in the case of maximum energy transfer by 180° backscattering. The differential cross-section of the WIMP scattering $\frac{\mathrm{d}\sigma_{WN}}{\mathrm{d}E_R}$ is split up into a spin-dependent $\frac{\mathrm{d}\sigma_{SD}}{\mathrm{d}E_R}$ (axial-vector coupling) and a spin-independent $\frac{\mathrm{d}\sigma_{SI}}{\mathrm{d}E_R}$ part (scalar and vector couplings). Focusing on the spin-independent part, this is parametrized into a form factor $F(E_R)$ accounting for the single nucleons making up the nucleus and the cross-section of the WIMP proton coupling $\sigma_{\chi p}^{SI}$ (assuming proton and neutron coupling approximately to be equal).

Together with equation (2.3) the expected event rate is computed by equation (2.4), showing the dependence of the expected recoil spectrum

$$\frac{\mathrm{d}R}{\mathrm{d}E_R} = \frac{\rho_\chi A^2}{2\mu_p^2 m_\chi} F^2(E_R)\,\sigma_{\chi p}^{SI} \int_{v_{min}}^{v_{esc}} \frac{f(v)}{v}\mathrm{d}v\ . \tag{2.4}$$

The overall shape of the spectrum will be exponentially decreasing with increasing recoil energies. This decrease originates from the loss of coherence and thus a decreasing nuclear form factor $F(E_R)$ and the decreasing velocity integral, as for higher recoil energies less dark matter particles have the sufficient velocities. Moreover, the total event rate scales with the squared atomic mass number A^2, but in contrast the form factor decreases faster for nuclei with higher mass. These effects result in different spectra for different possible target materials, as shown in Figure 2.5.

Having understood the expected signal of WIMPs scattering off nuclei, a few conclusions for direct detection experiments can be drawn immediately: the exponentially falling event rate requires detectors with a low energy threshold to exploit as much as possible of the expected recoil spectrum. Very challenging is the expected low total event rate, even more if it is considered that recoil energies in the order of a few keV already occur naturally in most materials.

Most dominant background sources are either nuclear recoils of neutrons or electronic recoils of γ and β particles. The former background type originates from free neutrons, produced in fission- or (α, n)-reactions induced by natural radioactivity processes or by cosmic ray activation. This can be suppressed by going deep underground in order to reduce the cosmic ray muon flux inducing such fission reactions to a negligible level. The latter background type

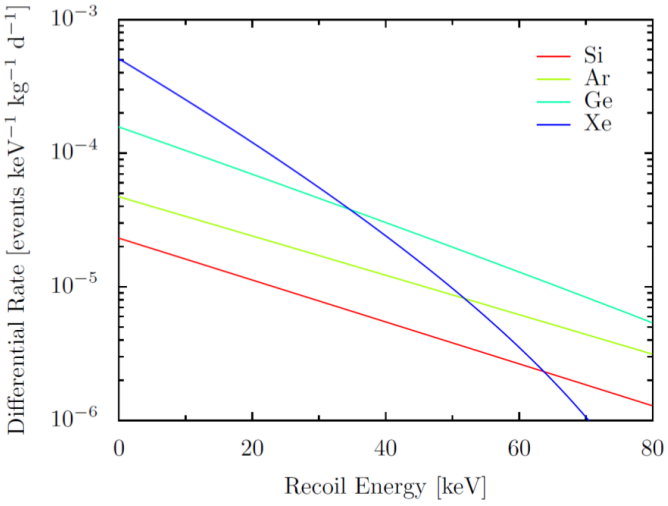

Figure 2.5.: Expected event rates of WIMP scattering for different target materials. m_χ = 100 GeV and $\sigma_{\chi p}^{SI} = 10^{-44}$ cm^2 are assumed. The total event rate is higher for heavier elements due to the scaling with A^2, but as seen for xenon, the nuclear form factor induces a quick decrease in event rate for increasing recoil energies. Figure taken from [20].

is produced in radioactive decays of naturally abundant radioactive isotopes. Mostly these radioactive decays come from the subsequent decay chains of the very long-lived primordial isotopes ^{238}U, ^{235}U, ^{232}Th and ^{40}K or from man-made radioactive isotopes like ^{137}Cs, ^{60}Co or very important in the context of this work ^{85}Kr. A strong reduction of this natural radioactivity background is one of the main challenges of experiments aiming for the direct detection of dark matter. It is usually faced with several approaches: reduction of initial contaminations, efficient shielding techniques, further cleaning processes and discrimination between different event types.

Different experimental techniques are accessible in order to detect the energy deposited in the target material. The recoil energy after a WIMP or a naturally occurring interaction is manifested in three excitation channels: ionization, scintillation and heat. These excitation channels can be read out by different detection techniques. Moreover, a combination of the readout of several channels at the same time opens the possibility of background discrimination: the ratio of the different excitation modes depends on the dE/dx and thus on the particle type.

Under several different approaches one of the most popular techniques is the use of liquid noble gas detectors. They are operated at cryogenic temperatures in order to achieve a low energy threshold by avoiding thermal noise effects and offer the possibility of reading out ionization and scintillation signals, benefiting from additional background discrimination. Stable operating conditions can be achieved as the technique is rather well known. Together with the advantage of easily scaling up the target masses, these kind of direct dark matter detection experiments are the most successful of recent years. A nice overview is given in [21].

2.3. The XENON experiments and their challenges

The XENON project uses *liquid xenon* (LXe) as target and detection material with the design of *time projection chambers* (TPCs) in a phased approach. The XENON10 detector was a first prototype of a LXe dark matter experiment operated between 2006-2007 by the XENON collaboration [22]. Installed at the *Gran Sasso Underground Laboratory* (LNGS), Italy, it benefited from 3 600 *meter water equivalent* (m.w.e.) rock shielding against background from cosmic radiation. At the same site the XENON100 detector [23] was set up and commissioned in 2009. It showed the scalability of the LXe dual-phase TPC principle to higher masses (from 10 kg to 100 kg LXe target) and was operated at improved background conditions of a factor of ~ 100. This led to first results of a 100 live-days run in 2011 [24] and another 225 live-days run result [25], which set the most stringent limits for high WIMP masses in direct dark matter searches over a long period of time. At the time of writing, the experiment is still taking data and offers the possibility to test more sophisticated dark matter models due to the excellent understanding of the detector response. The *Large Underground Xenon* (LUX) experiment confirmed and improved these results with the same detection principle but higher target mass and lower background [26]. The next step for the XENON project is the development of the first ton-scale LXe experiment, XENON1T. It will use in total more than 3 tons of LXe and benefit from improved background conditions by another factor of ~ 100. Its design goal is to test WIMP nucleon scattering cross-sections of $\sigma_{SI} = 2 \cdot 10^{-47}$ cm^2 for WIMP masses of $M_\chi = 50$ GeV, showing the feasibility of ton-scale liquid noble gas experiments. The infrastructure of XENON1T is built in such a way that the TPC can be easily upgraded. This will then facilitate XENONnT by scaling the TPC towards ~ 6 tons of LXe.

2.3.1. The XENON detection principle: a dual-phase LXe TPC

The underlying dark matter detector principle of the XENON project is a dual-phase LXe TPC. The LXe is contained in a stainless steel vessel with an inner cylindrical chamber. A liquid-gas interface can be maintained below the top of this chamber by pressurizing it with a constant xenon gas stream like in a diving-bell [23].

LXe is a good radiation detection material due to its scintillation and ionization response to incident charged particles, neutrons or γ rays with the additional advantage of different sharing of these excitation channels for different types of interactions [27]. The readout of these two excitation channels can be done with a TPC as shown schematically in Figure 2.6: the prompt scintillation light, called S1, is observed by two arrays of *photomultiplier tubes* (PMTs), one installed at the bottom of the TPC immersed in the LXe and one at the top surrounded by *gaseous xenon* (GXe). A high fraction of the S1 signal is detected by the bottom array due to the high internal reflection of the scintillation light at the liquid-gas interface.

The electrons created by ionization of the LXe due to an incident particle are collected by applied electrical fields. A homogeneous drift field between the cathode grid at the bottom of the TPC and the grounded gate grid below the liquid-gas interface of $\sim$530 V/cm drifts the electrons upwards. At the liquid-gas interface they are extracted and accelerated by a stronger extraction field $\sim$10 kV/cm created between the grounded gate grid and the anode grid placed slightly above the liquid-gas interface. Proportional scintillation is produced in the GXe [28], generally referred to as S2. This scintillation light is detected by the same PMT arrays giving the possibility of reconstructing the position of the interaction vertex: the time difference between the prompt scintillation light S1 and the secondary scintillation light S2 can be translated by the constant drift velocity of electrons in the homogeneous drift field into the z-position of the interaction vertex inside the TPC. The (x, y)-position is inferred from the hit pattern of the S2 signal at the top PMT array. It is located very close to the origin of the secondary scintillation light and shows therefore distinct patterns for different event locations. Resolution in the mm regime is achieved for all three spatial coordinates [23].

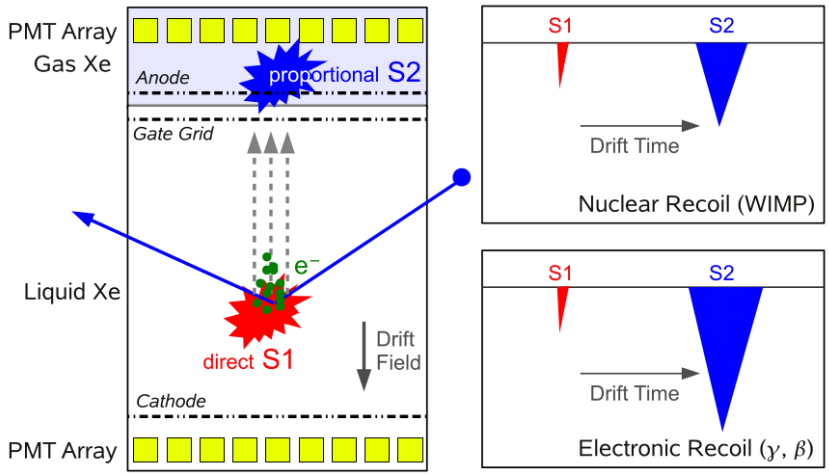

Figure 2.6.: Detection principle of the XENON100 detector: Excitation of the LXe by incident particles results in prompt scintillation (S1) and ionization electrons. The application of a homogeneous drift field transports the charge towards the liquid-gas interface where they are extracted and accelerated by a higher extraction field producing secondary scintillation (S2) proportional to the amount of primary ionization electrons. Figure from [23].

This 3D position reconstruction allows to fiducialize the target, exploiting the very good self shielding of the LXe for background reduction. Background events induced by natural radioactivity and mainly produced at the edges of the TPC cannot penetrate into the fiducial volume and are rejected. Together with the further ability of reducing γ ray induced electronic recoil background events from nuclear recoil WIMP events due to the different ratio $\frac{S2}{S1}$ for the different interaction types, the XENON detectors achieve very low background conditions.

2.3.2. XENON100

The XENON100 TPC is cylindrical with 30.5 cm hight and 15.3 cm radius designed to contain 62 kg of LXe [23]. The walls enclosing the TPC are made of *polytetrafluorethylen* (PTFE), which is a good electrical insulator and reflector for the scintillation light of LXe with a wavelength of 175 nm.

80 PMTs (Hamamatsu R8520-06-A1) are mounted in a densely packed bottom array to achieve a high light collection and thus a low energy threshold, as most of the S1 light will be seen by the bottom array. The 98 PMTs of the top array are ordered in concentric circles to achieve best results in the position reconstruction algorithms. The two PMT arrays are shown in Figure 2.7.

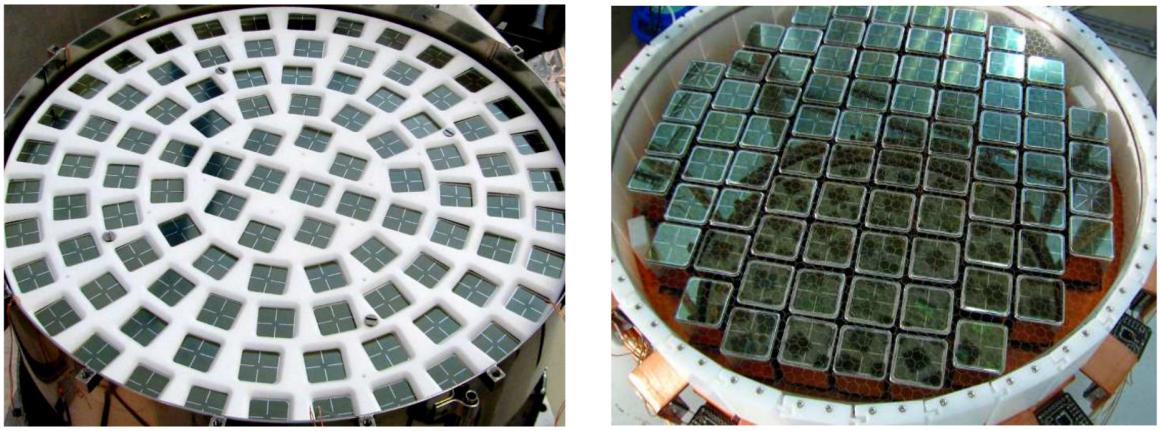

Figure 2.7.: Pictures of the XENON100 PMT arrays, observing the TPC. The left picture shows the top PMT array, where the Hamamatsu R8520-06-A1 PMTs are arranged in concentric circles for high resolution in position reconstruction. The right picture shows the bottom PMT array, which provides optimal area coverage of 52% resulting in high light collection and low detector energy threshold [23].

As described above, three field grids are mounted into the TPC: A cathode grid at the bottom, a grounded gate grid and an anode grid at the top. Together with field shaping electrodes fixed to the PTFE structure this set-up provides the electrical conditions of a homogeneous drift field in the liquid phase and a strong extraction field above the gate grid. The PMT arrays are shielded against the high voltages of the cathode and the anode by another set of grounded meshes, 5 mm above the bottom array and 15 mm below the top array.

With a constant stream of GXe into the gas phase at the top of the TPC, the diving bell is pressurized and the liquid-gas interface can be kept at the same level directly above the grounded gate grid and just a few mm below the anode grid. Furthermore the diving bell design allows a 4π coverage of the TPC by LXe for additional self-shielding and an active outer LXe veto, observed by 64 PMTs mounted to the outer walls of the TPC.

The total amount of 161 kg xenon has to be cooled to the LXe temperature of $-91°$C.

A cryogenic system with very good stability is connected to the detector: a *Pulse Tube Refrigerator* (PTR) is operated with a helium compressor in order to achieve a high cooling power at LXe temperature. The PTR cold head is connected with a copper-made cold finger to the LXe system as shown in Figure 2.8. Electric heaters are mounted between cold head and cold finger and together with two PT100 temperature sensors the heating power is regulated to keep the cold finger stable at the LXe temperature.

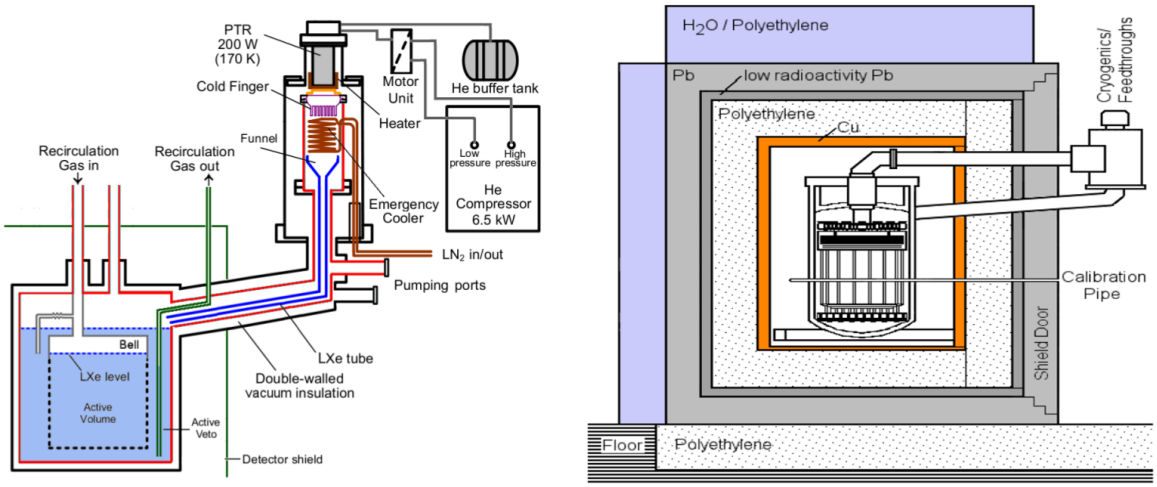

Figure 2.8.: (Left) A schematic drawing of the XENON100 cooling system. Gasous xenon is liquefied at a PTR cold head and circulated back to the LXe outside of the TPC. (Right) A drawing of the passive shield set-up of the XENON100 detector with the different layers of copper, polyethylene, lead and water containers [23].

In order to avoid heat losses the LXe is contained in a stainless steel vacuum cryostat. The cryostat and all inner detector materials of the TPC have high requirements on radiopurity. In this way, radioactive contaminations very close to the sensitive detector volume are avoided, which reduces significantly the background of the experiment [29]. Materials with inevitable contaminations such as the cryogenic system are installed outside a passive shield. The set-up of the passive shield is shown in Figure 2.8. Materials with a high proton number, such as lead, are used to shield against natural radioactivity γ rays. Water or polyethylene are used to moderate and capture neutrons. Therefore, the inner cavity containing the cryostat is surrounded by 5 cm of *oxygen-free high thermal conductivity* (OFHC) copper which is followed by 20 cm of polyethylene and 20 cm of lead, with the innermost 5 cm layer made out of low radioactivity lead. Additional outside water tanks and polyethylene layers complete the passive shield. The inner cavity is purged with high-purity nitrogen to avoid the diffusion of the possible background source radon, a noble gas occurring in the primordial decay chains and emanating constantly from the rock in the underground laboratory. Additionally backgrounds induced by the cosmic ray muon flux are reduced by 6 orders of magnitude compared to an above ground experiment [30], due to the 3 600 m.w.e. of rock overburden at the LNGS.

However there are still some impurities contaminating the LXe, due to its non-ideal produc-

tion process. Electronegative gases and traces of water reduce significantly the transmission of light and charge inside the LXe and therefore lower the signal yield and thus increase the detector threshold. They can however be removed by circulating the xenon permanently through a dedicated gas system with a hot getter outside of the shielding. The gas system as well includes ports for sample taking, detector filling and xenon recuperation. Moreover it provides access to a cryogenic distillation column designed for the removal of krypton and its radioactive isotope ^{85}Kr. This β-emitter with its long half-life of $T_{1/2} = 10.76$ years is a serious background source, because krypton as a noble gas cannot be removed chemically from the target xenon. This type of potential background in the xenon experiment is discussed in more detail in section 2.4.

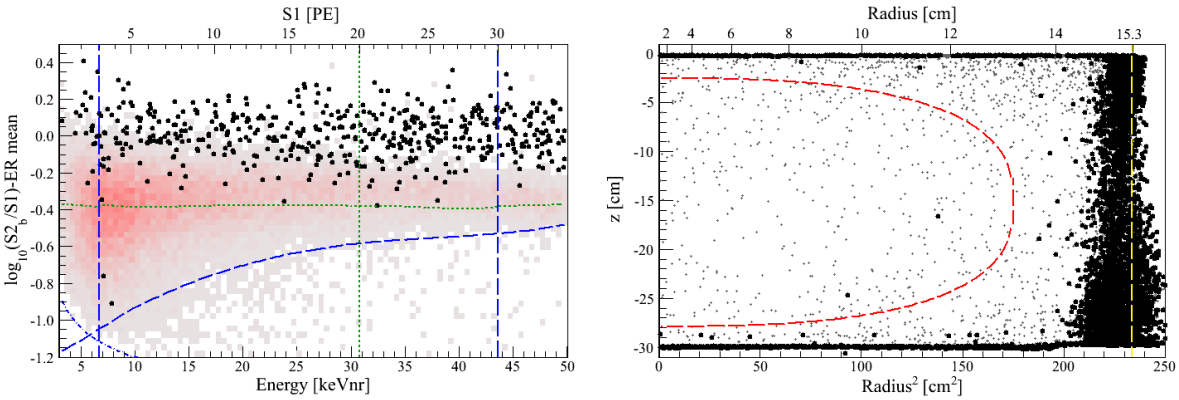

Figure 2.9.: (Left) The event distribution in the $\log_{10}\frac{S2}{S1}$-parameter space after application of all analysis cuts, volume fiducialization and electronic recoil band mean subtraction. The black dots indicate the observed events, the histogram in red/gray shows the position of nuclear recoil events from a neutron calibration. With 99.75 % rejection power, events above the green dashed vertical line are identified as electronic recoils. (Right) The distribution of the events inside the TPC. Grey events are rejected by the discrimination parameter space cut [25].

In 2012 the XENON-Collaboration reported the results of a 225 live-days run with the above described detector system. During this run all subsystems were in stable operations for ∼20 months [25]. With the very low background rate of 5.3 mDRU in the dark matter energy region and a fiducial volume of 34 kg, the experiment demonstrated the lowest background of any dark matter search experiment at that time. Together with the background reduction via S2/S1-discrimination between electronic and nuclear recoils, shown in Figure 2.9, XENON100 was able to set the world-best limits in terms of spin-independent WIMP nucleus scattering for high WIMP masses in 2012 [25]. In a benchmark analysis two events were found in the signal region expecting (1.0 ± 0.2) background events. The result of that WIMP search period is shown in Figure 2.10 using a more sophisticated profile likelihood analysis method [31]. The detector is as well able to test spin-dependent cross-sections due to the non-zero spin isotopes ^{129}Xe and ^{131}Xe, which have high isotopic abundances in the xenon used for the XENON100 experiment. Limits of the 225 life-days run derived for spin-dependent cross-sections can be

found in [32]. Further dark matter models, such as axions, are investigated with the same instrument. Axions arise as possible solution to the strong CP problem of the standard model of particle physics [33] and could be cold dark matter [34]. They would interact with the electronic shell of the xenon atoms in the XENON100 experiment. First results of an axion search with XENON100 were published in [35]. Another possibility is the study of a long term evolution of the electronic recoil rate, searching for an annually modulated signal. Such modulations could be expected due to the movement of the earth around the sun and the thereby induced change in relative velocity of an earthbound detector and the galactic dark matter halo. Rate modulations are already observed and reported by the DAMA experiment [36] or by the CoGeNT collaboration [37] [38]. Such investigations need stable operating conditions over a long time period as achieved by the XENON100 experiment. An analysis searching for a modulated signal is ongoing by using the 225 live-days dataset and will be published soon [39].

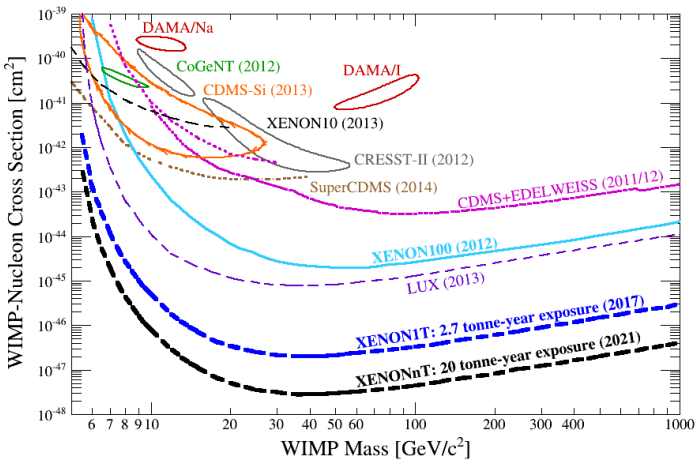

Figure 2.10.: WIMP-nucleon scattering cross-section with the WIMP mass as free parameter. The resulting limit of the XENON100 225 live-days run with 90% C.L. is shown in light blue. Other limits of different experiments are included for comparison, especially the recent results of LUX (2013) and Super-CDMS (2014) [25] [26] [40]. Additionally shown are the expected sensitivities of the XENON1T experiment and its upgrade, XENONnT [41].

2.3.3. XENON1T

In order to improve the sensitivity significantly using this successful technique, a larger detector, XENON1T has been designed and is since summer 2013 under construction. It will be located as well at LNGS, and scale up XENON100 to ~ 3 tons of LXe. An active target mass of ~ 1 ton and a reduction of the background by another factor of ~ 100 are envisaged. After two years of stable operation the scientific goal of $\sigma_{SI} \sim 2 \cdot 10^{-47}$ cm^2 could be reached as shown in Figure 2.10.

Similar to XENON100, XENON1T will be designed as dual-phase TPC with 1 m diameter

and 1 m height. The TPC will be observed by 248 PMTs (Hamamatsu R-11410), 127 in the top array and 121 in the bottom array as can be seen in the artists view in Figure 2.11 (right). Again the set-up of the PMT arrays will be such, that the top array provides optimal position reconstruction and the bottom array provides maximum light yield.

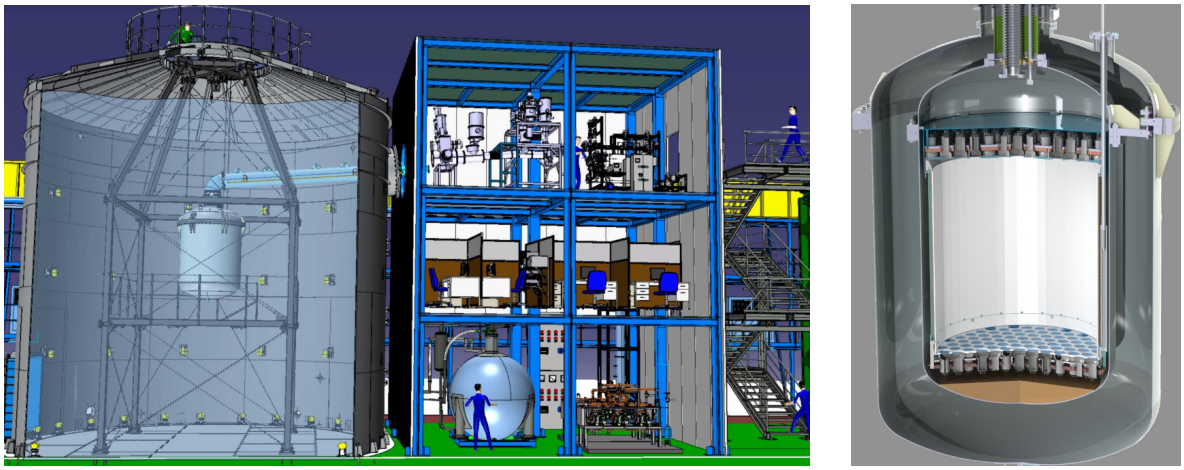

Figure 2.11.: (Left) Artists view of the Xenon1T dark matter experiment. On the left side the water tank operated as Cherenkov muon veto and containing the cryostat including the TPC is shown. On the right side there is the service building containing gas purification systems and DAQ. (Right) Design of the cryostat including the TPC.

The active volume is planned to be ~ 1 ton of LXe, which requires improvements in terms of LXe purity and gas handling. Electron drift of ~ 1 m has to be achieved and stable operation at LXe temperature has to be guaranteed. This will be provided by doubled and improved cooling and purification systems.

The other outstanding challenge for a ton-scale experiment is the further background reduction by a factor of ~ 100 compared to XENON100. Additional to the LXe self-shielding, external radiation from natural radioactivity of the detector surrounding as well as the neutron background will be suppressed by the use of a 9.6 diameter water tank. It will additionally be operated as active Cherenkov light muon veto observed by 90 PMTs, effectively reducing the background of all muon induced reactions [42]. Intensive material screening as done for XENON100 is absolutely mandatory to avoid materials with high radioactive contaminations close to the active target volume. The focus of the screening campaign was intensified in terms of the radon emanation of materials in contact with the xenon. This yields a reduction in the ^{222}Rn background emanating from detector materials, dissolving in the LXe and decaying after a half-life of 3.8 days inside the active volume.

The other remaining intrinsic background, the contamination of the LXe by krypton and its radioactive, long-lived isotope ^{85}Kr will be discussed in more detail in the next section. Like its predecessor experiment, XENON1T will use a cryogenic distillation system for krypton removal, this time designed for higher flow rates and a higher reduction factor. All together

the goal of a factor ~ 100 in background reduction should be feasible for the XENON1T experiment. It is scheduled to start data taking in 2015. Furthermore it opens the possibility for the planned upgrade of the TPC towards XENONnT by using the existing infrastructure.

2.4. The krypton background in XENON

The noble gas krypton and its radioactive isotope ^{85}Kr is one of the most dangerous background sources in the XENON direct dark matter detection experiments. Krypton naturally occurs in air with the volume concentration of 1.140 *parts per million* (ppm). Xenon and krypton are produced as a byproduct in the fractional distillation of air in order to separate nitrogen and oxygen. Further distillation cycles at the producer allow the extraction of xenon. But, it still contains krypton at the ppm or *parts per billion* (ppb) level, if ultra pure xenon is demanded, because of the impossibility of chemically cleaning the xenon from krypton due to the inert properties of these two noble gases.

The two main krypton isotopes are ^{84}Kr and ^{86}Kr with the relative abundances of 57 % and 17.5 %, respectively. The almost pure β-emitter ^{85}Kr, with its long half-life of $t_{1/2} = 10.76$ years, does not occur naturally: its origin is man-made as ^{85}Kr is produced by nuclear fission and released to the air by atomic bomb tests and nuclear fuel reprocessing. This can be seen in Figure 2.12: the activity of ^{85}Kr is plotted over several years as inferred from measurements done at Mount Schauinsland in southern Germany. A constant background activity level of 1.5 Bq/m^3 since 2003 is reported in [43]. The spikes increasing the ^{85}Kr activity up to a factor of three can be correlated to nuclear fuel reprocessing cycles in the two facilities maintained in Europe: La Hague, France, and Sellafield, Great Britain [43].

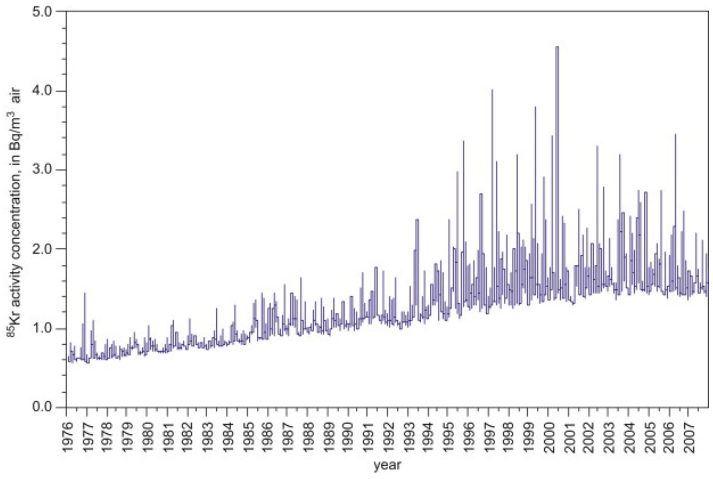

Figure 2.12.: The ^{85}Kr activity monitored at the sampling site Mount Schauinsland, Germany. After a linear increase over more than two decades the activity stays at a background level of 1.5 Bq/m^3. The spikes can be correlated to nuclear reprocessing cycles at the reprocessing plants in France and Great Britain [43].

This however leads to the hypothesis that the variations in between 1.5 Bq/m^3 and roughly 4 Bq/m^3 observed at the Mount Schauninsland do not correspond fully to the variations at LNGS, Italy. Atmospheric circulation which is dominated by western airstreams and the natural frontier of the Alps should flatten the variations for the experimental site of the XENON project with more than 1300 km distance to La Hague. Unfortunately there are no detailed measurements of the ^{85}Kr activity in Italy available, thus the mentioned flattening stays only a hypothesis. An estimate of the average value of 1.5 Bq/m^3 activity at LNGS is however supported by a measurement of (1.3 $\pm$ 0.2) Bq/m^3 taken from [44]. In [45] this measurement is related to the ratio of ^{85}Kr/$^{\mathrm{nat}}$Kr $\simeq 2.0 \cdot 10^{-11}$ mol/mol at LNGS, which is confirmed by others for different experimental sites [46].

In Figure 2.13 the decay scheme of ^{85}Kr is shown. With a branching ratio of 99.6 % it decays with a common β-decay to ^{85}Rb by emitting an electron and an anti-neutrino. The endpoint energy of the β-spectrum corresponds to the Q-value of these two nuclear states of 687 keV. Given the discrimination power between electronic and nuclear recoils of $\sim$99.5 % in the XENON project [47], 0.5 % of the ^{85}Kr decays remain indistinguishable from possible WIMP reactions. Performing a simple benchmark analysis with a WIMP search region of roughly 10 keV an approximated fraction of $\sim$1/70 of ^{85}Kr events fall into the WIMP acceptance window. Admitting only 0.1 event/year originating from the ^{85}Kr background, considering its long half-life of $T_{1/2} = 10.76$ years, the above numbers of the WIMP acceptance window and the electronic recoil rejection translate into 22 000 ^{85}Kr atoms inside the fiducial volume. Using the ratio of ^{85}Kr/$^{\mathrm{nat}}$Kr $\simeq 2.0 \cdot 10^{-11}$ mol/mol the required purity of the xenon in the fiducial volume of XENON100 (48 kg fiducial volume) yields a krypton concentration of $\sim$10 *parts per trillion* (ppt) and for XENON1T (1 ton fiducial volume) of $<$1 ppt.

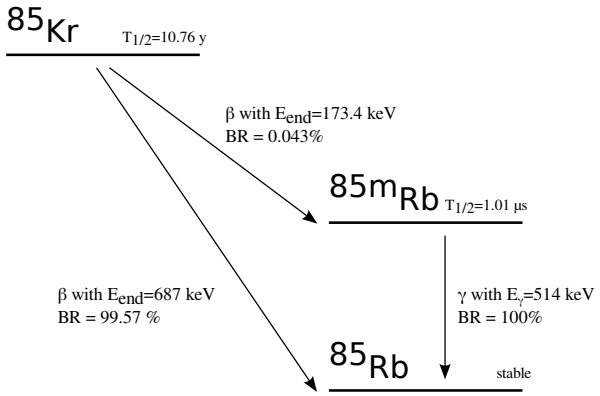

Figure 2.13.: Decay scheme of ^{85}Kr, showing the two decay branches. The main branch with its β-decay of 687 keV endpoint energy is a serious background source in dark matter experiments. The secondary branch with its delayed coincidence can be used in dedicated analysis methods. Numbers from [48].

These small numbers and concentrations impose several challenges for the XENON project: how can these requirements of xenon purity be achieved and equally important, how can they

be monitored for either predicting a background originating from ^{85}Kr decays or confirming achievements done in xenon purity?

The method employed by the XENON project for reaching the purity goals of XENON100 and XENON1T is cryogenic distillation. A schematic view of the distillation column used by the XENON100 experiment is shown in Figure 2.14. The column, designed using the McCabe-Thiele scheme [49], is very similar to [50] and purchased from TAIYO NIPPON SANSO. The commercially available xenon passes a pre-cooler with a PTR cold head and is then fed into the distillation column filled with a package material selected for the expected flow rates and the desired separation factor. A condenser at the top of the column is kept at LXe temperature and liquefies the gas produced in the reboiler at the bottom of the column. After the gas-liquid equilibrium is reached inside the column, the krypton enriched offgas is collected at the top and the krypton depleted LXe is collected at the reboiler, after being fed through a heat exchanger in order to conserve cooling power. Under the assumptions of the McCabe-Thiele scheme the XENON100 distillation column should provide a reduction factor of $\sim$1000 in one single pass at a purification speed of 1.8 *standard liters per minute* (SLPM). For the XENON1T experiment another column is currently under commissioning, able to process xenon at a nominal flux of at least 8 SLPM.

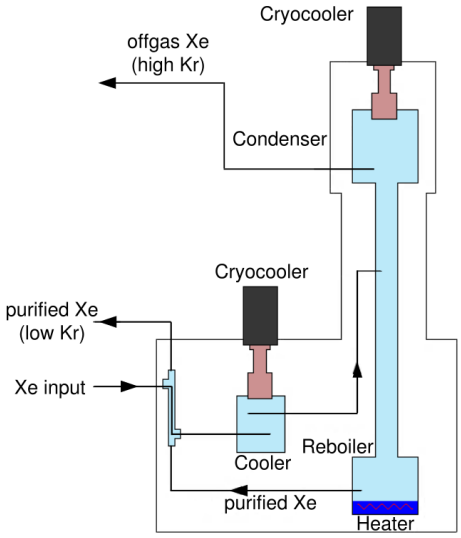

Figure 2.14.: Schematic view of the XENON100 distillation column. Xenon is fed to the column via an heat exchanger and a pre-cooler. Krypton enriched offgas is extracted at the top of the column and krypton depleted xenon is captured in the reboiler [23].

The purification of xenon at such low concentrations has to be confirmed and evaluated by dedicated analytics methods of krypton in xenon concentrations in the low ppt regime. This Master thesis is completely carried out in the context of monitoring krypton in xenon. In order to face this problem the XENON collaboration follows several approaches. Very sensitive methods developed to quantify krypton concentrations in xenon are performed off-line, i.e.

xenon samples are drawn from the detector and analyzed by dedicated set-ups. Usually they exploit the fact that the ratio of $^{85}\mathrm{Kr}/^{\mathrm{nat}}\mathrm{Kr} \simeq 2.0 \cdot 10^{-11}$ mol/mol is well known in order to gain a factor of $2 \cdot 10^{11}$ in statistics by measuring the $^{\mathrm{nat}}$Kr concentration. The XENON collaboration employs two different off-line methods. An optical atom trap system is maintained by the Columbia University in New York [51] and a dedicated set-up described in chapter 3 is located at the *Max-Planck-Institute for Nuclear Physics* (MPIK) in Heidelberg and is used for detailed measurements reported in chapter 4. On the other hand, in-situ methods using the XENON100 detector, try to tag ^{85}Kr events in the observed dark matter datasets. This can be done by comparing the spectral shape of the ^{85}Kr decay with Monte Carlo simulations and reproducing the expected spectrum. This is however limited to the case were the low energy background regime up to 687 keV is krypton dominated. Another possibility is tagging events of the secondary decay branch of Figure 2.13 by the unique β-γ delayed coincidence signature. This is in detail exploited in chapter 5 of this work.

3. Off-line krypton analytics: The RGMS setup

The potential background source ^{85}Kr in the XENON experiments does not occur naturally. Its abundance among natural krypton due to man-made production is on the trace level of $2 \cdot 10^{-11}$ mol/mol, see section 2.4. But as this ratio is rather well determined, a measurement of the ^{85}Kr abundance can be carried out by focusing on the stable krypton isotopes ^{84}Kr and ^{86}Kr. Known experimental techniques, which do not rely on the detection of radioactive decays, for example mass spectrometry or single atom counting in an optical atom trap system, can be used. Such methods require careful sampling and the measurement of the krypton concentration is then performed off-site in a dedicated set-up. Therefore it is called off-line technique.

In this chapter a mass spectroscopic set-up at the MPIK in Heidelberg is presented, which is tuned on the detection of krypton concentrations in xenon down to the *parts per quadrillion* (ppq) level. This reduction in sensitivity was achieved during this work and already reported in [52] by building up on the already existing set-up developed in [45]. The chapter begins with a general description of the set-up in section 3.1 and then focuses on new developments in terms of sensitivity, stability and comprehension gained during this work in section 3.2.

3.1. The RGMS setup

The *rare gas mass spectrometer* (RGMS) describes an experimental set-up consisting of several sub-systems. The analyzing instrument is a customized Vacuum Generators model VG 3600 sector field mass spectrometer which is described in section 3.1.1. Such devices however depend on an *ultra high vacuum* (UHV) with a residual pressure smaller than 10^{-6} mbar, as otherwise the ion mean free path gets to short for defined ion deflections in the applied magnetic field. Facing the problem of measuring trace contaminations of krypton in xenon in the ppt or ppq regime and assuming the sensitivity of the RGMS to krypton amounts to be in the order of 10^{-13} - 10^{-14} *ccmSTP* (cm^3 at standard conditions), see [45] or section 3.2, xenon batches of up to 1 ccmSTP have to be introduced to the mass spectrometer. This however would definitely impair the necessary vacuum conditions. Thus, a pre-separation of the krypton from the bulk xenon is done by cryogenic gas-chromatography, with a set-up described in section 3.1.2 and newly developed in [45]. Samples are mounted to the destined ports of the gas-chromatographic system and can be split up in order to process several batches of the same sample. Additionally the setup contains many accessible ports for

calibration purposes, getter modules, sample preparation and pumping sections. In section 3.1.3 the standard measurement procedure is described and the impact of the different subsystems is explained.

3.1.1. The VG 3600 mass spectrometer

The VG 3600 mass spectrometer was used intensively during the past two decades for the determination of noble gas abundances in earth and planetary sciences [53] as well as for trace analytics in astrophysics experiments [54]. It is designed to be most sensitive to chemically inert substances, due to the presence of getter modules directly in the vacuum system of the spectrometer. This provides a very clean environment for example for the measurement of noble gases.

A detailed scheme together with a photograph of the spectrometer is shown in Figure 3.1. The batch analyzed by the spectrometer is frozen to a cold finger, afterwards reheated and than introduced to the spectrometer by the opening of the interconnecting valve. The gas is distributed in the complete spectrometer volume, but ionization only takes place inside the ion source, close to the inlet valve. A moderate voltage accelerates electrons emitted by a hot filament. The gas is ionized by this electron beam and a high voltage accelerates the ions out of the source, focused by two additional focal plates, with only a fraction of the total high voltage applied. The ions than get deflected in an approximately homogeneous magnetic dipole-field.

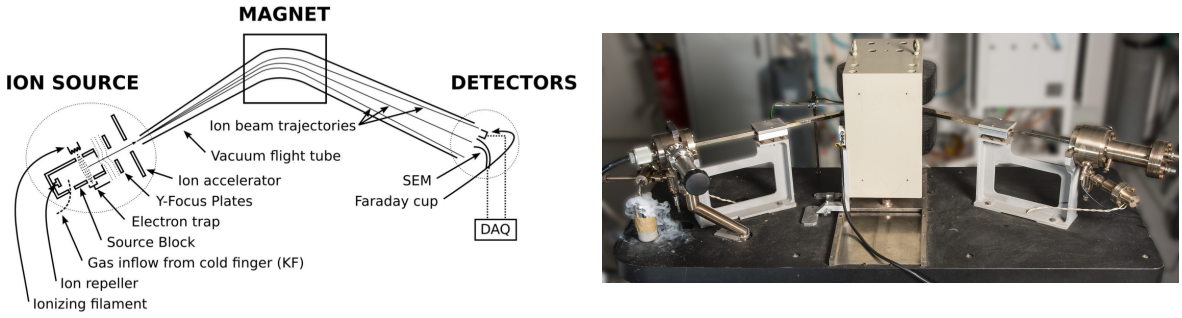

Figure 3.1.: (Left) Schematic drawing of the VG 3600 mass spectrometer, showing the mechanism of ionization in the source, the deflection of the ion trajectories and the two detection possibilities. Figure from [45]. (Right) Photograph of the VG 3600 mass spectrometer, set-up at MPIK.

The mass separation of the spectrometer is achieved by varying the magnetic field, using an empirically assumed fourth order polynomial dependence of field strength f and mass m of the ions reaching the detectors at the end of the flight tube: $f(m) = d+c\cdot m^{1/2}+b\cdot m+a\cdot m^{3/2}$. The necessary determination of the polynomial coefficients is done by inserting a calibration gas containing a noble gas mixture of argon, krypton and xenon and identifying the peaks corresponding to the occurring isotopes.

This calibration mixture is furthermore used for an absolute calibration of the response of the mass spectrometer to a quantified amount of gas. For this purpose the mixture can be extracted into a small pipette volume contained by two fully metal sealed valves at a dedicated port connected to the RGMS set-up. The composition of this *standard calibration pipette* (STD) was redetermined in [45] for krypton and is known for argon and xenon from [55].

STD admixture	amount
argon	$40 \cdot 10^{-9}$ cm^3
krypton	$(39 \pm 6) \cdot 10^{-12}$ cm^3
xenon	$50 \cdot 10^{-12}$ cm^3

Table 3.1.: Composition of one extraction of the *standard calibration pipette* (STD) used to quantify the response of the mass spectrometer and the determination of the field parameters. Numbers from [45] and [55].

Detection at the end of the flight tube is done by either a *secondary electron multiplier* (SEM) device or a Faraday cup. More sensitive to small numbers of ions is the former, consisting of a coated dynode, where incident ions induce the emission of secondary electrons. These are accelerated and amplified by the continuous, tube-like structure of the dynode and registered at a metal anode at the end. Not shown in the schematic view, but visible in the photograph are the two getter modules connected to the spectrometer. Furthermore the device delivered by VG incorporates electronics for the magnetic field controlling, spectrometer bake-out and detector read-out.

3.1.2. Sample preparation by a cryogenic gas-chromatographic set-up

The RGMS is optimized in [45] on its response to the noble gases argon, xenon and especially krypton in order to compete with the needs of the XENON experiments. This included the development of a gas-chromatographic pre-separation device, shown in Figure 3.2, in order to avoid the bulk xenon of the batches influencing the necessary UHV of the VG 3600 mass spectrometer.

Ultra pure helium is needed as carrier gas for the separation process in order to avoid krypton contaminations. Thus, 6.0 helium is further purified by passing it through an adsorbent filled column (T1: 10 mm inner diameter, 8.18 g Carbosieve S-III by Supelco Analytical [45]) at *liquid nitrogen* (LN_2) temperature, where krypton traces get trapped efficiently. An estimate of the achieved purity of the residual helium by this technique is done in this work in section 3.2. The batch extracted from the sample mounted at the destined ports, is quantified in a calibrated volume V_{cal} by its pressure at room temperature. Afterwards it is frozen to a second adsorbent filled column (T2: 6 mm inner diameter, 0.64 g Chromosorb 102 by Johns Manville [45]) at LN_2 temperature. Increasing the temperature by immersing the column

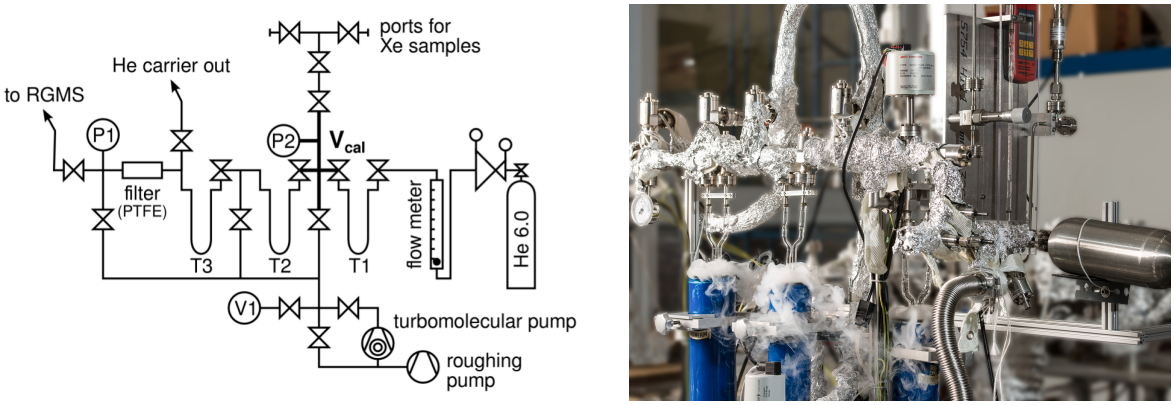

Figure 3.2.: (Left) Schematic drawing of the cryogenic gas-chromatographic set-up. The three adsorbent filled columns are used for He-carrier gas cleaning, krypton-xenon separation and krypton collection. Figure from [52]. (Right) Photograph of the same device, set-up at MPIK.

into cooled ethanol and pushed by the helium carrier gas, the different gaseous components of the batch get macroscopically separated by their different interaction strength with the surface of the adsorbent. Krypton can be collected on a third adsorbent filled column (T3: identical to T2) immersed in LN_2 without collecting xenon if the separating valve is closed before the bulk xenon passes T2. A validation of the very good separation power of this set-up is given in section 3.2.3. All parts of the set-up are selected for high purity standards. Only stainless steel tubes, copper sealed flanges and fully metal sealed valves are used. The adsorbent filled columns are made of borosilicate glass with special glass to metal seals [45]. A standard turbomolecular pump together with an oil-free piston pump are used to set the vacuum system and avoiding the diffusion of adsorbent polluting hydrocarbons.

The acceptance a_{Kr} of the gas-chromatographic procedure was determined in [45] for krypton. This was done by performing the separation procedure with the STD and the comparison of the result with the known calibration response of the mass spectrometer. The result is $a_{Kr} = (0.97 \pm 0.02)$.

3.1.3. Xenon assay

In [45] a standard xenon assay procedure was developed and evaluated. Xenon samples are usually filled in sample containers, commonly referred to as sample pipette. The standard sample pipette used consists of four fully metal sealed valves welded together. An example of such a sample pipette is shown in Figure 3.3. Destined sampling ports are available in the XENON100 experiment, see section 2.3.2, and also planned for XENON1T. Usually the sample pipette is baked moderately and pumped for a few days before filling in order to remove residual krypton contaminations. More intensive care has to be taken in ultra pure xenon sample taking which will become necessary for XENON1T and is described in section

4.3. The sample pipettes are then filled with the pressure of the operating system, in the case of the XENON100 experiment this is $\sim$2.2 bar. This slight overpressure reduces the risk of sample contaminations due to internally leaking valves, which enclose the sample. Furthermore, if a standard pipette is used, the three different volumes enclosed by the four valves, are separated and an internally leaking valve can be identified if the results of different volumes differ significantly.

Figure 3.3.: A standard xenon sample pipette used in this work. Four fully metal sealed valves are welded together and enclose three separable sub-volumes. The innermost volume is thus shielded on both sides by two valves and one buffer xenon volume minimizing the impact of eventually internally leaking valves.

Once the sample pipette is mounted to the ports at the RGMS, the chromatographic process can be performed. This includes the splitting of the sample into several batches and the determination of the assayed gas amount in the calibrated volume V_{cal} with a precise capacitance manometer (Edwards Barocel 600 series, 0.15 % accuracy [45]). The gas-chromatographic procedure is performed in standard operations with -80 °C at T2, a helium carrier gas flow of 40 ml/min and a 880 seconds acceptance window for krypton until T3 is closed to cut off the bulk xenon. Subsequently the gas is transferred to the cold finger of the mass spectrometer by cryogenic pumping for 40 minutes. This includes opening a valve to an additional high temperature getter module from SAES. It removes very efficiently non-inert impurities by chemically binding them, because some of them pass the chromatographic process due to similar retention times to that of krypton, as shown in section 3.2.3. The batch transfer to the mass spectrometer can be monitored by a friction manometer (Leybold VK201), avoiding any additional contaminations of the batch from the sensor.

Stopping the cryogenic pumping by closing the connecting valve at the mass spectrometer, the cold finger is reheated to room temperature, while the evacuation of the spectrometer is stopped and data taking starts. The response of the spectrometer to ^{84}Kr for a STD measurement is shown in Figure 3.4 (left).

The background of the measurement is determined by looping over the considered isotope masses and observing their evolution with time. Outgassing of hydrocarbons and residual noble gases from the spectrometer walls leads to a slight increase of the observed background before gas inlet. At a time t_0 the valve to the reheated cold finger is opened and the gas distributes inside the spectrometer, is ionized and detected. This results in a sudden increase of the response of the SEM or Faraday cup. Ion implantation to the spectrometer walls provokes

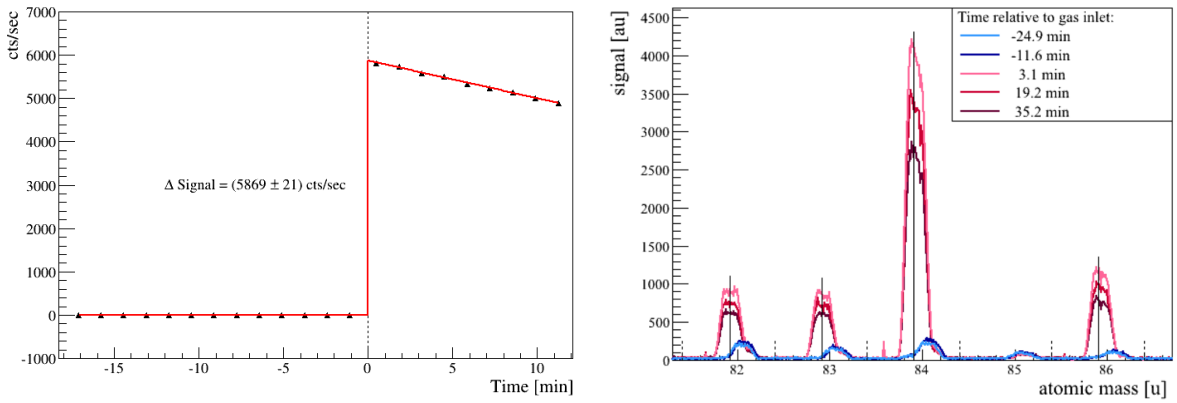

Figure 3.4.: (Left) Time evolution of the ^{84}Kr SEM-signal for a STD measurement. At t_0 the gas is introduced to the spectrometer and the pedestal is later on quantified by linear fits to the increasing background before and the decreasing signal after gas inlet. (Right) Several mass-scans over the expected krypton region are performed. Slightly shifter to higher masses and present before the gas inlet there is a background of (multiply) ionized hydrocarbons. With introduction of the STD, the peaks appear at lower masses clearly indicating the presence of krypton isotopes. Figure from [45].

a slowly decreasing signal with time as well quantified by looping over the considered isotope masses. The observed pedestal at t_0 inferred by the interpolation of the two linear regimes before and after gas inlet, quantifies the response of the spectrometer to an introduced amount of gas. In Figure 3.4 (right), several mass-scans over the main krypton isotopes are performed before and after gas inlet. The background present before the inlet is shifted to higher masses. It is mainly due to the presence of (multiply) ionized hydrocarbons, which appear at higher masses due to their high number of hydrogen constituents. With the introduction of the STD the peaks appear at the calibrated values of the krypton isotopes. As well in this plot the time dependence can be seen: Increasing before gas inlet due to outgassing and decreasing afterwards due to ion implantation to the spectrometer walls.

Being able of quantifying amounts of noble gases with the VG 3600 mass spectrometer and assaying amounts of few ccmSTP xenon with the pre-separation device, the RGMS set-up achieves a high sensitivity for trace contaminations of krypton in xenon. The *krypton impurity level* (KIL) of an assayed xenon batch can then be determined from the ratio of the krypton amount quantified by the mass spectrometer and the volume of the xenon batch:

$$\mathrm{KIL} = \frac{\langle (S_i - B_i) \cdot f_m(i)^{-1} \cdot \mathrm{STD}_i \rangle_i \cdot a_{Kr}^{-1}}{^{\mathrm{nat}}\mathrm{Xe}} \,. \tag{3.1}$$

The batch size is inferred from the pressure p and temperature T in the calibrated volume of the chromatographic set-up via $^{\mathrm{nat}}\mathrm{Xe} = p \cdot V_{cal} \cdot T_0/T$, where T_0 denotes the standard temperature. The trace amount of krypton is calculated by considering, if available, several isotope measurements. For a single isotope the pedestal of the batch is related to the pedestal of a calibration measurement, performed at least once before processing the batch. This ratio

is given by S_i and corresponds to the signal strength, whereas B_i denotes the background strength, which is subtracted from the signal strength and determined by procedure blank measurements. This means measurements of the full gas-chromatographic procedure without a xenon batch introduced to V_{cal}. This gives an estimate of the background present due to the introduction of impurities to the batch as a result of air leaks in the system or contaminations of the helium carrier gas. B_i is usually averaged over several measurements of a time period in which the operating conditions were approximately equal. The result obtained for a specific isotope is in the end multiplied by its mole fraction $f_m(i)$ and related to the STD amount. The considered isotopes are then averaged $\langle ... \rangle_i$ and divided by the acceptance a_{Kr} of the full procedure.

This final result includes several types of uncertainties, which were intensively studied for krypton impurities in [45]. All measurements are influenced by systematic errors on the STD (ΔSTD), the acceptance of the chromatographic process (Δa) and the xenon batch size (Δ^{nat}Xe). The latter is dominated by the uncertainty of the capacitance manometer p at V_{cal} estimated to be $\sim$ 3.5 %. The uncertainty of the calibration pipette $\Delta\mathrm{STD}_{Kr}$ is in the order of 16.5 %, which by far dominates the systematics.

Moreover, each single measurement is subject to variations in the chromatographic procedure, instabilities of the ion source high voltages, statistical uncertainties in ion counting at the SEM and background fluctuations due to variations of tiny air-leaks or internal outgassing effects. The latter is in detailed discussed in section 3.2.2 and 4.3. The uncertainty due to these statistical fluctuations can be estimated by the standard deviation of the common mean if several batches of the same sample are measured. In the case that only one single measurement is available the averaged standard deviation of all samples measured so far is considered. This standard deviation for a single measurement is evaluated in [45] to 13.5 %. In section 3.2.1 a re-evaluation of this number is performed, as more care has been taken on stable operating conditions during this work, which pushes the total error (the quadratic sum of the systematic and statistic effects) already close to the limits given by the systematic effects.

3.2. Improvement of the Sensitivity and Stability of the RGMS

As presented in the previous section, the RGMS system was optimized to its response to krypton in xenon already in [45]. First results of measurements at the ppt level are presented in [52], for example a sample taken during the 225 live-days run or samples showing the performance of the krypton distillation done after the end of this run.

But facing the upcoming challenges of the XENON1T experiment and its experimental goal of reducing the krypton concentration down to $\sim$200 ppq, this work was dedicated to improve the sensitivity of the RGMS. Furthermore stable operating conditions are desirable for longterm operations and thus constant monitoring of the XENON1T experiment. Hence,

the next section explains the improvements of the set-up and the very good results concerning the reached stability, which is closely linked to the achieved sensitivity, already projected in [52] and in detail discussed in section 3.2.2.

3.2.1. The RGMS stability

The stability of the RGMS system depends on the reproducibility of measurements with the mass spectrometer and on fluctuations of the gas-chromatographic procedure. The former is mainly dominated by the settings of the ion source of the mass spectrometer. During this work the accelerating high voltage was set to 5 kV by a high voltage module (FUG HCE 35-6500). A custom-made electronic controller for the ion optics was added to the set-up. This system includes a voltage dividing chain to set the ion focusing and repelling voltages, the supply for the electron accelerating voltage and a PID controller for the cathode current, which leads to constant electron emission. All parameters are monitored and most of them can be set independently. Before each measurement the parameters were adjusted manually to their standard values, which were optimized for a maximum response of the mass spectrometer to the krypton isotopes at the beginning of this work. This is most important for the focusing voltages, as tiny leakage currents appearing on the focal plates lead to longterm shifts of the settings. During one measurement, small fluctuations of the voltage supplies as well as shifts of the aforementioned leakage currents appearing inside the ion source lead to further instabilities in the ionization process and the subsequent ion acceleration and focusing. Thus the response of the mass spectrometer to the same amount of gas can show variations. This is easily monitored by comparing the continuously taken calibration standard measurements. In Figure 3.5 (left) the evolution of the response of the mass spectrometer to the STD is plotted over time.

Two very stable periods are visible. The change appearing at the December 11, 2013, was triggered by the introduction of a highly polluted batch which was measured that day. The high rate of ion implantation on the coated dynode surface of the SEM caused aging effects of the device and thus lowered its response to the STD after that incident. For stable operating conditions such high rates have to be avoided for the SEM. Therefore the gas amount introduced to the spectrometer is usually monitored by the friction manometer mounted to the set-up after the gas-chromatographic pre-separation. Figure 3.5 (right) shows the corresponding histograms for the response of the mass spectrometer to the STD for these two time periods. Gaussian fits give reasonable results and from the inferred standard deviation an estimate for the stability of the mass spectrometer can be done. Both periods give a relative uncertainty of $\sim$16 %. This confirms that only the SEM got damaged leading to an absolute decrease of its response and no other effect was provoking it.

The response of the mass spectrometer is thus longterm stable within $\sim$16 %. However, this might be not the correct estimate for the precision of a single krypton in xenon measurement

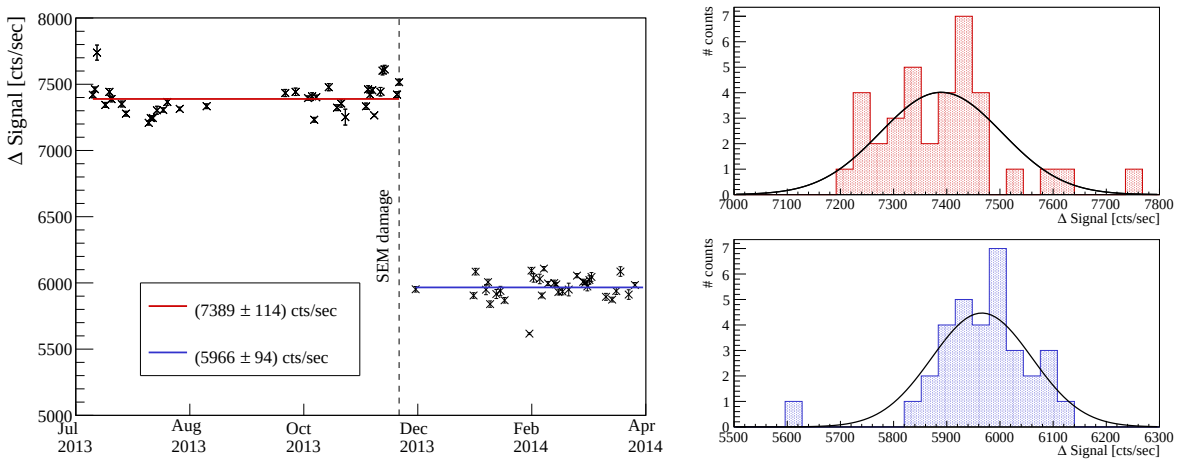

Figure 3.5.: (Left) The evolution of the response of the mass spectrometer to the STD over time. The SEM got damaged during the measurement of a highly contaminated sample, which explains the drop of the response observed at the beginning of December 2013. (Right) All available measurements of both time periods are shown in two different histograms, the upper corresponding to the period before the SEM damage and the lower corresponding to the period after the SEM damage. The relative uncertainty determined by a gaussian fit stays approximately identical with ∼16 %.

performed with the complete RGMS procedure. First, variations of the STD response might be as well due to different amounts of gas extracted from the STD for calibration. The extraction is done by a small volume enclosed by two fully metal sealed valves closed with a torque wrench, which can lead to tiny volume differences. Second, two subsequent measurements of the STD at the same day showed highly correlated results. This means, that the output of single calibration measurement seems to reflect the operating conditions more precisely than the averaged response. Therefore, a STD measurement is performed before every assayed batch. Third, and already mentioned at the beginning, the complete measurement procedure is subject to fluctuations, for example variations in the gas-chromatographic procedure (such as slight differences in the ethanol bath temperature, etc.).

For the above reasons, as already done in [45], the standard deviations of all available krypton in xenon measurements are averaged in order to get an estimate of the statistical uncertainty underlying the complete measurement procedure. Considering the results of chapter 4 with no special concerns, this leads to a 2.9 % statistical standard deviation for a single measurement. This value is lower than the one reported in [45]. On the one hand, this can be due to the possibility of monitoring the parameters of the ion source and their adjustment before each measurement, which seems to guarantee way more stable operating conditions. This pushes down the uncertainty for a sample where only one single batch could be measured down to 17.2 % dominated only by the overall systematic error.

On the other hand, the complete RGMS system was simplified during this work, facing another source of possible measurement instabilities: the leak tightness of the system. Tiny

(diffusive) air-leaks of the UHV system can introduce krypton from the ambient air, which would increase the background. Moreover, these air-leaks might be varying with time, as the ambient pressure or the mechanical stress on the leaky system component is subject to variations. Therefore constructional elements known to be a source of possible air leaks have to be minimized, mainly flexible tubes and valves.

A schematic overview of the RGMS set-up is given in Figure 3.6. As the mass spectrometer

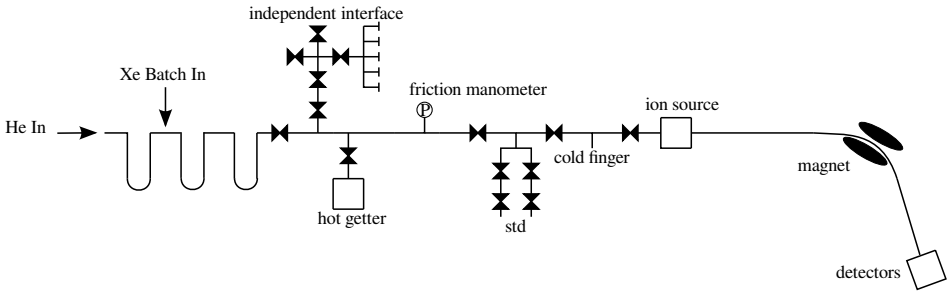

Figure 3.6.: Schematic overview over the full RGMS setup at the time of writing. Compared to [45] the interface is made independent from the standard procedure in order to reduce possible sources of defect components, but still fully accessible for additional operations.

was used for many other purposes during the last two decades, the complete set-up contains several dead flanges, enclosed tubes and unnecessary valves. But due to already reached very good UHV conditions and mechanically fixed sections, a complete reassembling of the set-up is not desirable. However, during this work, the part used for installing an independent calibration pipette, see [45], which contains several accessible sampling ports, was moved out of the standard procedure, simplifying the set-up and avoiding possible sources of tiny air-leaks.

Furthermore the complete RGMS system was leak checked first by measuring accumulated blanks of the different separable sub-volumes of the set-up with the mass spectrometer and afterwards performing detailed leak checks with a dedicated helium leak detector. With this twofold approach leaks very close to the detection limit of the leak detector could be identified and removed.

3.2.2. The RGMS sensitivity

Closely linked to the question of leak tightness is the sensitivity of the RGMS, because background fluctuations are a limiting factor for it, as it can be seen in the following. The theoretical sensitivity of the RGMS can be calculated by the ratio of the minimal amount of krypton detectable with the RGMS $\left({}^{\mathrm{nat}}\mathrm{Kr}\right)_{\mathrm{min}}$ and the maximal amount of xenon which can be processed $\left({}^{\mathrm{nat}}\mathrm{Xe}\right)_{\mathrm{max}}$.

The former can be inferred following the international standards for measurements of ionizing radiation [56] and is illustrated in Figure 3.7. Starting point are the fluctuations of the background underlying any krypton measurement. At 90 % probability that a measured

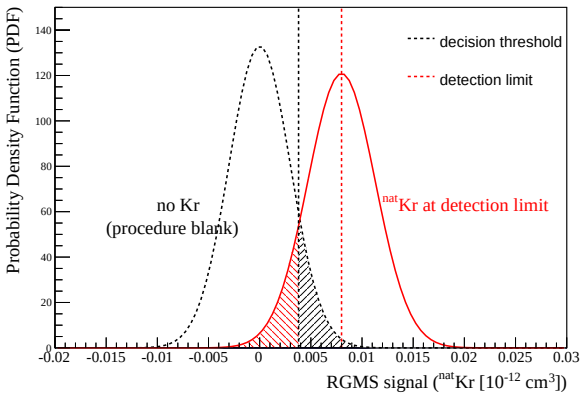

Figure 3.7.: Sketch illustrating both decision threshold and detection limit [56] at the 90 % confidence level for the RGMS krypton assay assuming a procedure blank of (0.013 ± 0.003) ccmSTP ^{nat}Kr and a uncertainty of 17.2 % for a single measurement. Sketch adopted with new values from [45].

result corresponds to a gaussian fluctuation of the background a decision threshold is set. An observed outcome of a measurement is treated as signal-like if the result is above this decision threshold. The minimal detectable amount of krypton $\left(^{nat}\mathrm{Kr}\right)_{\mathrm{min}}$ is defined at 90 % C.L. as the mean of a gaussian distribution, with the standard deviation for the outcome of a single krypton in xenon measurement, with 90 % of the distribution above the decision threshold. This means, that for a krypton amount of $\left(^{nat}\mathrm{Kr}\right)_{\mathrm{min}}$ there is a 90 % probability of being treated as a signal-like outcome, if only one single measurement is done.

A first conclusion is that background fluctuations and signal stability are the two main impacts on the reachable sensitivity of the RGMS. As already discussed in section 3.2.1 huge efforts were made during this work in order to improve the signal stability and the background fluctuations, mainly by observing the ion source parameters and assuring absolute leak-tightness of the system. As discussed in the previous section, the standard deviation for a single RGMS measurement is found to be 17.2 %, mainly dominated by systematics. And on the other hand, repeated and combined measurements of the procedure blank under the same operating conditions give an valuable estimate of the strength of the background fluctuations.

The development of the procedure blank of the RGMS system as a measure of the background and its fluctuations is shown in Figure 3.8. This evolution can be split up in different periods, where the averaged procedure blank showed different results. During this work, the improved leak-tightness of the system lead to a reduction of the procedure blank first to $(0.081 \pm 0.004) \cdot 10^{-12}$ ccmSTP ^{nat}Kr and later even further down to $(0.013 \pm 0.003) \cdot 10^{-12}$ ccmSTP ^{nat}Kr.

With the most stable background conditions achieved in December 2013 and the above calculated standard deviation of a single measurement, the theoretical minimal amount of krypton which can be detected with the set-up gets $\left(^{nat}\mathrm{Kr}\right)_{\mathrm{min}} = 0.008 \cdot 10^{-12}$ ccmSTP at 90 % C.L. Showing in chapter 4 that the processing of xenon amounts of at least 2.85 ccmSTP

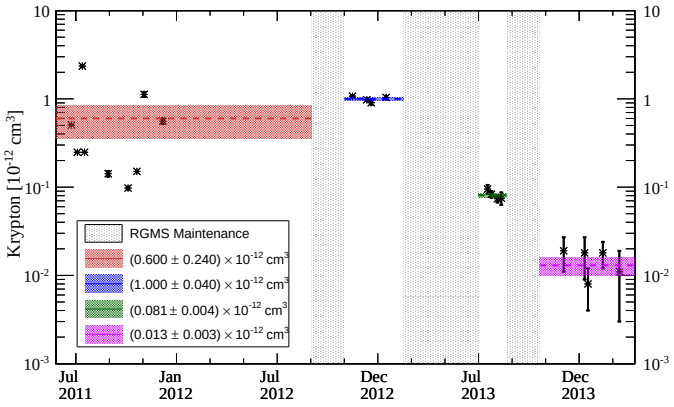

Figure 3.8.: Evolution of the procedure blank during this work and [45]. The leak search done in summer 2013 reduced the background and its fluctuations significantly. Afterwards stable conditions were only reached by taking intensive care for leak tightness, indicating that the dominant background contribution are still the presence of tiny air-leaks.

is possible with the gas-chromatographic set-up, this translates to an overall theoretical detection limit at 90 % C.L. of the RGMS of

$$\mathrm{DL} = \frac{\left(^{\mathrm{nat}}\mathrm{Kr}\right)_{\mathrm{min}}}{\left(^{\mathrm{nat}}\mathrm{Xe}\right)_{\mathrm{max}}} = 3 \cdot 10^{-15}\ \frac{\mathrm{mol}}{\mathrm{mol}} = 3\ \mathrm{ppq}\ . \tag{3.2}$$

Understanding the contributions to the procedure blank is mandatory in order to further improve, and even more important, to guarantee longterm stability of this excellent background conditions. As already pointed out in section 3.2.1 the set-up was for this reason modified in order to exclude possible leak sources from the standard procedure. Another possible contribution to the background is the residual krypton concentration of the helium carrier gas. About (900 ± 120) ccmSTP helium is used in the procedure, estimated by the amount of helium necessary to fill the gas-chromatographic set-up (total volume of $\sim$ 290 cm^3) to a pressure of $\sim$1 bar and flushing the column for $\sim$15 minutes with a flux of $\sim$40 ml/min in order to perform the separation. The contribution of krypton added to the procedure by this amount of helium carrier gas can be estimated by comparing actual procedure blank measurements with freezing blanks of all contributing volumes. A freezing blank is the transfer of the residual amount of gas present in T3 to the cold finger of the mass spectrometer by cryogenic pumping after intensively pumping and baking the contributing volumes, including T3, in advance. The average of several such measurements can be related to the amount of krypton quantified by the procedure blank. With this method, only an upper limit of the residual krypton contamination of the helium carrier gas after the purification in T1 is found with $\frac{^{\mathrm{nat}}\mathrm{Kr}}{^{\mathrm{pur}}\mathrm{He}} < 0.012 \cdot 10^{-15}\ \frac{\mathrm{mol}}{\mathrm{mol}} = 0.012$ ppq at 90 % C.L.

Lowering the procedure blank further in order to increase the sensitivity therefore already gets very difficult. Absolute leak-tightness is assured as far as it is possible with the present

set-up, and the contribution of the helium carrier gas can be completely neglected. Furthermore, the detected amounts of krypton with the mass spectrometer in a procedure blank measurement are already very close to the detection limit of the mass spectrometer itself. This is shown in Figure 3.9.

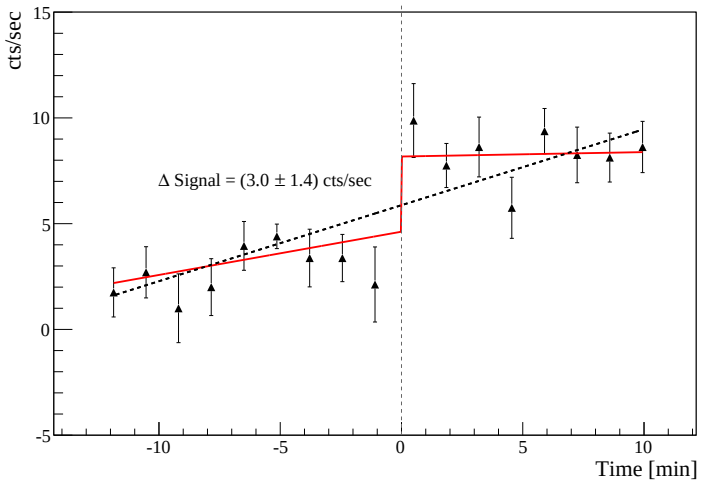

Figure 3.9.: The response of the mass spectrometer for a measurement of the procedure blank at the lowest achieved conditions. A pedestal function as well as a linear increase are fitted to the data, resulting in $\chi^2/_{\mathrm{NDF}} = 0.91$ and $\chi^2/_{\mathrm{NDF}} = 1.35$, respectively. This indicates that the measured krypton amount is already very close to the detection limit of the mass spectrometer.

The measurement of a procedure blank is shown, resulting in $(0.018 \pm 0.009) \cdot 10^{-12}$ ccmSTP krypton. The measured pedestal already has a ~ 50 % relative uncertainty due to the limited ion counting statistics. Both a linear interpolation and the pedestal fit result in high p-values of 0.16 and 0.54, respectively. Thus, it gets already difficult to decide, weather the observed data are correctly described by a pedestal-like gas inlet. It can be concluded, that such a result is close to the detection limit of the mass spectrometer, which is then in the order of $1 \cdot 10^{-14}$ ccmSTP $^{\mathrm{nat}}$Kr. Only few possibilities are left in order to increase statistics. A higher sensitivity of the SEM can be achieved by increasing the collecting high voltage. This however is not permanently achievable as aging effects always will reduce the sensitivity and even speed up at higher voltages. Additionally the measurement procedure could be changed, neglecting the by default performed simultaneous measurements of argon and xenon masses for cross-checking reasons, and thus increasing the rate of looping over the krypton isotopes. This however reduces the statistical uncertainty only by few percent as already verified in tests with the STD.

As the background is already very close to the detection limit of the RGMS, a further increase of its sensitivity could be achieved by increasing the amounts of xenon which can be processed by the gas-chromatographic set-up. Therefore a detailed study on the separation power of the existing columns is performed in the next section.

3.2.3. Investigating the gas chromatographic separation procedure

In order to test the performance of the used adsorbent filled column in regard of its krypton/xenon separation the RGMS set-up is modified. A commercially purchased gas chromatograph (Trace GC Ultra from Thermo Scientific) is available in the same laboratory at MPIK. Mounted to this device is a *pulse discharge detector* (PDD), which is based on pulsed helium discharge photo-ionization, see [57] and [58]. The complete set-up was already studied in [45] in regard of its response to krypton traces.

For a test of the gas-chromatographic separation procedure of the RGMS, the PDD is connected directly to the output of the helium carrier gas (which is in the standard procedure just released to air) of the gas chromatographic set-up by stainless steel tubes of approximately 10 meters length. The modification of the set-up is shown in Figure 3.10 (left). The gas transfered to the PDD can be analyzed: a pulsed high voltage discharge is produced by two electrodes in a clean helium environment, flushed with a typical flux of ~ 60 ml/min, avoiding contaminations of the electrodes. Photons of the emission continuum between 13.5 eV and 17.5 eV [59] can then ionize all gas components introduced to the PDD, except neon and the carrier gas helium itself. The ionization current is then read out by a collector electrode. A schematic view of the PDD is shown in Figure 3.10 (right).

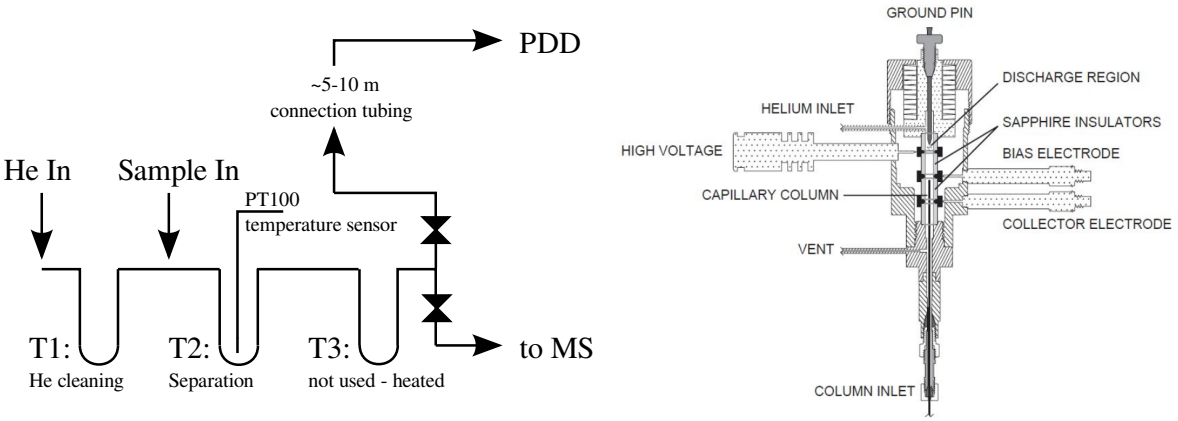

Figure 3.10.: (left) Modification of the gas chromatographic set-up of the RGMS used for krypton/xenon separation. The helium carrier gas is led to the PDD by a stainless steel connection tube. A temperature sensor at T2 allows for the precise evaluation of the gas-chromatographic separation procedure. (right) Schematic view of the a pulsed discharge detector (PDD). Figure from the VICI (Valco Instruments Co. Inc.) Pulsed Discharge Detector Models D-4-I-TQ-R and D-4-I-TQI-R Instruction Manual.

As the connection tube between the output of the gas-chromatographic set-up and the detecting device is in the order of 10 m, a measurement quantifying the time-offset between the gas reaching the adsorbent filled column T3, which collects the gas in the standard procedure, and the actual detection at the PDD was performed. Hydrogen is spiked at the output of the gas-chromatographic system and the time-offset to the subsequent detection is

measured, yielding $\Delta t = (190 \pm 10)$ s for a helium carrier gas flux of (41 ± 2) ml/min, which is typical in the standard procedure. Additionally, a PT100 temperature sensor is mounted to the adsorbent filled column T2, in order to investigate the influence of temperature deviations on the separation procedure.

First, a 1:4 krypton/xenon mixture is separated with the standard procedure by the column T2 and the result is shown in Figure 3.11 (left). Thereby, 0.048 ccmSTP of the mixture are frozen to the column T2, which is set to -80 °C at time t_0. The acceptance window of the standard procedure is shaded in gray, shifted by the time offset Δt between detection at the PDD and the usual collection at T3. In order to speed up the process, the column is set to -30 °C after 30 minutes, reducing the time xenon needs to elute from the column.

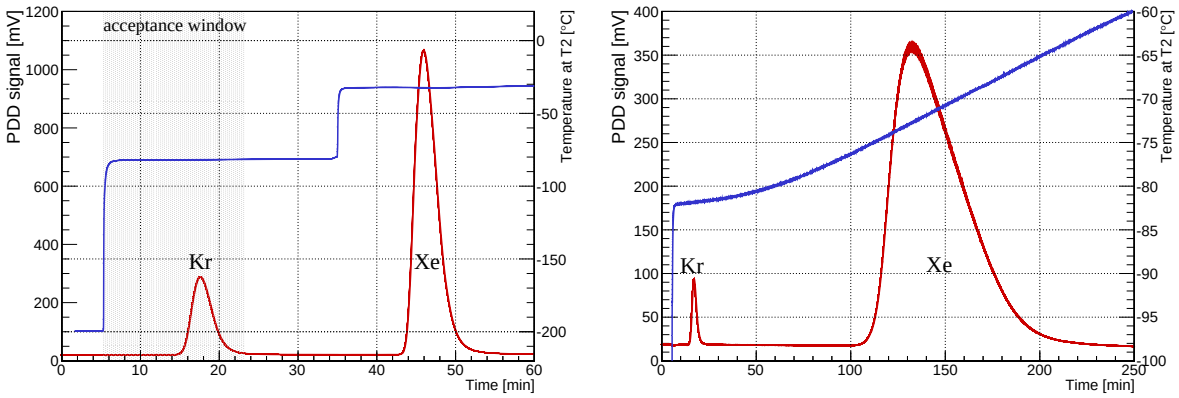

Figure 3.11.: (left) PDD signal (red) for a separation of a 1:4 krypton/xenon mixture. Krypton reaches the collecting column T3 ∼9:00 min after the start of the chromatographic procedure and completely inside the acceptance window of the standard procedure. As indicated by the temperature evolution at T2 (blue) the process is speeded up by increasing the temperature to -30 °C, pushing the xenon through the column. (right) PDD signal for a separation of a 1:100 krypton/xenon mixture. After setting the separating adsorbent filled column T2 to -80°C, the ethanol bath is left untouched, resulting in a modest temperature increase (blue) towards ambient temperature. First xenon traces reach the PDD only after ∼100 minutes and a temperature of -76°C.

The krypton peak reaches the collecting column T3 ∼9:00 min after the temperature increase from LN_2 to a -80 °C ethanol bath. Only, if at all, a very tiny fraction of the slow tail of the krypton peak is cut off, confirming the estimation of the krypton acceptance of the gas-chromatographic procedure of $a_{Kr} = (0.97 \pm 0.02)$ done with the mass spectrometer in [45]. This is supported by the fact that the sketched acceptance window is only a conservative lower limit, because the time the gas needs to pass the heated column T3 is not considered in the used time-offset Δt.

The xenon peak reaches the collecting column only after setting the column to a -30 °C ethanol bath. No traces of xenon, which would contaminate the extracted krypton, seem to appear before this increase. This is supported by the measurement shown in Figure 3.11 (right), where a 1:100 krypton/xenon mixture is separated by the column, but this time

without pushing the xenon out of T2 by abruptly increasing the temperature. The temperature just slowly converges towards ambient temperature due to the heat input from the environment. Therefore the peak corresponding to xenon is broadened compared to the one in Figure 3.11 (left). The first traces of xenon then appear at T3 $\sim$95 min after the start of the chromatographic process and at a temperature of $\sim$-76 °C. This means that indeed no bulk xenon passes the gas-chromatographic separation, providing the necessary vacuum conditions required for the trace analysis performed with the VG 3600 mass spectrometer in the standard procedure.

On the other hand, this measurement shows that xenon already starts to pass the separating column at temperatures very close to -80 °C. As the ethanol bath is cooled down manually, temperature fluctuations might be present. For this reason Figure 3.12 (left) shows the systematic influence on the separation power for different ethanol bath temperatures.

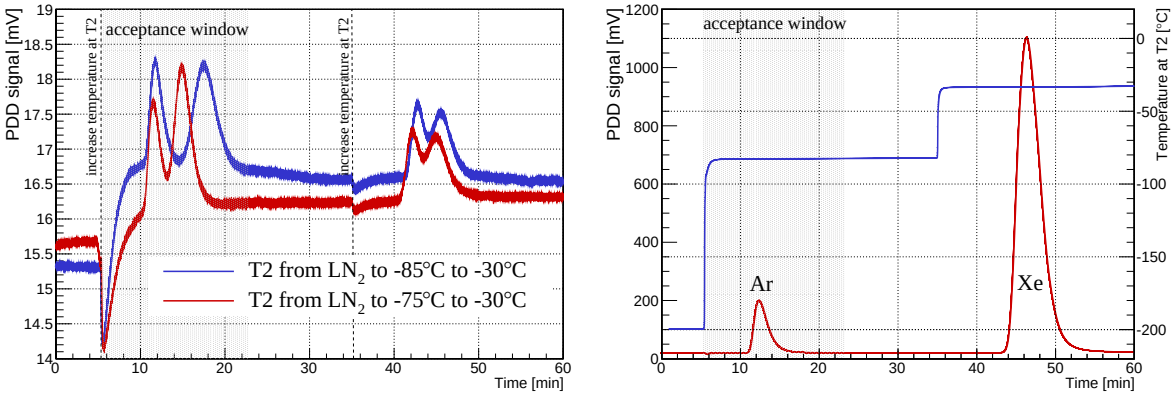

Figure 3.12.: (left) PDD signal (red) and temperature at T2 (blue) for a separation of a 1:4 argon/xenon mixture. Argon reaches the collecting column T3 $\sim$3:50 min after the start of the chromatographic procedure. (right) PDD signal for two different separation procedure, showing its dependence on the temperature at T2.

This measurement is performed with a helium calibration gas mixture containing contaminations of hydrogen, oxygen, nitrogen, carbon dioxide, methane, argon, krypton and xenon on the 5-10 ppm level. The krypton peak is identified as the second one by comparing the arrival time at T3 with the one obtained by measuring the pure krypton/xenon mixture. No xenon traces are registered in the acceptance window for the separation performed at -75 °C. Moreover, the acceptance of the separation process stays unaffected on the sensitivity level of the PDD, as no krypton tail outside the acceptance window is visible, even for the measurement with higher retention times performed with a -85 °C ethanol bath. Assuming that the manual cooling does not result in differences larger than ±5 °C, the separation procedure can be considered as stable in regard of its high acceptance and good separation power.

Figure 3.12 (right) confirms that the first peak observed in the separation of the helium calibration gas mixture of Figure 3.12 (left) indeed corresponds to the noble gas argon, as for this measurement a 1:4 argon/xenon mixture was processed. The argon peak reaches the

collecting column at $\sim$3:50 min after the start of the chromatographic separation procedure. The appearance of the peak before the krypton peak allows the assumption that its acceptance a_{Ar} is at least as high as the acceptance for krypton a_{Kr}.

Only two fast peaks and two overlapping slow peaks are visible in the separation of the helium calibration gas mixture, as seen in Figure 3.12 (left), even though the mixture contains more than four components. It has to be concluded, that the visible peaks are superpositions of the different components present in the mixture. Oxygen and nitrogen most likely act comparable to argon and methane acts comparable to krypton. Hence, these impurities will also pass the gas-chromatographic separation. The use of a strong getter module in the system after the separation is therefore absolutely mandatory in order to remove these contaminations, if present, from the krypton. On the other hand carbon dioxide is known to have similar retention times as xenon, which can even be resolved if the column is set to -30 °C by the observation of a double peak structure [60], where the second one appears at the xenon arrival time. Thus the first peak before xenon is assumed to be carbon dioxide, which is as well cut off in the standard procedure.

4. RGMS results

The off-line analytics system RGMS provides a monitor with a so far unprecedented sensitivity for krypton in xenon assay. It can be used in order to investigate and improve the purity conditions of the LXe dark matter search experiments XENON100 and XENON1T. Furthermore, only constant monitoring of the krypton concentration can provide an estimate of the background originating from ^{85}Kr decays. This chapter starts with monitoring results of the most recent science run of the XENON100 experiment in section 4.1. This *third science run* (SR3) is the first dataset with more than one accessible krypton in xenon assay result. This allows a correlation study which links the impact of air leaks between increase in the krypton concentration and the observation of higher radon activity inside the detector. The second part of the chapter focuses on the interplay between krypton monitoring and improvements in xenon purity by cryogenic distillation. First, section 4.2 discusses results of different distillation runs of the XENON100 experiment. Section 4.3 then focuses on the XENON1T distillation column built by the Münster XENON1T collaboration group, which resulted in the purest xenon sample taken and measured so far [61]. This section therefore concludes with the implications for the RGMS system in order to be able to perform stable measurements in the ppq-regime. An overview over all RGMS results relevant for this work can be found in the appendix A.

4.1. Monitoring the XENON100 experiment

Already the *first science run* (SR1), leading to the 100 life-days dark matter search result of [24] and the *second science run* (SR2) leading to the 225 life-days publication [25] were monitored with samples assayed by the RGMS system. This resulted in (340 ± 60) ppt krypton for SR1 and in (14 ± 2) ppt krypton for SR2. These results agreed well with in-situ krypton analyses as discussed in more detail in chapter 5. However, there was only one measurement available for each run, representing the operating conditions at the time of sample taking. Due to the improved stability of the RGMS, it was possible in SR3 to follow the evolution of the krypton concentration for the first time during the course of a run.

4.1.1. The evolution of the krypton concentration during SR3

In total, there are six different samples that have been taken during SR3. Usually the sample pipette is connected to one of the accessible ports of the XENON100 gas system. The outcomes of the krypton in xenon assay with the RGMS system during SR3 are summarized in Table 4.1.

Name	Sampling date	^{nat}Xe [ccmSTP]	Kr/Xe [ppt]
SR3-1	14/12/2013	0.262 ± 0.008	$0.71 \pm 0.18^{stat} \pm 0.12^{sys}$
			0.71 ± 0.22
SR3-2	09/01/2013	1.95 ± 0.06	$0.95 \pm 0.01^{stat} \pm 0.16^{sys}$
			0.95 ± 0.16
SR3-ATTA	30/09/2013	0.353 ± 0.013	$404 \pm 6^{stat} \pm 70^{sys}$
		0.242 ± 0.009	$465 \pm 4^{stat} \pm 78^{sys}$
			435 ± 79
SR3-3	21/10/2013	2.60 ± 0.09	$9.2 \pm 0.05^{stat} \pm 1.5^{sys}$
		0.55 ± 0.02	$8.9 \pm 0.1^{stat} \pm 1.5^{sys}$
		1.77 ± 0.06	$8.1 \pm 0.1^{stat} \pm 1.4^{sys}$
			8.7 ± 1.5
SR3-4	22/12/2013	0.258 ± 0.009	$10.9 \pm 0.1^{stat} \pm 1.9^{sys}$
		1.70 ± 0.06	$11.4 \pm 0.1^{stat} \pm 2.0^{sys}$
		0.546 ± 0.020	$10.9 \pm 0.1^{stat} \pm 1.9^{sys}$
			11.1 ± 1.9
SR3-Rec	10/02/2014	0.345 ± 0.012	$25.2 \pm 0.3^{stat} \pm 4.4^{sys}$
		0.288 ± 0.010	$26.2 \pm 0.1^{stat} \pm 4.5^{sys}$
			25.7 ± 4.3

Table 4.1.: Summary of the krypton in xenon assay during SR3. SR3-1 to SR3-4 as well as SR3-ATTA were drawn at the XENON100 gas system during SR3. SR3-Rec is sampled from the xenon bottles after the recuperation at the end of SR3. Result of SR3-1 from [52]. SR3-2 to SR3-4, SR3-Rec and SR3-ATTA were drawn and measured during this work. If more than one measurement is available the statistical uncertainty is calculated individually, otherwise the overall uncertainty for a single measurement is applied.

The samples drawn in December 2012 (SR3-1) and January 2013 (SR3-2) were taken prior to the start of dark matter data taking, confirming the very good achieved purity conditions with the krypton distillation performed previous to the detector filling. For these measurements it was not possible to perform more than one RGMS measurement, therefore the standard deviation for a single measurement is applied. 21.5 % for SR3-1 and 17.2 % for SR3-2 as quoted in section 3.2.1, because the latter was already done under the controlled conditions of the ion source, which improved the stability significantly.

For SR3-ATTA a sample pipette different to the standard pipette of Figure 3.3 was used and turned out to be leaky. This hypothesis is supported by observing a strong pressure decrease with the friction manometer, after including the hot getter to the procedure. This can be explained by removed nitrogen and oxygen, which also pass the gas-chromatographic separation. The observed pressure drop can be related to an amount of air contaminating the batch (in roughly 1 l volume). Assuming the krypton fraction of air this can be translated into a krypton amount, which corresponded very well for all three batches to the amount quantified by the mass spectrometer. This shows the possibility of using the friction manometer as a tool for indications of air contaminations. As the measured krypton amount is originating from an air leak, the sample contains no informations about the status of the XENON100 experiment. It is thus removed from any considerations about the krypton evolution during SR3. But despite of the leak the same sample was measured by the *atom trap trace analysis* (ATTA) device employed at Columbia University, New York [51]. The result of (500 ± 140) [62] agrees with the RGMS measurements and therefore confirms its absolute calibration in the high ppt-regime.

SR3-3 was drawn in October, 2013, and showed a higher krypton concentration compared to the samples SR3-1 and SR3-2. It was measured three times with each batch extracted from a different sub-volume of the standard sample pipette. Since the results are consistent within statistical fluctuations, it is concluded that the krypton concentration of the xenon inventory of the XENON100 experiment increased during the course of the current science run.

Sample SR3-4, drawn in December 2013, confirmed that the krypton concentration was still increasing. Hence, an air leak in the detector system had to be present, introducing air to the system. This results in an accumulation of the krypton concentration and, compared to gases as oxygen or nitrogen, it is not removed by the hot getter of the gas system. The RGMS measurements SR3-3 and SR3-4 provoked actions such as a nitrogen flushed bagging of the gas system in order to prevent additional air to leak into the system. As a result of the bagging the science run could be continued.

Dark matter data taking of SR3 ended mid January 2014. After recuperation of the xenon inventory, the sample SR3-Rec was drawn from the storage bottles. It shows a significantly higher krypton concentration than expected from a constant air leak between SR3-2 and SR3-4. This can be explained by the fact that during the process of normal recirculation the GXe passes the gas system at a pressure of ~ 2.2 bar driven by a recirculation pump. At the end of recuperation however, the pressure drops below 1 atmosphere and thus no overpressure prevents external air to leak into the gas system. The leak was later on identified at the membrane of the recirculation pump and supports this explanation.

The evolution of the krypton concentration during SR3 is displayed in Figure 4.1. It shows the clear increase in krypton concentration due to the accumulation of krypton from air, introduced by the leak found at the recirculation pump after the end of SR3. More

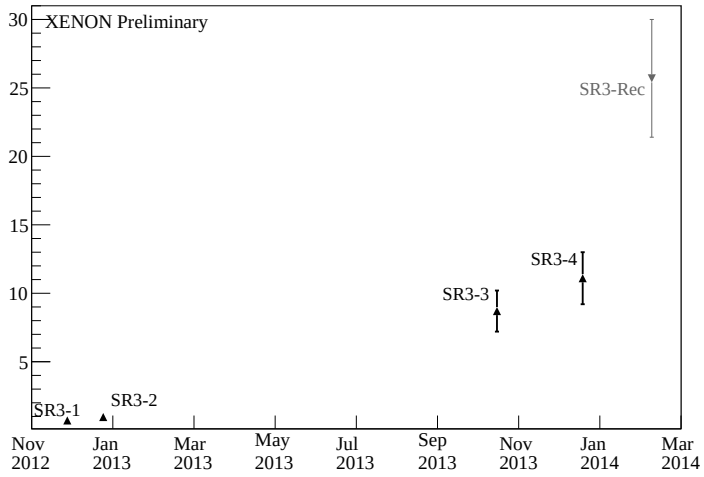

Figure 4.1.: Krypton assay results of the RGMS for the samples taken at Xenon100 during the course of SR3. A clear increase with time is visible, but due to a lack of information towards the middle of the run no conclusion about the gradient can be drawn.

information about the air leak is gained from a correlation study with the measured radon rate inside the XENON100 experiment, which is presented in the next section.

4.1.2. Radon and krypton and the estimate of possible air leaks

As explained in the previous section, the RGMS measurement during SR3 unveiled the presence of a leak, introducing air and, thus, krypton to the xenon inventory of the experiment. An air leak can also be identified by finding correlations between the radon decay rate inside the XENON100 experiment and an outside radon monitor as already done for SR2 [63]. In the following, the air leak size during SR3 is estimated by such a radon correlation study and compared to the air leak size inferred from the krypton evolution druing the run.

The radon isotopes ^{222}Rn and ^{220}Rn arise in the primordial decay chains of thorium and uranium, which are present in almost all materials. Produced by the α disintegration of their mother isotope radium, see Figure 4.2, the radon atoms can get sufficient recoil energy to be repelled out of material surfaces or eventually leave the bulk material by their diffusive motion. If this emanation process occurs in materials housing the xenon inventory, the radon can dissolve in the xenon. The isotope ^{222}Rn with its half-life of $t_{1/2} \simeq 3.8$ days can even diffuse in air after emanation from laboratory surrounding soil, rocks and concrete, leading to activity concentrations of ^{222}Rn up to hundreds of Bq/m^3. Subsequently, the radon can penetrate into the detector system through tiny air leaks or diffusive materials. Inside the XENON100 experiment both radon isotopes are serious background sources due to their subsequent decays as shown in Figure 4.2.

The impact of radon and a dedicated determination of the concentration present in the XENON100 experiment has been studied in [63], where radon decay selection algorithms are

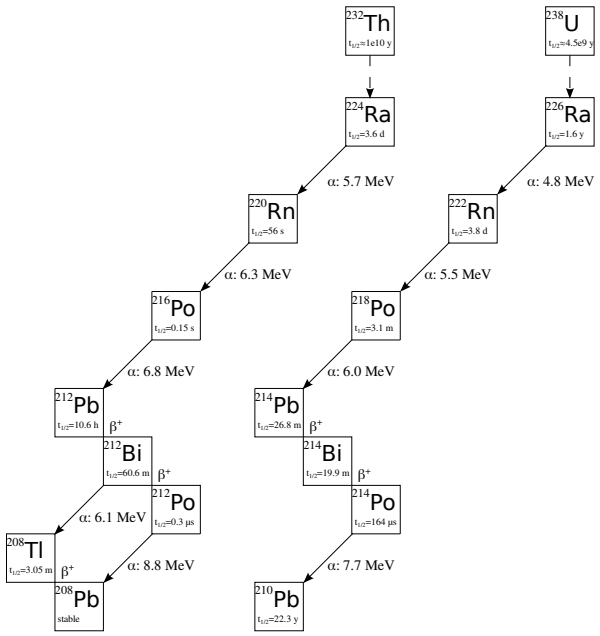

Figure 4.2.: (left) The ^{220}Rn decay scheme occurring in the decay chain of the primordial isotope ^{232}Th [48]. (right) The ^{222}Rn decay scheme occurring in the decay chain of the primordial isotope ^{238}U [48]. ^{222}Rn has a much longer half-life compared to ^{220}Rn, and thus it can diffuse into the xenon inventory through tiny air leaks or diffusive materials.

developed. Basically the energy deposition of the two subsequent α decays can be tagged or a coincidence analysis is performed, identifying the β and α decay of bismuth and polonium (BiPo), occurring in both radon chains with half-lives of the intermediate polonium state of $t_{1/2}\left(^{214}\text{Po}\right) = 164\ \mu$s and $t_{1/2}\left(^{212}\text{Po}\right) = 0.3\ \mu$s. The BiPo-rate is lower compared to the inferred α rates, due to a loss of efficiency in BiPo-tagging. This effect, investigated in [63], originates from the ion drift towards the cathode of the bismuth isotopes which remain charged after the disintegration of the parent lead isotopes. The BiPo-coincidence at the cathode is then very likely to deposit its energy in the metallic mesh and remain undetectable for the algorithms.

As already done for SR2 in [63], the evolution of the radon activity inside the XENON100 detector during the course of a run can be extracted by applying the radon detection algorithms to the dark matter datasets available and averaging the rate on a daily basis. The result is shown in Figure 4.3 for the α decay rates as well as for the BiPo rate, differing by the above explained ion drift of the charged decay products.

In Figure 4.3 a sudden increase in the rates of all radon tagging algorithms is observed around May 15, 2013. Assuming that an absolute leak tight system shows a constant radon activity level due to the unavoidable radon emanation from the detector materials, this abrupt change in activity level can be explained only by additional radon input to the LXe from the outside air diffusing through a newly opened air leak. On November 30, 2013, the radon rate

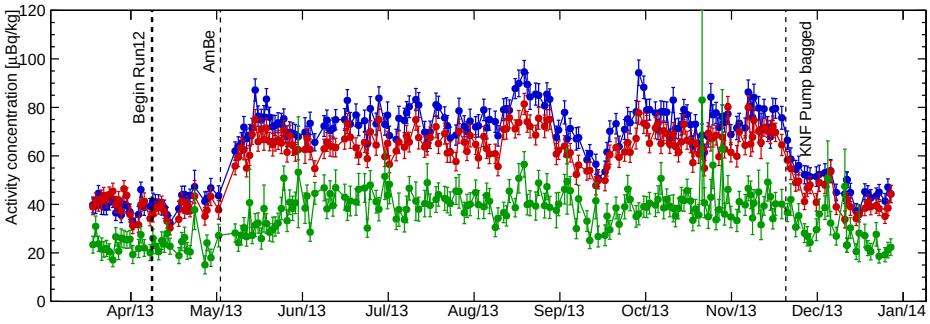

Figure 4.3.: Activity concentration of decays within the ^{222}Rn decay chain as measured during SR3. Blue and red are inferred from tagging the α decays of ^{222}Rn and ^{218}Po. Green represents the activity concentration estimated by the tagging of subsequent BiPo-decays. Clear jumps in activity can be observed in all channels as marked by the dashed vertical lines. Figure from [64].

drops down to the initial conditions of the run. This strongly supports the leak hypothesis, as bagging and nitrogen flushing of the recirculation pump, which is a known source of possible air leaks, was initiated in November 2013 at the same time. Contrary to the evolution of the krypton concentration, the introduction of radon atoms due to a connection to the outside air does not result in an accumulation, but in a constant offset of the rate, because the ^{222}Rn half-life is just in the order of days.

In addition, the measured activity concentration inside the XENON100 experiment can be correlated to the activity concentration of the ambient air measured by a RAD7 radon monitor (from Durridge Company) at the experimental site. This allows to estimate the size of the air leak. Thereby, the following ansatz for the change of the total number of radon atoms $\mathrm{d}N_i$ inside the XENON100 TPC is done:

$$\mathrm{d}N_i = \frac{1}{\tau_{Rn}} \cdot N_i \cdot \mathrm{d}t + \mathrm{d}N_e \ , \tag{4.1}$$

where the first part accounts for the radioactive decay of the radon atoms with the lifetime of τ_{Rn} and the second part is the number of radon atoms diffusing through the air leak linked to the amount of incoming air $\mathrm{d}V$ with a radon concentration of n_e by $\mathrm{d}N_e = n_e \cdot \mathrm{d}V$. Dividing the above ansatz by $\mathrm{d}t$, yields

$$\frac{\mathrm{d}N_i}{\mathrm{d}t} = -\frac{1}{\tau} \cdot N_i + n_e \cdot \frac{\mathrm{d}V}{\mathrm{d}t} \ . \tag{4.2}$$

Under the assumption that after some initialization time, the processes of radioactive decay and external radon input reach an equilibrium state ($\frac{\mathrm{d}N_i}{\mathrm{d}t} = 0$), which is supported by the above mentioned fact, that no longterm increase in radon decay rates is observed, the equation simplifies to:

$$\frac{\mathrm{d}V}{\mathrm{d}t} = \frac{1}{\tau_{Rn} \cdot n_e} \cdot N_i \ . \tag{4.3}$$

Equation (4.3) is solved by integrating over time and replacing $N_i(t)$ and $n_e(t)$ with the measured internal $A_i(t)$ and external $a_e(t)$ radon activity concentrations, respectively. The total amount of air that entered the system up to a time t then is

$$V(t) = \frac{1}{\tau_{Rn}} \cdot \int_0^t \frac{A_i(t')}{a_e(t')} \mathrm{d}t' \,. \tag{4.4}$$

This integration can be performed, as illustrated in Figure 4.4 (left), using just a linear interpolation between the available data points. The total amount of air that entered the system as a function of time, derived by application of equation (4.4) is plotted in Figure 4.4 (right). A linear fit is performed, showing very good agreement with the observed

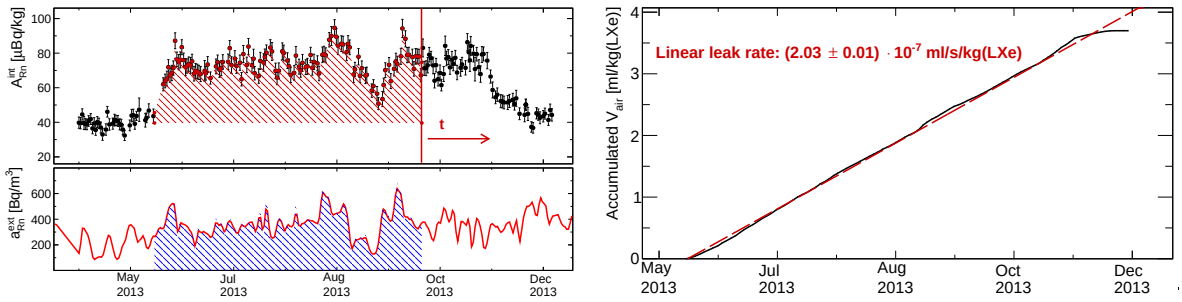

Figure 4.4.: (left) The ratio of the integrated radon activity concentration during SR3 measured inside (A^{int}_{Rn}) and outside (a^{ext}_{Rn}) the XENON100 experiment gives an estimate of the accumulated amount of air introduced by the air leak. (right) A linear fit to the evolution of the accumulated amount of air seems agrees well with the observed data. It can be concluded, that an almost linear air leak was present during SR3, with a leak rate of $(2.03 \pm 0.01) \cdot 10^{-7}$ ml/s/kg(LXe). Figures adopted from [64].

data and confirming the presence of an almost constant air leak between May 15, 2013 and November 30, 2013. The slope of the fit then corresponds to the air leak size, and yields $(2.03 \pm 0.01) \cdot 10^{-7}$ ml/s/kg(LXe). Note that the result is normalized to one kilogram of LXe. This normalization is done for the radon rates, which are calculated for fiducial volume selections of the inner TPC. This normalization might not be valid if extended to the total amount of xenon filled to the detector during SR3. Taking the fact that the air leak was localized in the purification loop at the recirculation pump, the radon from the external air gets first dissolved in the LXe of the TPC, because the output of the loop directly pressurizes the diving bell, as it can be seen in Figure 2.8 (left). The process of mixing the xenon of the TPC with the active LXe veto by diffusion through the interlocking PTFE panels might be in the same order of the ^{222}Rn half-life. Thus, homogeneity inside the total detector system is not necessarily guaranteed.

On the contrary for a measurement with the RGMS it can be assumed, that it reflects the krypton concentration of the complete detector system at the time of sample taking. This is justified, as the krypton isotopes of interest for the RGMS measurements are stable and do not decay before getting distributed homogeneously in the total xenon inventory of the

experiment. The krypton measurements can then also be used for an estimate of the air leak size. The information about the exact opening and closing of the leak obtained from the radon rates are included. Therefore, in Figure 4.5, the results SR3-1 and SR3-2 are averaged and shifted to the approximate date of leak opening, May 15, 2013. The last result of SR3-4 is shifted to November 30, 2013, the day the radon rate dropped back to the initial conditions.

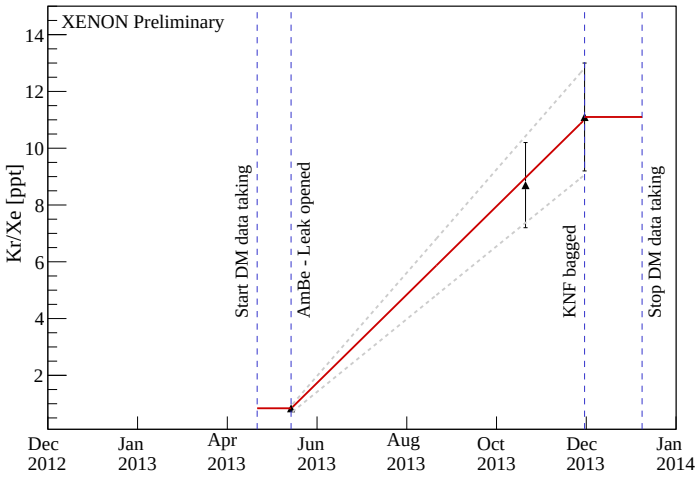

Figure 4.5.: Determination of the krypton concentration evolution during SR3. The RGMS results are shifted such that they correspond to the correct dates of the air leak opened and closed as indicated by the radon monitoring. Systematic offsets of the linear leak rate due to systematic uncertainties in the RGMS measurements are estimated by the two interpolations shown in gray.

The scenario of a linear increase in krypton concentration is supported by the fit resulting in a leak rate of $(5.9 \pm 0.1\,(\text{stat}) \pm 1.0\,(\text{sys})) \cdot 10^{-7}$ $\text{ppt}_{\text{Kr}}/\text{s}$. The leak rate and its statistical uncertainty are derived by a linear fit to the RGMS results with their statistical errors only. But, a relative offset of all RGMS results due to systematic uncertainties of the RGMS measurements, for example an uncertainty in the calibration (ΔSTD), is still possible. In order to account for such an overall offset, the systematic uncertainty of the fit is estimated by two additional interpolations, considering a maximal positive or maximal negative offset of all measurements.

The averaged krypton concentration of SR3 can then be determined by integrating the evolution over time and dividing by the total runtime of the dataset. This yields (6.2 ± 1.0) ppt, which is lower than during SR2 and the lowest value achieved for a science run of the XENON100 experiment so far.

In order to compare the result with the leak rate inferred from the radon rates, the above value is converted to $(8.8 \pm 1.5) \cdot 10^{-8}$ ml/s/kg(LXe) by assuming the krypton to be distributed homogeneously inside the 161 kg LXe and applying the known relative abundance of krypton in air ($V_{\text{Kr}}/V_{\text{air}} = 1.140$ ppmv). This result deviates by a factor of $r = (2.3 \pm 0.4)$ from the leak rate inferred by the radon concentration correlation. But as explained above, especially

for the case of radon, the homogeneity assumption is very critical. Considering that all radon is only distributed inside the TPC and no radon reaches the LXe veto before decay a correction factor of 161/62 kg/kg ~ 2.6 would have to be applied, bringing the leak rates inferred from krypton and radon into very good agreement.

In any case, as long as the same amount of LXe is used in different science runs, the correlation factor of r can be supposed to vary only slightly. This is supported by a similar study of the impact of an air leak in regard of radon activity and krypton measurements during an early commissioning run of the XENON100 experiment reported in [45] and [63] and finding a correlation factor of ~ 2.

Hence, it is possible to perform a first order estimate of the krypton evolution during the course of a run from the radon correlation and the well motivated correlation factor r if not more than one krypton measurement is available. This is done for *science run 2* (SR2). In this run no abrupt increase in radon rate was observed. But, as discussed in [63], a correlation between the external and internal radon activity concentrations could be found as well, indicating the presence of a leak. The integration described in equation (4.4) is performed for the SR2 radon datasets and the result is converted into a comparable leak rate of $(5.6 \pm 1.0) \cdot 10^{-8}$ ml/s/kg(LXe) by applying the correlating factor r. This is then translated into a linear increase in krypton concentration, as shown in Figure 4.6, anchored by the single RGMS measurement available.

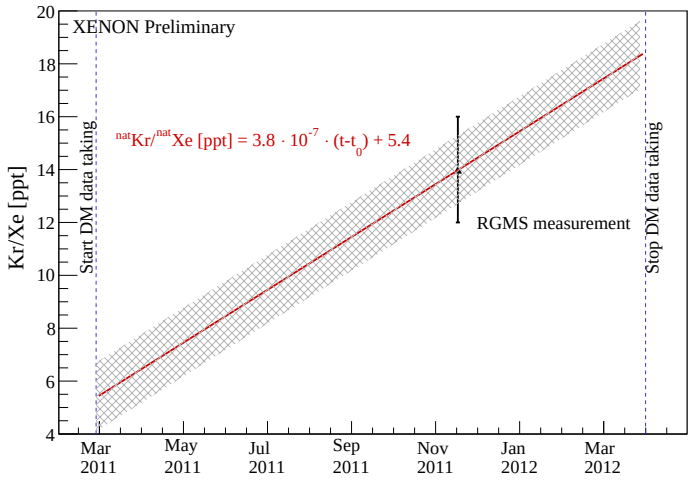

Figure 4.6.: Estimate of the krypton concentration evolution during SR2. The RGMS result anchors the linear increase assumed by the observation of a correlation between the radon activity concentration outside and inside the XENON100 experiment. The relation between air leak sizes inferred from krypton and radon measurements established during SR3 is used.

This result can be used for the search of a modulated signal rate with the XENON100 experiment [39]. The DAMA and CoGeNT experiments reported evidence for annual modulations of their signal rates [36] [38]. Such modulations could be present in the electronic recoil signal of the XENON100 experiment as well. A detailed analysis searching for any

modulated signal rate in XENON100 should therefore include the known evolution of the background originating from ^{85}Kr. Hence, the above calculated evolution of the ^{85}Kr concentration during the 225 live-days dataset is included in the likelihood function of the analysis as a linear term influencing the observed electronic recoil signal rate. It thus minimizes any systematic influence coming from a possible evolution of the krypton concentration. This effect, however, is expected to be sub-dominant, which can be easily seen by comparing the electronic recoil background index for the dark matter search region. An averaged concentration of (12 ± 2) ppt as inferred from the above krypton evolution during SR2, results in an expected electronic recoil background rate of (0.047 ± 0.08) mDRU (evts/kg/day/keV) with the conversion from [45]. This is more than two orders of magnitude smaller than the total background index of 5.3 mDRU reported for this run [25].

4.2. The performance of the XENON100 krypton distillation column

As already pointed out in section 2.4, commercially available xenon is produced by fractionated distillation of air. Because of their similar properties, krypton concentrations in the order of ppm or ppb are still present in commercial xenon gas cylinders. In order to achieve the background goals of XENON100 it was therefore decided to further clean the xenon by distillation in a dedicated distillation column, similar to [50], and purchased from TAIYO NIPPON SANSO. Krypton in xenon measurements with the RGMS system allow detailed investigations of the performance of the XENON100 distillation column.

The filling of the detector is usually done by passing the xenon through the distillation column first, because recuperation from a previous science run and storage in the xenon bottles might have reduced the krypton purity, making a distillation necessary. Between SR2 and SR3 of the XENON100 experiment, three distillations were performed in order to guarantee the xenon purity for SR3. The first distillation procedure was done between September 21, 2012, and October 1, 2012. One sample was drawn at the beginning of the distillation at the column output (KC1-Out), measured already in [45], confirming that a very good purity close to ~ 1 ppt krypton in xenon was achieved. A second sample was drawn at the end of the procedure at the column input (KC1-In), measured during this work. The result is presented in Table 4.2 and yields (123 ± 21) ppt. This confirms that the high purity achieved during SR2 (~ 18 ppt at the end of the run, as seen in Figure 4.6) has been lost. Recuperation and storage seem to influence the xenon purity, especially in the presence of an air leak in the gas system, as confirmed for SR2 in section 4.1.2. At the end of recuperation no overpressure prevents air leaking into the system and contaminating the residual xenon. The same effect is observed after the end of SR3, shown in section 4.1.1. The resulting purification yield of this distillation run, which is defined as the ratio between the input and output concentrations, is $y_p\,(\mathrm{KC1}) = (130 \pm 30)$.

Name	Sampling date	^{nat}Xe [ccmSTP]	Kr/Xe [ppt]
KC1-In	01/10/2012	0.547 ± 0.027	$118 \pm 1^{stat} \pm 20^{sys}$
		0.111 ± 0.004	$125 \pm 1^{stat} \pm 21^{sys}$
		0.341 ± 0.004	$125 \pm 1^{stat} \pm 21^{sys}$
			123 ± 21
KC1-Out	25/09/2012	0.700 ± 0.020	$0.97 \pm 0.09^{stat} \pm 0.16^{sys}$
		0.170 ± 0.005	$1.0 \pm 0.4^{stat} \pm 0.2^{sys}$
			0.97 ± 0.19

Table 4.2.: Results of the distillation performed between September 21, 2012 and Obctober 1, 2012. The output sample (KC1-Out) was drawn directly at the column output and measured in [45]. The input sample (KC1-In) was drawn at the column input and measured during this work. Combining the results gives a purification yield of $y_p\,(\mathrm{KC1}) = (130 \pm 30)$.

After that distillation and filling of the detector a power outage and a subsequent pressure increase inside the detector resulted in a rupture disk failure. This caused a loss of xenon. A new xenon gas cylinder supplied by AirLiquide was then distilled on November 4, 2012. In [45], a sample taken directly from the xenon gas cylinder (KC2-In) which was later on fed into the column, was measured and resulted in (2.8 ± 0.5) ppb. A second sample was drawn at the column output (KC2-Out) and yielded (7.0 ± 1.7) ppt. This corresponds to a purification yield of $y_p\,(\mathrm{KC2}) = (390 \pm 120)$ [45].

A third distillation was then performed directly before the start of SR3. This time, only the krypton concentration of the xenon inventory of the XENON100 detector is known, due to a sample drawn from the gas system shortly after filling the detector. This sample was already presented in section 4.1.1 as SR3-1 with a result of (0.71 ± 0.22) ppt.

The evolution of the krypton concentration during SR3 was already investigated in section 4.1.1, resulting in the characterization of the air leak, which was present during the course of the run. For that reason, the xenon purity could not be kept at the very low level of the beginning of the run. Thus, after SR3 another distillation run was performed, in order to achieve a high purity for another science run (SR4). Thereby, one sample was drawn at the input of the column coming from the storage bottles (KC3-In), which was already presented as SR3-Rec in section 4.1.1. It is summarized in Table 4.3 together with a sample taken at the output of the column (KC3-Out) during this distillation.

Combining the two results the purification yield gets $y_p\,(\mathrm{KC3}) = (40 \pm 10)$. Note, that the result of the column output is the lowest result achieved so far with the XENON100 distillation column, despite of the low purification yield. Additionally this sample was measured already five days after sample taking and yielded a reproducible result. This shows that the RGMS system is very fast in providing information about the current detector status if necessary, although, as an off-line technique, it needs sample pipette preparation and shipment time.

The distillation run was however stopped as ∼30 kg xenon were filled to the detector. This

Name	Sampling date	^{nat}Xe [ccmSTP]	Kr/Xe [ppt]
KC3-In/SR3-Rec	10/02/2014		**25.7 ± 4.3**
KC3-Out	06/02/2014	0.452 ± 0.016	$0.66 \pm 0.09^{stat} \pm 0.11^{sys}$
		1.36 ± 0.05	$0.62 \pm 0.01^{stat} \pm 0.11^{sys}$
			0.64 ± 0.11

Table 4.3.: Results of the distillation process performed after the end of SR3. The input sample (KC3-In/SR3-Rec) was already presented in section 4.1.1 as its measured krypton concentration corresponds to the xenon storage bottles. The output sample was taken at the column output (KC3-Out) and combined this results in a purification yield of $y_p\,(\mathrm{KC3}) = (40 \pm 10)$.

was done because the pressure increased more than expected during filling, which could be an indication of the presence of contaminations like argon changing the vapor pressure of the xenon. This was verified by the measurement of the sample SR4-Fill1, drawn directly from the XENON100 experiment, while only 30 kg of xenon were inside the detector. The result presented in detail in Table 4.4, yielded the very high value of roughly 2 pbb. This confirmed the hypothesis of ∼9 l air entering the system and contaminating the xenon during filling, which caused the unexpected pressure behavior. That this excess in krypton concentration is indeed coming from air, was verified during the RGMS measurement by the friction manometer. The residual pressure observed dropped drastically after including the hot getter to the procedure. As already pointed out during the measurement of SR3-ATTA, this is explained by large quantities of nitrogen and oxygen removed by the hot getter. The observed pressure drop directly can be translated to a krypton concentration of ∼ 2 ppb by assuming the known abundance of krypton in air and estimating the volume around the getter to be ∼ 1 l.

Name	Sampling date	^{nat}Xe [ccmSTP]	Kr/Xe [ppt]
SR4-Fill1	12/02/2014	0.604 ± 0.021	$2040 \pm 10^{stat} \pm 340^{sys}$
		0.509 ± 0.018	$1990 \pm 10^{stat} \pm 330^{sys}$
			2015 ± 335
SR4-Fill2	28/03/2014	2.12 ± 0.07	$1.36 \pm 0.10^{stat} \pm 0.23^{sys}$
			1.4 ± 0.3

Table 4.4.: The distillation KC3 was stopped after filling ∼ 30 kg xenon into the detector, as the operating conditions got very unstable. A sample subsequently drawn from the XENON100 gas system was measured during this work (SR4-Fill1). The achieved purity of another filling procedure was monitored with the sample SR4-Fill2. This filling was successful providing the necessary conditions for another science run.

Subsequently to this measurement, the xenon already filled to the detector was again recuperated and a leak was indeed found at a flexible tube in the XENON100 gas system. With new xenon added, another distillation was performed and successfully filled into the detec-

tor. The krypton concentration was then determined by another sample (SR4-Fill2), which verified a good achieved purity with (1.4 ± 0.3) ppt.

All above RGMS results on the distillation performance of the XENON100 column are summarized in Figure 4.7. The performance of a distillation run is characterized by the

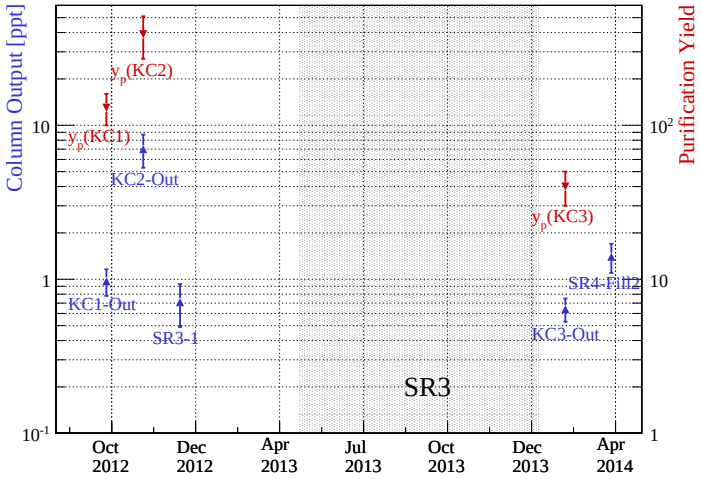

Figure 4.7.: Overview of the results of RGMS measurements assaying the performance of the XENON100 distillation column. In blue the achieved purity at the output of the krypton column for different distillation runs is shown. In red the purification yield y_p for the distillation runs, where as well a sample of the column input was available, is shown. The achieved purity is close to ~ 1 ppt for four of the five assayed distillation procedures. The second distillation run deviates from this result, as the initial concentration was much higher.On the other hand, this run achieved the highest purification yield of $y_p\,(\mathrm{KC2}) = (390 \pm 120)$.

achieved xenon purity at the output of the column and the observed purification yield y_p, if a sample of the in- and output were drawn and analyzed with the RGMS. For four of the five distillation runs presented here, the achieved purity was very close to ~ 1 ppt. The distillation performed directly after SR3 reached the lowest krypton in xenon concentration of the XENON100 experiment and a value so far unattained by other experiments, for example see [50] [65]. Only the distillation of the xenon bottle supplied by AirLiquide resulted in a bit higher value. But in this case the initial contamination was higher. During this run the column achieved also its highest purification yield of $y_p = (390 \pm 120)$, which is lower than the purification yield reported in [50] of $y_p \sim 1000$ for a column similar to the one of the XENON100 experiment. Moreover, the other two distillation runs with an available measurement of the purification yield resulted in even lower values. This, however, could be explained by the fact, that the achievable purity for the XENON100 column levels off at a value close to ~ 1 ppt. The origin of this effect may be in either tiny air leaks that always recontaminate the purified xenon inside the distillation column or in a breakdown of the separation technique by distillation at the ppt-level (at least for the XENON100 distillation column). On the other hand, it could originate also from the sampling and measurement

procedures of the RGMS xenon assay. Residual and unknown background effects might result in an achievable limit for the xenon assay not accounted in the theoretical determination of the detection limit. This possibility is investigated in the next section, together with the presentation of assay results of the XENON1T demonstrator column, showing a measurement of a so far unprecedented xenon purity.

4.3. Xenon assay at the ppq level: The XENON1T distillation column

The design goal for XENON1T is to reach a krypton concentration lower or equal to 200 ppq. In the first place it has to be demonstrated that such purities can be achieved by cryogenic distillation. Neglecting the possibility that the XENON100 distillation column already achieved its purity limit, it is not suitable for XENON1T because of another reason: The total 161 kg xenon inventory of XENON100 can be cleaned at a standard flux of 1.8 SLPM in a couple of days. But this procedure would take months for one distillation process of the complete 3.3 t xenon inventory of XENON1T experiment. Therefore, the commercially purchased XENON100 distillation column cannot be used for the XENON1T experiment. Thus, it was decided to built a new column by the Münster group of the XENON collaboration.

In a phased approach a first demonstrator column with 1 m of package material was built, which is easily scaled up to 3 m, in order to reach a higher purification yield. The column is designed for a xenon flux of 16 SLPM in order to perform distillation runs at the XENON1T experiment on reasonable timescales. The completion of the demonstrator distillation column designed for the use in XENON1T [61] and first successful tests offered the possibility of taking ultra pure xenon samples with so far unprecedented low concentrations. As shown in section 3.2.2 the RGMS system is theoretically able to detect krypton concentrations of a few ppq. The test of the demonstrator column could give the opportunity to test the RGMS system in the ppq-regime, verifying that an assay of such low concentrations is even feasible for the existing set-up.

In order to be able to perform a krypton measurement expected at the sensitivity limit of the RGMS, several prerequisites were necessary. It had to be proofed that the measured signal indeed comes from the krypton concentration of the sample and is not an residual background effect not accounted for in the measurement of the procedure blank.

First, the standard procedure blank does not include all volumes which might contribute in the measurement of a batch. Figure 4.8 (left) shows the sample extraction ports of the gas-chromatographic set-up, explained in section 3.1.2. The gas from the sample pipette is usually extracted by expanding it to the three extraction volumes V_{ext1}, V_{ext2} and V_{ext3}. The expansion subsequently reduces the batch into an amount which can be processed by the gas-chromatographic set-up (in the order of few ccmSTP). During a standard procedure blank measurement only the extraction volumes V_{ext2} and V_{ext3} are frozen to the separating

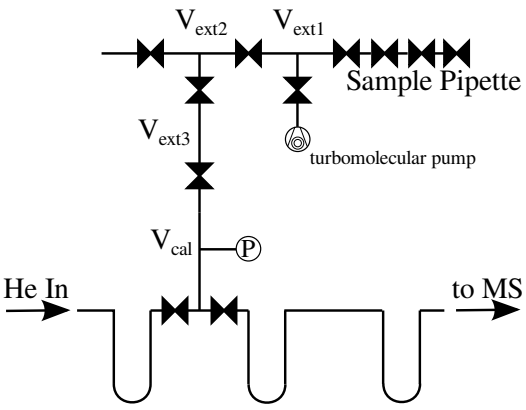

Date		^{nat}Kr [10^{-12} ccmSTP]
28/02/2014	$V_{ext1,2,3}$	(0.230 ± 0.011)
02/03/2014	$V_{ext1,2,3}$	(0.031 ± 0.012)
averaged Blank	$V_{ext2,3}$	(0.013 ± 0.003)

Figure 4.8.: (left) Sample preparation part of the gas-chromatographic set-up. The batch is extracted from the pipette by three extraction volumes, $V_{ext1,2,3}$, which are used to divide the sample by expansion in order to achieve adequate batch sizes. (right) Results of procedure blank measurements. The first two results contain the extraction volume V_{ext1} as well and show the evolution after sample mounting on 28/02/2014. The averaged standard procedure blank, which only includes $V_{ext2,3}$ is shown as well.

column (T2). The extraction into V_{ext1} is performed very fast and still results in overpressure inside this volume, which reduces the impact of tiny air leaks in that part drastically. Thus the influence of this volume to the background of a measurement is supposed to be of minor impact. On the other hand, this volume is unavoidable exposed to air each time a new sample pipette is mounted to the system. Krypton from the air could stick to the stainless steel tube surfaces and could later on get dissolved into the sample. Therefore, the contribution of the extraction volume V_{ext1} was studied before the ultra pure xenon assay by the measurements of two procedure blanks including V_{ext1}. The results are shown in Figure 4.8 (right). A reduction of the blank measurements towards the standard procedure blank value is observed between a measurement directly performed after mounting the pipette to the system and another measurement performed after three days of pumping and baking the extraction volume V_{ext1}.

The second effect might be a background originating from the sample pipettes. The standard sample containers, shown in Figure 3.3, are enclosed by fully metal sealed stainless steel valves which could have non-negligible internal leak rates. In the standard filling and assay procedure the valves are closed with a torque wrench set to 4.5 Nm. It is ensured that the leak rate for the valves used and closed with this torque is less than the sensitivity of a standard helium leak detector. The residual internal leak rates therefore should be dominated by diffusive effects with leak rates $< 10^{-12}$ mbar $\cdot$ l$_{air}$/s. The innermost volume of the standard sample pipette is always protected in each direction by two fully metal sealed valves and one buffer volume filled as well with ultra pure xenon. Hence, if batches of all three sub-volumes are processed an observed gradient would imply internally leaking valves, as the krypton concentrations of the outer volumes would increase first and on a much shorter timescale compared to the impact on the innermost volume. The result of the inner sub-volume should

therefore be completely unbiased by internal leaking valves on the sensitivity level of the RGMS.

The effect of krypton implantation of the pipette surfaces might be more dominant: Like the pipette port volume V_{ext1}, the sampling container itself could trap krypton traces in the stainless steel surfaces, if it has been exposed to a highly contaminated sample or air before. This would lead to contaminations due to outgassing effects, which would increase the krypton concentration of the sample filled into the container by dissolving the residual krypton from the walls.

An estimate of the backgrounds from the sample containers was done by measuring the blanks of the pipettes after pumping and baking them in advance and then closing the pipettes for a couple of days. In order to increase the sensitivity, only the two outer valves of the investigated pipettes were closed, resulting thus in blank results for the complete pipette volume. Division by three might thus only be an upper limit for the innermost volume, because it is protected further against internally leaking valves, as explained above. Three pipettes were examined in that way together with one blank measurement of all connecting and contributing volumes in advance. The results are shown in Table 4.5 and show a clear dependence on the time which was used for the pipette preparation. Intense pumping and

Pipette	pipette preparation	^{nat}Kr [10^{-12} ccmSTP]
PipNo 9	16 days pumping and baking	< 0.007 at 90 % C.L.
PipNo 8	16 days pumping and baking	(0.026 ± 0.008)
PipNo 5	1 day pumping and baking	(0.29 ± 0.01)

Table 4.5.: Measurements of the background contributions of the sample pipettes. The pipettes were pumped and baked over different time periods, before gas was accumulated over 4 days inside the closed pipette, but no normalization is done for that timescale. This is due to the fact that the origins of these background effects, for example outgassing from the inner surfaces might not be linear in time.

baking over 2 weeks ensures a background contribution from the sample containers to be in the order of the minimal detectable amount of krypton by the RGMS. A short sample preparation however results in a background not any more negligible for measurements in the ppq-regime.

Due to these results, PipNo 9 and PipNo 8 were used for the sample taking on February 27, 2014, during a test run of the XENON1T distillation column. The run was performed at a flux of 8 SLPM. The sample pipettes were already mounted two days in advance to the system, in order to have enough time to pump and bake the connecting tubes which were exposed to air while mounting. It was possible to draw two samples independently, one from the column output (MS-LiquidOut) filled into PipNo 9 (lowest background) and one from the column input (MS-InGas) filled into PipNo 8. The filling pressure was ~ 1.7 bar, corresponding to the operating pressure inside the column. The sample MS-LiquidOut was mounted the next

day to the RGMS, and subsequently measured six times, after verifying that the background originating from the connection tubes exposed to air while mounting was sufficiently low. The results are presented in Table 4.6, together with the results for the sample MS-InGas. First it gets obvious, that the results of the different batches fluctuate much stronger than for

Name	Sampling date	^{nat}Xe [ccmSTP]	Kr/Xe [ppt]
MS-LiquidOut	27/02/2014	2.24 ± 0.08	$0.008 \pm 0.005^{stat} \pm 0.001^{sys}$
		2.09 ± 0.07	$0.024 \pm 0.006^{stat} \pm 0.004^{sys}$
		2.85 ± 0.10	$0.015 \pm 0.004^{stat} \pm 0.003^{sys}$
		1.22 ± 0.05	$0.013 \pm 0.007^{stat} \pm 0.003^{sys}$
		0.234 ± 0.008	< 0.050 at 90% C.L.
		1.73 ± 0.06	$0.028 \pm 0.005^{stat} \pm 0.005^{sys}$
			0.018 ± 0.005
MS-InGas	27/02/2013	0.636 ± 0.022	$133 \pm 2^{stat} \pm 22^{sys}$
		1.96 ± 0.07	$143 \pm 1^{stat} \pm 24^{sys}$
		1.12 ± 0.04	$131 \pm 1^{stat} \pm 22^{sys}$
			136 ± 22

Table 4.6.: Measurements of the sample drawn at the Münster demonstrator column. For MS-LiquidOut the statistical variations were much higher than usual. This could be an indication that the measurement of the sample is highly influenced by systematics. MS-InGas shows the very high stability of measurements in the ppt-regime. Combining the results regardless of possible systematic effects in the ppq-regime would result in a purification yield of $y_p = (7500 \pm 2500)$.

samples assayed in the ppt-regime as presented in section 4.1.1. The standard deviation for a single measurement calculated from the results of Table 4.6 is in the order of ~ 40 %, much higher than the averaged value of 2.9 % obtained in section 3.2.1 for measurements in the ppt-regime. But still three of the five measurements with a non-zero result agree within 1σ considering the much higher statistical uncertainties of the individual measurements. Since all measurements were already very close to the detection limit of the mass spectrometer, the estimate for the pedestal size gets dominated by the limited ion counting statistics as shown in section 3.2.2 and illustrated in Figure 3.9. This explains the stronger deviations for the individual outcomes.

But such variations could be as well a first hint, that the measurements taken in the ppq-regime are much more dominated by systematic effects, which are negligible for measurements in the ppt-regime. As already seen by the examination of the background effects originating from the sample pipettes and the connecting tubes, krypton contributions of few 10^{-15} ccmSTP are present due to effects such as krypton implantation on stainless steel surfaces. These effects might be as well more dominant for the measurements of Table 4.6, as for the assay of six different batches it was necessary to store gas over longer time periods ($\sim$ few days) in the extraction volumes $V_{ext1,2,3}$. Enriching residual krypton concentrations from

the walls could then lead to the observed variations. This could especially be the case for the upward fluctuations of the second and sixth measurement, where the assayed xenon batch was stored in the extraction volumes over time periods of several days before the measurement.

Although the five non-zero measurements of Table 4.6 agree very well considering their high statistical uncertainties, the result is quoted as an upper limit of < 26 ppq at 90 % C.L., when referring to the initial sample concentration. This is more conservative as the systematic effects causing the non-zero result are not fully understood. Further investigations at such low krypton concentrations are planned and will increase the comprehension of the RGMS system in the ppq-regime. It has to be underlined that this is the cleanest xenon sample in regard of krypton concentration assayed so far. It showed in principle that the RGMS system can measure such low quantities. Furthermore, the fifth measurement was on purpose performed with a lower amount of xenon, in order to achieve a result comparable with the procedure blank. An upper limit of < 0.012 ccmSTP $^{\mathrm{nat}}$Kr at 90 % C.L. is found, comparable to the procedure blank of (0.013 ± 0.003) ccmSTP $^{\mathrm{nat}}$Kr. This assures that using procedure blanks as an estimate for the background is a valid approach.

The measurement of the sample MS-InGas showed a very stable outcome, as typical for RGMS measurements in the ppt-regime. The results are as well presented in Table 4.6 and yield (136 ± 22) ppt. A lower limit for the purification yield of the XENON1T demonstrator column is calculated, as only the upper limit for the output sample is considered in order to be conservative. Therefore the purification yield is calculated using the original results of Table 4.6 and a lower limit is constructed, resulting in $y_p > 4500$ at 90 % C.L. This is more than a factor ten higher than the best purification yield achieved with the XENON100 distillation column, see section 4.2.

These results clearly indicate, that both the purification system and the equally important off-line analytics system can face the requirements of the XENON1T experiment in regard of the ^{85}Kr background.

5. In situ analysis of ^{85}Kr in XENON100

^{85}Kr is a serious internal background source in the XENON direct dark matter detection experiments as discussed in section 2.4. Its dominant β decay remains indistinguishable from other electronic recoils of the same energy range and moreover it is distributed homogeneously inside the LXe and cannot be reduced by a fiducialization of the active target volume. An off-line determination of the krypton concentration using gas-chromatography and mass spectrometry is shown in chapter 3, but needs careful sampling and a sophisticated measurement procedure. A direct observation of ^{85}Kr decays is however possible via the secondary decay branch shown in Figure 2.13. Within this branch ^{85}Kr decays to the metastable ^{85m}Rb by a β-decay with the endpoint energy of 173.4 keV. This metastable state has a half-life of $t_{1/2} = 1.01$ μs (lifetime $\tau = t_{1/2}/\ln 2 = 1.46$ μs) and subsequently decays into ^{85}Rb with the emission of a 514 keV γ [48]. This clear signature allows an in-situ analysis of krypton concentrations using the existing XENON100 detector despite of the tiny branching ratio of BR = 0.043 % and the associated loss in statistics.

During this Master thesis a detailed ^{85}Kr analysis of the XENON100 data is carried out, improving previous analyses by specifying systematics and increasing accuracy in setting the event selection cuts. The results can be used for a comparison with the off-line analytics performed with the RGMS set-up.

The following chapter first focuses on the basic principles of the XENON100 data analysis in section 5.1 and then continue by explaining data quality and selection cuts for the krypton analysis. This is followed by section 5.3, where the 100 live-days *first science run* (SR1) [24] is used for tuning the analysis due to the higher krypton level at that time. This is followed by the results of the *second science run* (SR2), leading to the 225 live-days publication [25] and the most recent and *third science run* (SR3) with a corresponding analysis in progress at the time of writing.

5.1. The XENON100 data analysis

5.1.1. Data acquisition and raw data processing

The observational data of the XENON100 experiment consist of the waveforms of the 242 PMTs employed in the dual-phase TPC and the active LXe veto. The signals of the PMTs are amplified and fed to *flash analog-to-digital-converters* (FADCs) with a sampling rate of

100 MHz and 14 bit resolution. On-board *field programmable gate arrays* (FPGAs) allow a suppression of baseline-only digitization (zero-length-encoding). Events are recorded if a trigger signal is present, which is generated by combining signals of 68 top and 16 central bottom PMTs. It was improved between SR1 and SR2 [24] [25] by the application of a hardware majority condition admitting only signals where a specified number of PMTs exceed a threshold of ~ 0.5 *photo-electrons* (PE). This reduced the trigger threshold of 300 PE down to 150 PE keeping a >99 % trigger efficiency. In a time window of 400 μs around the trigger signal, the waveform is recorded by the FADCs and stored on disc in a dedicated file format. This time window is more than twice as large as the maximum drift time of electrons over the hole size of the TPC which is 176 μs at the used drift field of 0.53 kV/cm.

The stored waveforms are processed with a ROOT [66] based data processor extracting the physical quantities out of the summed waveforms. The first step is the identification of peaks on the recorded waveform with a peak finding algorithm, for details see [20]. S1 and S2 signals (see section 2.3.1 for clarification) are distinguished by their pulse width, because S2 signals are expected to be broadened due to the secondary scintillation process and the diffusion of the electron cloud during drift. S1 peaks after the S2 are not identified because single electron signals and PMT afterpulses are more dominant in that part of the waveform. The raw data processor then extracts the physical quantities of the peaks, such as the integral, position in the waveform, coincidence level and peak width. In a third step the integrated peak signals are converted into the commonly used unit of PE using the individual PMT gains measured with weekly LED calibrations.

Afterwards the position reconstruction is performed for each event and S2 peak: the distance between the S1 and the corresponding S2 in the waveform is converted via the known electron drift velocity into a z-position, by convention a value < 0. The (x, y)-reconstruction is done differently: the S2 PMT hit pattern of the top array is highly clustered due to the secondary scintillation located very close to the top PMT array. This specific hit pattern is fed to different position reconstruction algorithms: A χ^2-analysis, a support vector machine and a neural network. All of them were trained by the comparison with Monte Carlo simulations. Here the neural network gave best results and thus it is used in standard operation, for details see [67].

The last action of the raw data processor is the application of signal corrections, in order to account for distortions of the detector response. First the z-position has to be corrected for electrical field inhomogeneities, occurring at the bottom edge of the TPC and quantified by detailed electrical field simulations. Then a (x, y, z)-dependent correction on the S1 and S2 signals are performed individually, as light and charge registered by the XENON100 detector depend on the vertex position. The prompt scintillation light S1 reaching the PMT arrays is a function of the solid angle towards the vertex position, the reflection probability at the PTFE walls, the attenuation by Rayleigh scattering, the transmission at the electric field meshes

and the different quantum efficiencies of the PMTs. These effects cause a variation of the detector response to a given energy deposition up to a factor of 3. A (r, z)-2D *light collection efficiency* (LCE) map is derived from calibration sources and shown in Figure 5.1. Axial symmetry of the detector response is confirmed by the comparison of calibration data taken at different source positions around the detector [23]. The application of such a correction map on the raw data leads to uniform response of the TPC in regard to S1 signal strength.

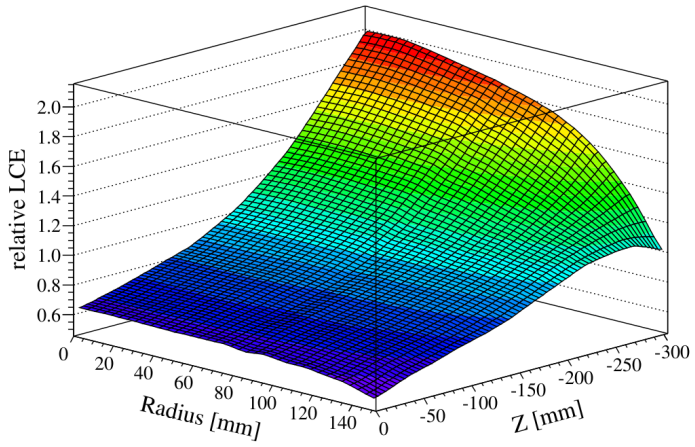

Figure 5.1.: The 3D light collection efficiency map for the S1 signal derived from the 40 keV γ inelastic neutron scattering line obtained with a ^{241}AmBe calibration source. The same map is as well derived for 662 keV γ rays of a ^{137}Cs source and the 164 keV γ neutron activation line of ^{131m}Xe. Axial symmetry is confirmed by comparison of ^{137}Cs data taken at three different source positions. Figure taken from [23].

Similar to the S1 signal, the secondary scintillation light S2 has as well a position dependence. A z-correction is needed, because the electron drift is strongly suppressed by electronegative impurities of the LXe inside the TPC. The electrons get attached to the impurities and the charge signals therefore depend exponentially on the time the electron cloud had to be drifted through the TPC. Hence, the S2 signal is corrected by the exponential law $\exp(t/\tau_e)$ where τ_e is the electron lifetime determined with the charge signal of the ^{137}Cs full absorption peak and t the measured drift time of the event. Furthermore the S2 signal is affected by differences in gas gap size due to mesh wrapping and thus different gain factors for the production of the secondary scintillation light. This is corrected via a (x, y)-2D correction map. With all these signal corrections applied, the corrected and the uncorrected values are available in ROOT data files and can be used for analysis.

5.1.2. Detector calibration and energy scales

For detector comprehension one step is still missing: energy scales relating S1 and S2 signals in terms of PE to the recoil energy in keV. This is absolutely mandatory for any interpretation of observed events. In order to access these quantities radioactive calibration sources are used,

which can be placed very close to the detector by a tube through the shielding materials. ^{137}Cs, ^{57}Co, ^{60}Co and ^{232}Th sources are used for γ calibrations with different purposes. The 662 keV line of ^{137}Cs provides information about spatial dependences of the detector response, as explained in the previous section. The low energy Compton tail of the high energy lines of ^{60}Co and ^{232}Th defines the electronic recoil background region in the discrimination parameter space $\log_{10} \frac{S2}{S1}$. The nuclear recoil acceptance region is obtained by a ^{242}AmBe neutron source. This source additionally provides subsequent neutron induced γ lines in the LXe at 40, 80 and 164 keV with the additional advantage of giving a low energy calibration in the total TPC volume, as the LXe itself gets activated. Other external γ ray sources of that energy regime cannot penetrate deep enough into the LXe due to its high self-shielding capacity. The use of internal sources, mixed with the LXe and decaying in a sufficiently short enough half-life in order to not contaminate the detector is in discussion for XENON1T.

The energy scales are distinct for the S1 and the S2 signal but moreover depend on the interaction types: nuclear and electronic recoils share different ratios of the excitation channels available for a given energy deposition in the LXe, as explained in chapter 2.3.1 and [27].

For the S1 signal the light yield $\mathcal{L}_y$ of a given electronic recoil interaction relates the signal in PE to the corresponding energy deposition in units of keV. For electronic recoils the interpolation between the different measurement points of the available energy calibration lines is done using the semi-empirical NEST-model [68]. In Figure 5.2 the predictions of the model for the number of produced photons per keV depending on the incident particle energy is plotted. Historically motivated, but unfortunately not accessible in the XENON100 experiment due to the high self-shielding capacity of the LXe is the ^{57}Co 122 keV reference γ line. It is thus inferred from the low energy calibration measurements and the model predictions. Moreover it is used to compare different conditions in the different science runs, as the light yield depends on changing parameters such as the residual water concentration in the LXe. Once the light yield dependence of the NEST-model is anchored by the detector response and thus to the specific set-up conditions the S1 energy scale is completely defined. The same procedure holds for the charge signal S2 and the S2 amplification, correlating the signals in PE of an S2 peak into an electronic recoil energy deposition in keV. In a first order approach the production of light and charge can even be assumed to be completely anti-correlated.

The standard WIMP analysis searches for nuclear recoils and only uses the more precisely known S1 energy scale. It is obtained by relating the observed signal to the 122 keV ^{57}Co reference γ-line. This is done by the relative scintillation yield $\mathcal{L}_{eff}$ as shown in equation (5.1) with the additional field quenching factors S_e and S_n. $\mathcal{L}_{eff}$ is taken from measurements performed in external set-ups or detailed analyses of the available XENON100 data as reported in [63] [70] [71]. The different measurement points are interpolated but still the region of nuclear recoil energies below 3 keV is not accessible. The uncertainties of this parameter were

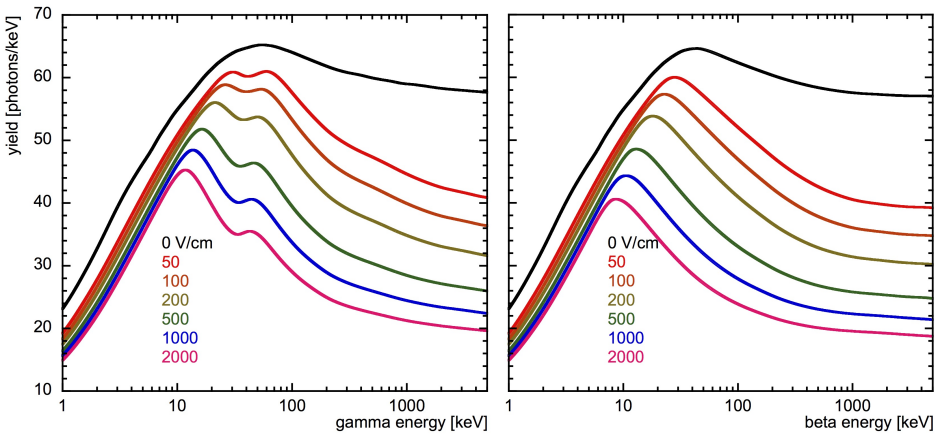

Figure 5.2.: (Left) The NEST prediction for the production of photons due to γ interactions in LXe. The different lines correspond to different drift fields applied to the LXe, as field strength diminishes the recombination probability of created electron-ion pairs and thus decreases the light yield. (Right) The prediction of the model for β interactions. Note the slight differences due to electronic shell effects, even though both interactions undergo electronic recoils. Figure taken from [69].

accounted for in the profile likelihood analysis performed to obtain the dark matter search results presented in [24] and [25]. Although only the S1 nuclear recoil energy scale is used in the standard dark matter search analysis, as well a S2 energy scale can be derived by measurements of the charge yield for nuclear recoils, which is in a first order approximation also completely anti-correlated to the S1 signal.

$$E_{nr} = \frac{S1}{\mathcal{L}_{eff}\left(E_{nr}\right) \cdot \mathcal{L}_{y}\left(122\,\mathrm{keV}\,\gamma\right)} \frac{S_e}{S_n} \,. \tag{5.1}$$

5.2. Selection of ^{85}Kr events

In the ^{85}Kr decay scheme shown in Figure 2.13, it can be seen that the branch with the delayed coincidence pattern has a timescale of $\tau = 1.46$ μs. As this lifetime is two orders of magnitude lower than the total recorded time of one event, the signature of two distinct S1 peaks and the corresponding charge signals should be visible in the same waveform. Therefore selection criteria considering the time requirement and the signal sizes of the corresponding events are applied. Additionally it should be validated that neither of the two interactions subsequently recorded is induced by noise or uncorrelated energy deposition. Therefore this section will begin with the introduction of several data quality cuts providing a clean sample of events.

5.2.1. Data quality criteria

First electronic noise is removed very efficiently by a small set of basic cuts described in the following. A condition on the coincidence level of an identified S1 peak is imposed. The cut requires the signal to consist of at least 2 PMTs exceeding the threshold of 0.35 PE in a 20 ns time window and neither of them is known to have a huge dark rate or is a turned off PMT channel. Details can be found in [47]. As this cut is designed for the use in single scatter dark matter searches, it only verifies the above condition for the largest S1 peak found in the waveform. A second cut with the same condition but imposed on the second largest S1, which should correspond to the β-interaction, is set for this analysis.

The second data quality condition for the S1 peaks is a cut on the width of the peak, which is defined between the left and right boundary at 10 % of the total peak height. Events with very small widths are likely to be noise events, as downward fluctuations of the baseline lower the width of the peak and therefore are efficiently rejected by this cut, details in [47]. Similar to the S1 coincidence condition, this cut is as well adopted for the use in this analysis to work on the second largest S1 signal.

For SR2 and SR3 an entropy value for each peak is defined in order to remove noise more efficiently. This cut is also adopted for the second largest S1 and used in the results of SR2 and SR3 in order to improve noise rejection.

The expected signal will consist of two subsequent S1 peaks and corresponding charge signals. Single scatter event cuts which are used to identify WIMP interactions in the standard dark matter analyses cannot be applied in this analysis due to the expected signature of two subsequent decays in the waveform. Furthermore the largest S2 peak might be an overlap of the two expected signals. This is due to the fact that the 514 keV γ which is emitted at approximately the same position as the β interaction vertex has a mean free path of ~ 3.5 cm in LXe [72]. Thus, it is possible, that the difference in z-position of the two interactions is not large enough to be resolved as two S2 peaks in the waveform. The application on any cuts using the physical quantities extracted of the S2 peaks may therefore not have a well defined acceptance. This implies, that cuts searching for a high signal-to-noise ratio or asymmetries between the signal detected by the top or bottom PMT array are not applied in this analysis. On the S2 peak only one condition is imposed: It has to be verified that at least the largest S2 is above the trigger threshold of 300 PE for SR1 and 150 PE for SR2 and SR3. This verifies that at least one true S2 peak is present in the waveform as the trigger can be released by large S1 peaks as well and this analysis mainly will deal with such cases. It is not applied on the second largest S2, which is just not always expected to be present in the recored waveforms of ^{85}Kr delayed coincidence events.

In order to guarantee that the observed signature is not due to an uncorrelated energy deposition in the TPC, a veto condition is applied. The LXe active veto observed by 62 PMTs should not coincide with a signal in the inner TPC volume. Events with an energy

deposition $\geq$0.35 PE in the active veto around a given S1 peak are therefore rejected.

The acceptances of the cuts used in this analysis are exactly evaluated in [47] in terms of possible WIMP signals. The veto cut has the very high acceptance of $\sim$ 99.5 % independent of the observed signal inside the TPC. The coincidence condition has an acceptance of $>$ 99 % for signals above 10 PE and the S1 width cut $>$ 99.9 % above 6 PE. The cuts tuned on the second largest S1 are assumed to have the same acceptance. In the frame of this study a total acceptance of the data quality conditions of $>$ 99 % can therefore be assumed as by far the most expected ^{85}Kr events will have high S1 signals for the γ and the β interaction. Therefore the acceptance loss in the few PE region of the above cuts will be of minor impact.

5.2.2. ^{85}Kr selection cuts

After ensuring that observed events are not induced by noise or correlated to energy deposition in the active LXe veto, ^{85}Kr events can be tagged. Three conditions are used: first, a timing condition verifying that the time distance is in the order of $\tau = 1.46$ μs between the β and the subsequent γ interaction. Second, cuts on the S1 energy for the 514 keV γ on the largest S1 signal and for the β-decay with 173.4 keV endpoint energy on the second largest S1 are imposed. The waveform of such a typical ^{85}Kr event of SR1 is shown in Figure 5.3.

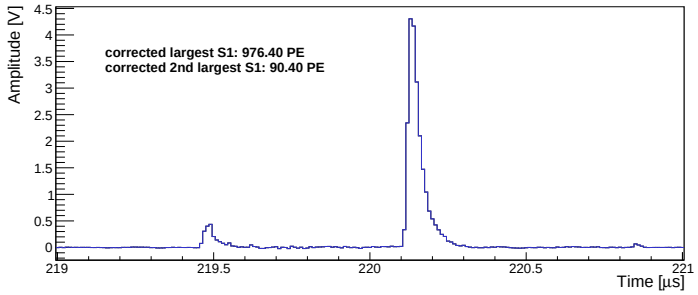

Figure 5.3.: The summed waveform registered by the raw data processor of the XENON100 experiment of a typical ^{85}Kr delayed coincidence event. The lower S1 signal corresponding to the β decay is followed on atypical timescale of $\tau = 1.46$ μs by a higher S1 signal corresponding to the γ interaction.

The clear signature of the delayed coincidence branch of ^{85}Kr gives the possibility of an almost background-free measurement. But in the decay chain of ^{232}Th the isotope ^{220}Rn appears with the short half-life of $\sim$1 minute. In the subsequent decays, a BiPo-coincidence can be found, as shown in Figure 4.2 (left): a β-emission from ^{212}Bi into ^{212}Po with endpoint energy of 2254 keV and a delayed α-decay within a half-life of $t_{1/2} = 0.3$ μs, very similar to the one of ^{85m}Rb. In general, the α-decay with its energy of $\sim$8.78 MeV should be distinct from the 514 keV γ in energy, but effects as incomplete energy deposition inside the active LXe can reduce the energy measured by the XENON100 detector. This can for example happen at the edges of the TPC, when the α gets implanted to the PTFE walls and is not fully stopped in the LXe. Such effects would then lead to misidentified ^{85}Kr events. The same argumentation

holds for the BiPo-coincidence of the ^{238}U decay chain, see Figure 4.2 (right), where the radon isotope ^{222}Rn appears. This BiPo-coincidence as well has the signature of a β and subsequent α decay, but with the intermediate half-life of $t_{1/2} = 164$ μs. Both radon isotopes are dissolved in the LXe of the XENON100 experiment due to emanation from detector walls, or in the case of ^{222}Rn, as well due to the possible diffusion through tiny air leaks from the outside air, as shown in section 4.1.2. Therefore both BiPo-coincidences of the radon decay chains have to be considered as a possible background source in the detection of delayed ^{85}Kr coincidences.

The delay condition is set to a time window from 0.5 to 4.9 μs in which two S1 signals have to be registered. The lower threshold is chosen such that possible background from ^{220}Rn is minimized by keeping a highest possible acceptance. But due to the very similar half-lives, a complete avoidance of this background is very difficult. The upper threshold ensures that the cut includes three lifetimes of the ^{85m}Rb γ-decay. Extending the cut to more lifetimes would not have increased the acceptance drastically but on the other hand would rise the possibility of picking up background originating from ^{222}Rn-decays. The acceptance of the cut can be calculated analytically to

$$a_\tau = \frac{\int_{0.5}^{4.9} \exp\left(-t/\tau\right) \mathrm{dt}}{\int_{0}^{\infty} \exp\left(-t/\tau\right) \mathrm{dt}} = 67.5\% \; . \tag{5.2}$$

The energy conditions on the selection of the largest and second largest S1 peaks have to take into account the finite energy resolution of the XENON100 detector. As a physical device any energy deposition is subject to statistical fluctuations and therefore the energy distribution is smeared out. The resolution measured during SR1 with different γ calibration lines explained in section 5.1.2 is shown in Figure 5.4. As the resolution only changed slightly during the different runs, the values of 11.9 % for a 514 keV γ and 13.1 % for a 173.4 keV β are kept for the complete analysis.

The energy spectrum of the β decay is expected to follow the distribution shown in Figure 5.5 (left) given by a GEANT4 [73] simulation. As the spectrum decreases with increasing energy, 2σ of the detector resolution added to the endpoint energy should yield no loss in acceptance anymore. The lower cut threshold is set to 5 PE which translates to an energy deposition of approximately 2 keV as derived in [35]. A systematic error of the cut acceptance is determined by assuming another spectral shape (box-like to presume a very different underlying model as shown in Figure 5.5 (left)) and varying the lower threshold. This yields $a_\beta = (99.9 \pm 1.1)$ %.

For the γ condition, a 3σ region in resolution is used in order to achieve a high acceptance. The cut thresholds still depend on the specific light yield at 514 keV which might be distinct for the different datasets. Therefore the systematic uncertainty of this cut acceptance is derived by comparing different assumptions for the light yield, either with the underlying

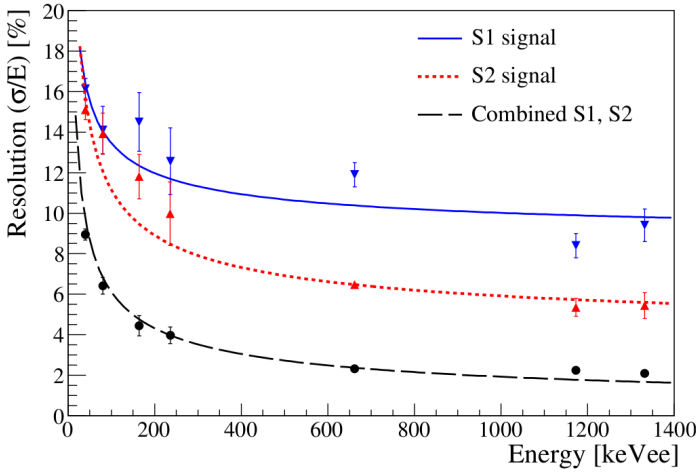

Figure 5.4.: The energy resolution of the XENON100 detector determined via several calibration γ-lines for SR1. The functional dependences of the best fit results are shown for the S1, S2 and combined energy scale. Figure from [23].

NEST-model or with a direct determination on SR1 data, as shown in Figure 5.5 (right) and in detail explained in section 5.3. The acceptance yields $a_\gamma = (99.7 \pm 2.7)$ %. All ^{85}Kr delayed coincidence selection criteria are summarized in Table 5.1.

Cut	Definition	Acceptance
Data Quality Cuts		>99 %
Delay Cut	0.5 < time difference < 4.9	67.5 %
β Cut	5 < corrected largest S1 < 219 · yield	(99.9 ± 1.1) %
γ Cut	330 · yield < corrected 2^{nd} largest S1 < 698 · yield	(99.7 ± 2.7) %

Table 5.1.: Summary of the used cuts in order to identify valid ^{85}Kr events. Their acceptances together with their systematic errors are shown as well.

5.3. Calibration of the analysis method on *science run 1* (SR1) data

The dataset of the 100 live-days publication [24] is used for a first approach in this analysis. This is due to the fact, that a higher krypton level inside the detector was observed as a result of a leak during maintenance work at the gas system previous to the start of the run. In [52] the krypton concentration of this run was measured to be (340 ± 60) ppt by mass spectrometry with the set-up described in chapter 3. The comparison of the spectral shape with Monte Carlo background simulations supported this result with a value of (350 ± 50) ppt [47]. This leads to the expectation of approximately 150 ^{85}Kr delayed coincidence events inside the complete 62 kg LXe of the TPC over the life-time of this science run. SR1 gives therefore a possibility to test this analysis in conditions were sufficient statistics are available and an

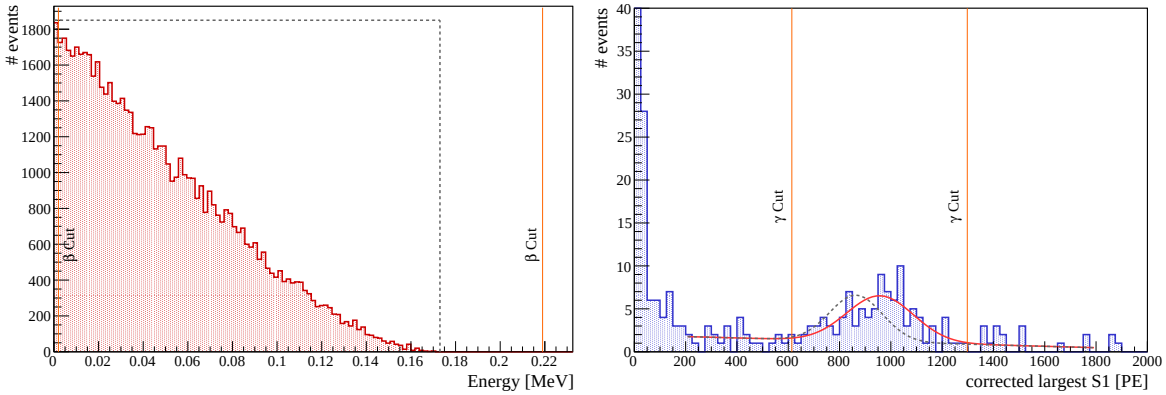

Figure 5.5.: (Left) The energy spectrum of the expected β-decay with an endpoint energy of 173.4 keV as given by a GEANT4 [73] simulation. The cut thresholds are shown in orange and the gray dashed line represents the spectral shape assumed for a determination of the systematic uncertainty. (Right) The energy distribution of the corrected largest S1 after application of a delay and a β condition inside the total TPC volume. The observed peak structure close to the expected value of the 514 keV γ full absorption peak is fitted with a gaussian function and an assumed linear background. The gray dashed line represents the expectation of the NEST model which is used for an estimate of the systematic uncertainty of the cut acceptance.

evaluation of the influence of the selection cuts on real data can be done. This offers the opportunity to specify the systematic effects of this analysis.

5.3.1. SR1 light yield

The first step is the definition of the selection cuts, mainly the definition of the light yield for the expected γ and β signals. The reference light yield for the 122 keV ^{57}Co line is used to anchor the NEST model, as explained in section 5.1.2. The value for this reference light yield was reevaluated by the XENON collaboration and yields $\mathcal{L}_y\,(122\,\mathrm{keV}\,\gamma) = (2.09 \pm 0.04)$ PE/keV. Using the latest version of the NEST-model [69] the light yield at a given drift field of 0.5 kV/cm for a 173.4 keV β interaction and a 514 keV γ interaction can be read out from Figure 5.2. This yields by chance for both the same value of $\mathcal{L}_y\,(173\,\mathrm{keV}\,\beta) = \mathcal{L}_y\,(514\,\mathrm{keV}\,\gamma) = (1.68 \pm 0.08)$ PE/keV.

With this light yield the β cut is set in terms of PE and a crosscheck of the NEST results with the observed data can be performed. The delay and the β condition are applied to the SR1 data first. A peak structure in the spectrum of the largest S1 close to the expected value of 860 PE as shown in Figure 5.5 (right) can be observed. A gaussian fit to the peak including an unknown but linear background contribution from either ^{220}Rn BiPo- or random-coincidences, results in a light yield of $\mathcal{L}_y\,(514\,\mathrm{keV}\,\gamma) = (1.86 \pm 0.04)$ PE/keV, slightly higher than the result of the NEST model. This deviation might have its explanation in possible scatters of the 514 keV γ. Compton scattering followed by the absorption of the γ is unresolvable in S1 as the time difference of these two signals is smaller than the sampling

time of the FADCs. The combined light yield of these two interactions might be higher, which can be seen in Figure 5.2 (left). As no single scatter cuts can be applied in this analysis, such a verification of this effect would require a full Monte-Carlo simulation. But for the intention of this analysis it is sufficient to use the modified and slightly higher light yield of the direct measurement performed in Figure 5.5 (right). But, as already explained in section 5.2.2, this deviation in light yield is taken into account in a systematic error on the cut acceptance. This is done by calculating the acceptance of the used cut assuming the lower light yield predicted from the NEST-model.

5.3.2. The observed event distribution

The above defined cuts are now applied to the dataset. The averaged krypton concentration can then be calculated using equation (5.3):

$$\frac{^{\mathrm{nat}}\mathrm{Kr}}{\mathrm{Xe}}\left[\frac{\mathrm{mol}}{\mathrm{mol}}\right] = \frac{\#\text{selected events} \cdot M_{Xe}}{\mathcal{N}_a \cdot (^{85}\mathrm{Kr}/^{\mathrm{nat}}\mathrm{Kr}) \cdot T \cdot \lambda \cdot a_{comb} \cdot \mathrm{BR} \cdot m_{Xe}} \tag{5.3}$$

with $\mathcal{N}_a$ the avogadro number, $(^{85}\mathrm{Kr}/^{\mathrm{nat}}\mathrm{Kr})$ the measured isotope abundance at LNGS, T the lifetime of the run, λ the decay probability of 0.000176 decays/day, $a_{comb} = (67 \pm 2)$ % the combined selection cut acceptance, BR the branching ratio of the delayed coincidence decay mode, m_{Xe} the xenon mass considered for the analysis and M_{Xe} the molar mass of xenon.

Different fiducial volume cuts are applied in order to obtain information about spatial homogeneity and possible edge effects. The 48 kg fiducial volume used in [24] and the 34 kg fiducial volume used in [25] as well as the total TPC volume consisting of 62 kg LXe are evaluated. The spatial distribution of the events is shown in Figure 5.6, which is very homogeneous within statistical fluctuations. The results of the two different fiducial volumes differ only slightly and agree within their statistical uncertainties as well. Data corrections, cuts and acceptances could be different for the outermost regions of the TPC, as the detector is still not fully characterized and understood in this region. Thus, the results considering the total TPC volume should be taken more carefully.

This event selection is now used to crosscheck the analysis. In Figure 5.7 (left) the time difference between the largest and second largest S1 is plotted for all the selected event of the total TPC volume, which should follow an exponential decay with the time constant $\tau = 1.46\ \mu$s [48]. The fit yields $(1.3 \pm 0.2)\ \mu$s which is in very good agreement with the expectation. Furthermore in Figure 5.7 (right) the energy distributions in PE of the largest and second largest S1 are shown for the selected events. As expected, the shape of the β decay spectrum of Figure 5.5 (left) and the gaussian type of the 514 keV γ peak are observed within statistical fluctuations.

Possible systematic influences are checked as well. Already mentioned in section 5.2.2,

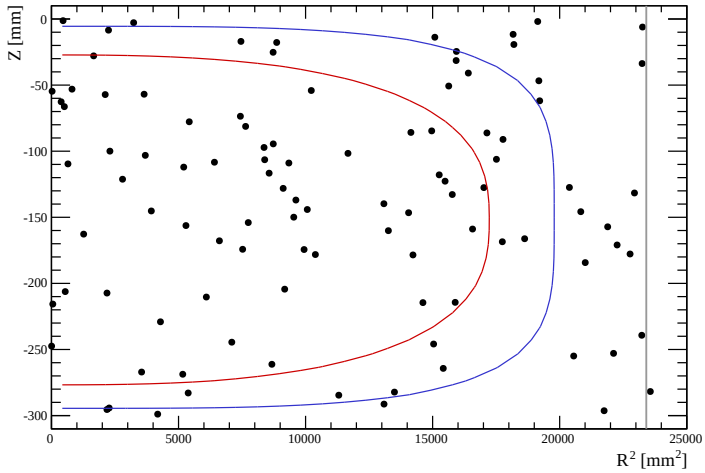

mass [kg]	# events	Kr/Xe [ppt]
34 kg	59	(370 ± 50)
48 kg	80	(350 ± 40)
62 kg	103	(350 ± 40)

Figure 5.6.: (Left) The observed event distribution inside the XENON100 TPC of selected ^{85}Kr delayed coincidence events after application of the data quality cuts and the γ, β and τ conditions. The red line indicates the 34 kg, the blue line the 48 kg fiducial volume. (Right) Results.

there is the possible background originating from BiPo-coincidences of the ^{220}Rn decay chain. In Figure 5.7 (left) a contribution in the first bins of the full TPC event selection due to the short lifetime of the BiPo-coincidence of $\tau = 0.43$ μs might be present. However, these misidentified background events should mainly occur at the edges of the TPC, as insufficient energy deposition in the LXe is required for the α decay to leak into the γ acceptance window. If an additional 34 kg fiducial volume cut is applied in order to obtain a cleaner sample, the assumption of a background contribution with a short lifetime is supported as the fit now yields a slightly higher lifetime of (1.9 ± 0.4) μs, but still in good agreement with the expected value.

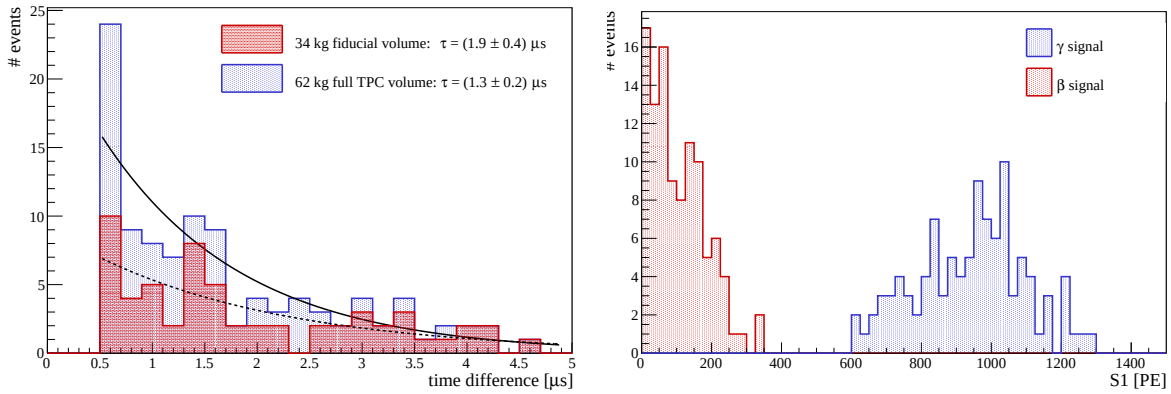

Figure 5.7.: (Left) The time distance between the largest and second largest S1 of the selected events. Blue represents the total TPC volume and red a 34 kg fiducial volume. The black curves correspond to the applied exponential fits. (Right) The energy distributions for the corrected largest and second largest S1 of the same event selection and the total TPC volume.

No strong dependence of the analysis results on the fiducial volume selection is observed. Furthermore, the effect of an additional background in the outer regions of TPC might be compensated by a loss in ^{85}Kr selection acceptance in this region: as already mentioned the 514 keV γ has a mean free path of $\sim$3.5 cm [72]. It can therefore escape the TPC volume if the previous β decay occurs close enough to the edges of the TPC. This effect could only be quantified in a full Monte Carlo simulation. Although these effects might compensate each other in this run, it shows again that results of the full TPC volume should be treated carefully. A reduction to the innermost volume might be more reasonable. This consideration results in a first estimate of the $^{\text{nat}}$Kr concentration during SR1 of $^{\text{nat}}\text{Kr/Xe} = (370 \pm 50\,(\text{stat}) \pm 10\,(\text{sys}))$ ppt.

5.3.3. Further investigations about the charge signal S2

The presence of a possible background is faced in an additional study of the charge signal S2, an information so far only used for the position reconstruction and the condition of requiring at least one valid S2 signal. The reason why the charge signals are more difficult to treat is the effect of the expected possible overlap of the S2 originating from the β and the γ interaction. Nevertheless, the observed signal of the largest S2 should at least correspond to the energy of a 514 keV of the γ interaction. Additionally the α energy deposition of the background from the BiPo-coincidence is expected to have a lower charge yield than γ interactions due to the very high stopping power of α particles. Hence, the BiPo-coincidence might be separable from the ^{85}Kr delayed coincidences in S2.

The energy scale applied to the S2 signal is inferred from calibration measurements. Only the bottom PMT array is used for S2-analyses, as the top PMTs show saturation effects influencing the energy scale. The ^{137}Cs 662 keV γ line serves as an estimate of the S2 amplification factor of the expected energy regime. For SR1 a value of 348.5 PE/keV is assumed [74], which translates to $\sim$ 180 000 PE for a 514 keV γ interaction. A similar value is inferred from a study of the calculated secondary scintillation gain of single electron signals [75] together with the NEST predictions [69].

In Figure 5.8 (left) the energy spectrum of the largest S2 signals is shown. A very broad population of events is observed mainly at slightly lower values than expected. Therefore a cut with a high acceptance can only be set as shown in Figure 5.8 (left). Such a condition only rejects very low S2 signals. The observed smearing towards lower S2 signals is possibly explained by scattering effects: If the 514 keV γ undergoes a Compton scatter before full absorption, there is the possibility, that these two interactions are resolved in S2 (which is not possible in S1). Therefore the largest S2 might not correspond to a 514 keV interaction, but to somehow lower energy deposition.

This effect of double or multiple scatters is avoided by using the sum of all registered S2 peaks. Then the signals of the majority of interactions of the γ and the β add up. The summed

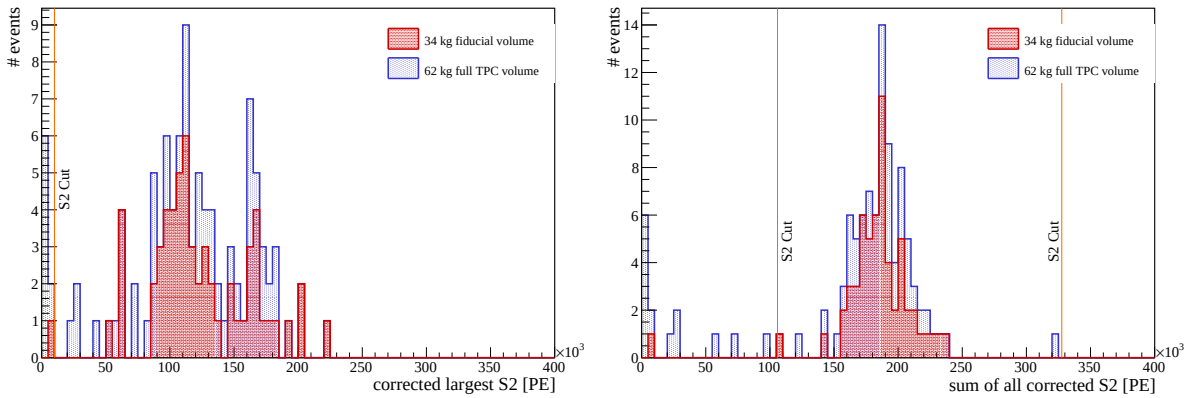

Figure 5.8.: (Left) The energy distribution in PE of the corrected largest S2 is plotted for the ^{85}Kr delayed coincidence selection. As the expected peak structure is very broad only a cut eliminating very low signals can be applied. (Right) The energy distribution of the sum of all S2 peaks found in the waveforms. Valid signals should consist of a value between the 514 keV and 687 keV. A 5σ resolution cut is applied.

signal is therefore expected to be in the range of $[514, 687]$ keV and following a superposition of a gaussian distribution and the shape of the β decay. A 5σ resolution band for the required energies is added according to the S2 resolution of Figure 5.4 in order to account for higher uncertainties in the charge yield determination. This should yield an acceptance very close to 100 %. The resulting event distribution and the cut thresholds are shown in Figure 5.8 (right). The observed population can now easily be separated from events with a very low S2 signal, which should correspond to incomplete α energy deposition originating from the ^{220}Rn decay chain. Hence, the application of this cut should provide a cleaner event selection.

In Figure 5.9 the event distribution inside the TPC is shown. As expected most of the

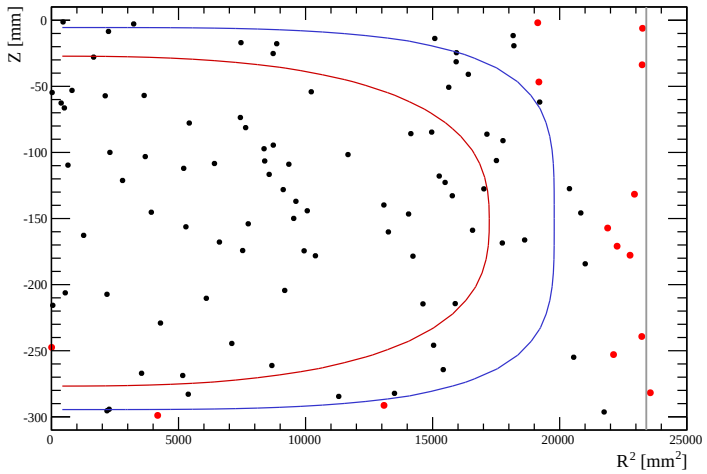

mass [kg]	# events	Kr/Xe [ppt]
34 kg	58	(360 ± 50)
48 kg	79	(350 ± 40)
62 kg	89	(310 ± 30)

Figure 5.9.: (Left) The observed event distribution inside the XENON100 TPC of selected ^{85}Kr delayed coincidence events after application of all selection cuts including the condition on the S2 signal. Events in red are removed by the S2 cut only. The red line indicates the 34 kg, the blue line the 48 kg fiducial volume. (Right) Results.

events removed by the additional cut on the charge signal occur at the edges of the TPC. There the probability for BiPo-coincidences mimicking the ^{85}Kr delayed coincidence is higher because the α can deposit only parts of its energy inside the TPC. But effects as insufficient charge collection due to field inhomogeneities could lower the S2 cut acceptance and this is as well most likely to occur close to the field shaping electrodes of the TPC. As a final and conservative result therefore only the innermost 34 kg fiducial volume is considered $^{\text{nat}}\text{Kr/Xe} = (360 \pm 50\,(\text{stat}) \pm 10\,(\text{sys}))$ ppt. This is in very good agreement with the RGMS value of (340 ± 60) ppt.

5.3.4. A comparison to previous delayed coincidence analyses

The XENON100 collaboration already performed a study on the ^{85}Kr delayed coincidence for SR1 and quoted the result of (294 ± 66) ppt [47]. The analysis reported here was performed completely unbiased as a comparison was only made after the obtainment of first results with this new method. The final event distributions are compared in Figure 5.10.

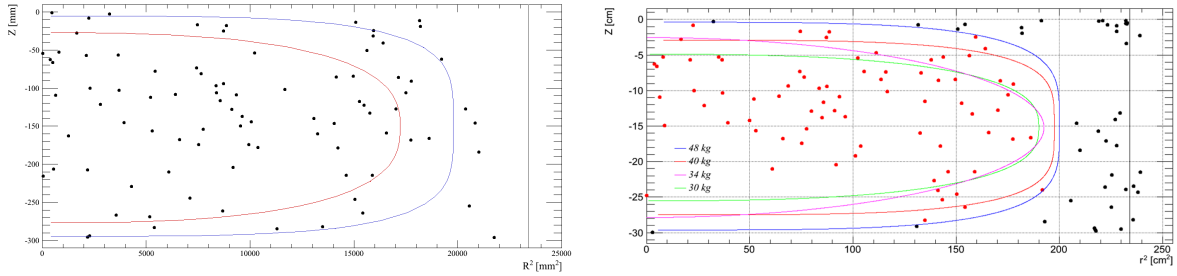

Figure 5.10.: (Left) The observed final event distribution of the SR1 dataset after application of all ^{85}Kr selection criteria described in this work. The lack of events close to the edges of the TPC is expected in this analysis and can be avoided with the use of fiducial volumes. (Right) The final distribution of a previous analysis [76]. The lack of events the central bottom region of the TPC is due to the use of uncorrected signals and not anymore observed in the analysis performed in this work.

Two main differences are apparent: In this analysis less events close to the edges of the TPC are detected. This can be explained by two already mentioned effects: the loss of acceptance of the γ condition close to the TPC walls, as the 514 keV γ might escape out of the sensitive volume, and, second, effects of insufficient charge collection lower the acceptance of the S2 condition. The other main difference is the lack of events directly above the center of the bottom PMT array in the previous analysis. The origin of this event inhomogeneity was not known. As this lack does not occur in this analysis there has to be a physical reason, which was found by comparing the selection criteria: The previous analysis used the uncorrected signals for the γ and the β condition. The detector however has a very high LCE close to the center of the bottom PMT array, see Figure 5.1. The application of the correction factors, which are in the order of $\sim$0.6 in that region, prevent events of that regions to fail the S1

conditions, due to their very high signals. Hence, the quoted result of this analysis is slightly higher and closer to the expected value inferred from the RGMS measurement.

A further comparison of the cut thresholds showed other minor differences. The delay condition has a higher acceptance of $\sim 81\,\%$ in the previous analysis by setting the lower time threshold to only 0.3 μs and the upper threshold to 10 μs. This, however, includes the possibility of picking up background from BiPo-coincidences in the lower time regime from the ^{220}Rn decay chain and in the upper time regime from the ^{220}Rn decay chain. Therefore the analysis of this work takes the loss in acceptance by ensuring a much cleaner sample.

Other differences were the improvements of the selection cuts: adoption of the data quality cuts used in the standard dark matter searches for the largest and second largest S1, detailed considerations about light yield, charge yield and resolution and the estimation of systematic errors on the cut acceptances. Thus the results of this analysis are more robust as systematic uncertainties are included.

5.4. Results of *science runs 2* and *3* (SR2 and SR3)

With this knowledge, the datasets of the 225 live-days publication (SR2) [25] and the most recent dataset with 153.6 live-days (SR3) are evaluated. For both runs the krypton level was reduced compared to SR1. The ratio between the background from BiPo-coincidences originating from radon decays and the signal from ^{85}Kr delayed coincidences is thus shifted towards the background for this analysis. Moreover, due to tiny air leaks, as already investigated in section 4.1.2, additional radon was introduced to the xenon inventory in SR2 and SR3. It is thus expected to observe more background events originating from the BiPo-coincidence of the ^{222}Rn decay chain. On the contrary, ^{220}Rn has a very short half-life of $\sim$1 minute and therefore should not diffuse through an air leak into the LXe.

5.4.1. SR2

The RGMS measurement for this run was (14 ± 2) ppt, this is significantly lower compared to SR1, such that about one order of magnitude less events are expected. As already mentioned in section 5.2, the entropy cut (further electronic noise rejection) is additionally applied to the data. The delay condition was left unchanged. The reference light yield of 122 keV for this run is $\mathcal{L}_y\,(122\,\mathrm{keV}\,\gamma) = (2.28 \pm 0.04)$ PE/keV [47]. This translates by application of the NEST-model to $\mathcal{L}_y\,(173\,\mathrm{keV}\,\beta) = (1.85 \pm 0.08)$ PE/keV. Using the directly measured light yield at 514 keV of SR1 and its ratio to the reference light yield determined during the analysis of SR1, the value of the light yield of a 514 keV γ for SR2 is $\mathcal{L}_y\,(514\,\mathrm{keV}\,\gamma) = (2.03 \pm 0.07)$ PE/keV. The S2 amplification was evaluated recently [77] with a value of (366.5 ± 0.5) PE/keV by studying the ^{137}Cs calibration data of this run.

The event distribution observed after application of all cuts mentioned above is shown in

Figure 5.11. Due to the lower krypton level and the longer lifetime of the run, a relative increase in the number of events at the edges of the TPC is apparent if no S2 cut is applied.

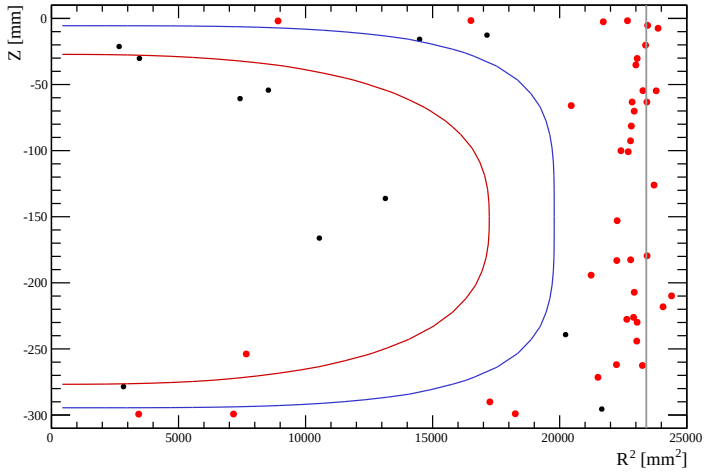

mass [kg]	# events	Kr/Xe [ppt]
34 kg	5	14^{+8}_{-6}
48 kg	8	16^{+7}_{-5}
62 kg	11	17^{+6}_{-5}

Figure 5.11.: (Left) The observed event distribution inside the XENON100 TPC of selected ^{85}Kr delayed coincidence events after application of all selection cuts including the condition on the S2 signal. Events in red are removed by the S2 cut only. The red line indicates the 34 kg, the blue line the 48 kg fiducial volume. (Right) Results.

This is underlined in Figure 5.12 (left), where the S2 spectrum of this run is displayed. More events with low S2 signals are clearly present and removed by the S2 condition. A verification of the efficiency of the S2 cut is given in Figure 5.12 (right). The delay time distribution of events which not pass this additional cut yields a lifetime of $\tau = (0.38 \pm 0.06)$ μs in good agreement with the expected lifetime from the BiPo-coincidence of $\tau = 0.43$ μs. On the other hand the 11 events passing this additional cut show a delay distribution comparable with the expected ^{85}Kr delayed coincidence, despite of the low statistics. A possible acceptance loss of the S2 cut for the outer TPC volume cannot be excluded, however all three evaluated volume selections give consistent results for this run.

The need of the additional S2 cut is demonstrated by the waveform of the one event of the 34 kg fiducial volume which does not pass the condition, shown in Figure 5.13. Due to an unidentified largest S2, the position reconstruction of this event fails. Thus it is placed inside the innermost fiducial volume, even though the small S2 signal indicates that its origin could rather be an α interaction from the BiPo-coincidence. Possible data quality cuts on the S2 signals could be very efficient in removing those events, but as already explained in section 5.2.1 these cuts are avoided due to their unknown acceptance on overlapping S2 signals. The S2 condition developed in this work removes this event, providing a very clean event selection.

After this proof of the efficiency of the newly introduced S2 cut, the final result of SR2 is $^{\text{nat}}\text{Kr/Xe} = \left(14\ ^{+8}_{-6}\,(\text{stat}) \pm 1\,(\text{sys})\right)$ ppt. The innermost 34 kg fiducial volume should give the result with the deepest understanding, as no acceptance losses should be present there.

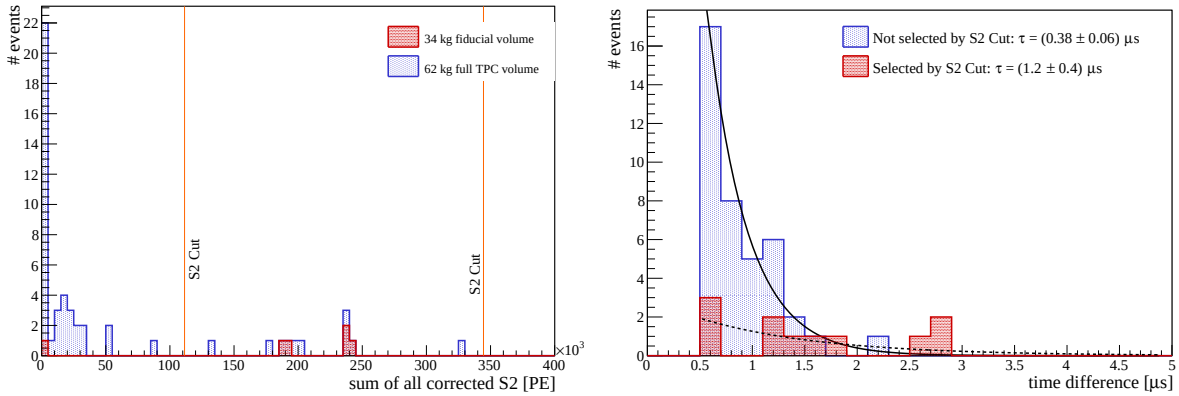

Figure 5.12.: (Left) The energy distribution of the selected events in terms of summed S2 signal strength for the total TPC volume and the innermost 34 kg fiducial volume. (Right) The time distance between the largest and second largest S1 is plotted for all events passing the τ, β and γ criteria. The events which not pass the S2 condition are displayed in blue and the events which pass the S2 condition are shown in red. The black lines indicate exponential fits.

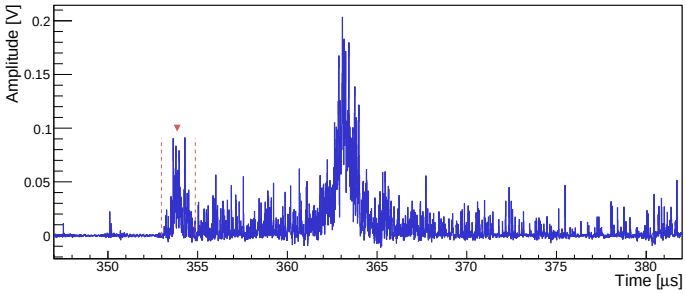

Figure 5.13.: The summed waveform registered by the raw data processor of the XENON100 experiment of the event xe100_110625_1131_000115 173 removed by the S2 condition. The raw data processor did not identify the largest S2 peak, thus the position reconstruction applied could be wrong. For this reason this event with a very weak S2 signal and therefore likely to be a misidentified BiPo-coincidence is located inside the innermost fiducial volume.

The uncertainties are assumed to be Poisson like due to the observed low statistics and the confidence intervals are calculated using the method of [78] assuming a background free event selection.

5.4.2. SR3

The third science run of the XENON100 experiment started dark matter data taking in April 2013 and lasted untill January 2014. Several RGMS measurements of the krypton content were performed for this run. Due to the presence of an air leak in the gas system, additional krypton was introduced to the LXe since May 2013. The averaged krypton concentration was calculated in section 4.1.2 to (6.2 ± 1.0) ppt. This value is of the same magnitude as for SR2. As well during this run a higher ^{222}Rn decay rate is expected due to the presence of the air

leak. Thus, a similar event distribution as in SR2 is expected for this run.

First, the selection cuts have to be adopted to SR3 conditions. According to [77] the overall reference light yield of this run is determined to $\mathcal{L}_y\,(122\text{keV}\,\gamma) = (2.28 \pm 0.04)$ PE/keV, the same value as for SR2. This is expected since the conditions such as xenon purity did not change between these two runs. Thus, the same cut thresholds for the β and γ conditions are applied. The S2 amplification of 662 keV γ rays from ^{137}Cs was determined to be slightly lower as in SR2 with (357 ± 3) PE/keV.

The resulting event distribution is shown in Figure 5.14. Once again the good BiPo-coincidence rejection power of the S2 cut is demonstrated, as an increased population of events at the edges of the TPC is removed. The final result of the innermost 34 kg fiducial volume is $^{\text{nat}}\text{Kr/Xe} = \left(20\,^{+12}_{-9}\,(\text{stat}) \pm 1\,(\text{sys})\right)$ ppt. It deviates 2σ from the value obtained by the RGMS average over the run, which is still a good confirmation of the RGMS measurements.

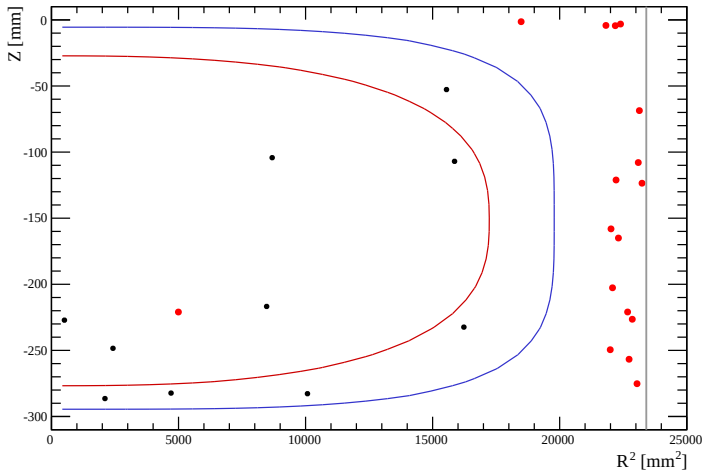

mass [kg]	# events	Kr/Xe [ppt]
34 kg	5	20^{+12}_{-9}
48 kg	8	29^{+11}_{-9}
62 kg	11	22^{+9}_{-7}

Figure 5.14.: (Left) The observed event distribution inside the XENON100 TPC of selected ^{85}Kr delayed coincidence events after application of all selection cuts including the condition on the S2 signal. Events in red are removed by the S2 cut only. 5 events in the innermost fiducial volume pass all selection criteria. (Right) Results.

A closer look into the S2 spectrum of the selected events is shown in Figure 5.15 (left). Two out of the five selected events of the innermost 34 kg fiducial volume have a very high summed S2 signal, although they are still inside the 5σ predefined region. Such events are already observed in SR1 and SR2. The S2 distribution is plotted for all three science runs combined in Figure 5.15 (right).

The signal in PE is used as the scale for the x-axis, although the absolute and comparable energy scale depends on the charge yield of the specific run. But as the differences are just a $\sim$3 % effect, this is only of minor impact. In this approximated comparison it can be seen that the few events with a very large summed S2 signal are are separated by a huge gap with no events from the bulk of events expected from ^{85}Kr delayed coincidences. Thus this population, which deviates more than 4σ from the energy window of $[514, 687]$ keV$_{ee}$, could

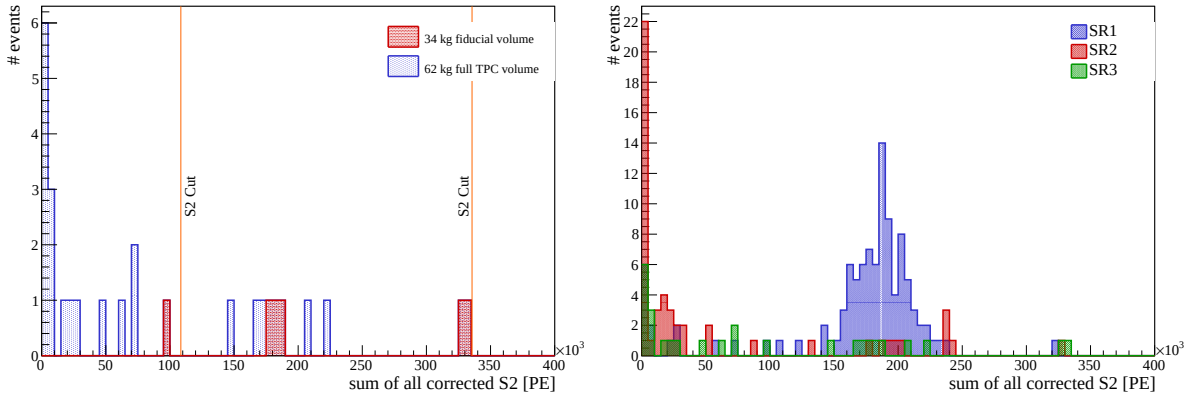

Figure 5.15.: (Left) The energy distribution of the selected events in terms of summed S2 signal strength for the total TPC volume and the innermost 34 kg fiducial volume for SR3 data. (Right) The summed S2 spectrum of the total TPC volume combined for all three science runs. A tiny population at very high summed S2 signals is observed and clearly distinct from the bulk of ^{85}Kr delayed coincidence events. The origin of this population however remains unknown.

be of a different origin. A close inspection of the waveforms shows no anomalies. Note that ignoring this population at high S2 sizes would have a major impact on the SR3 analysis, because the two events occur in the innermost fiducial volume, pushing down the result to $^{\text{nat}}\text{Kr/Xe} = \left(12\,^{+9}_{-8}\,(\text{stat}) \pm 1\,(\text{sys})\right)$, which is much closer to the value expected from the RGMS measurements. But as long as no physical explanation for considering these events as background exists, they are interpreted as valid ^{85}Kr delayed coincidence events.

5.4.3. Comparison with RGMS results: Search for time clustering of events in SR2 and SR3

The results of this delayed coincidence analysis agreed well with the off-line analytics of the RGMS set-up, presented in chapter 3 and chapter 4. An overview of this comparison will be given in chapter 6, illustrated nicely in Figure 6.1. An additional check of consistency between the RGMS results and the ^{85}Kr delayed coincidence analysis can be done by comparing the appearance of the ^{85}Kr delayed coincidence events with the expectations from section 4.1.2. Tiny air leaks in SR2 and SR3 could be reflected in more ^{85}Kr delayed coincidence events towards the end of the specific run, as the overall krypton level was increasing with time. In Figure 5.16 the time distribution of the selected events is plotted for SR2 and SR3 together with the evolution of the krypton concentration estimated in section 4.1.2.

The observed events were binned into periods of one month and in order to increase statistics all valid ^{85}Kr events of the 48 kg fiducial volume were used. The hypothesis of a very slight increase expected from the observation of the radon level inside the detector for SR2 and SR3, done in section 4.1.2, cannot be verified by any observed time-dependent clustering of the selected events. But this is already expected from the very low statistics of the ^{85}Kr

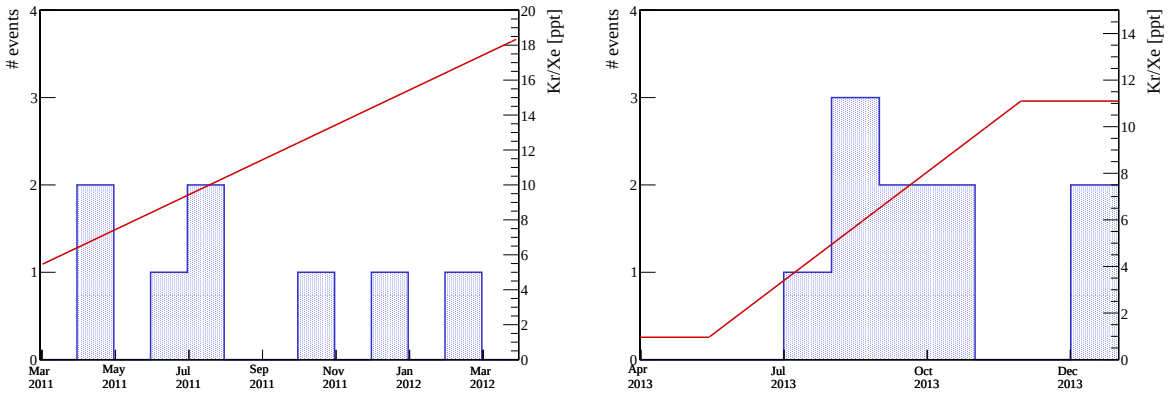

Figure 5.16.: (Left) The timestamp of the selected ^{85}Kr delayed coincidence events in the 48 kg fiducial volume of SR2 is shown, together with the expectation for the krypton evolution estimated in section 4.1.2. (Right) The same distribution for SR3, as well underlined with the expectation for the evolution from section 4.1.2.

analysis for SR2 and SR3. The measured monthly rates get too low in order to infer any statistical significant increase in rate due to the increase in krypton concentration.

6. Summary and Outlook

This Master thesis is put forward in the context of the XENON dark matter search experiments. It deals with one of the main background sources of the experiments: the man-made krypton isotope ^{85}Kr. As an almost pure β emitter its disintegration signals could leak into the expected dark matter signal region, if krypton is present in a too high concentration. Moreover, it is an intrinsic background, distributed homogeneously in the xenon inventory and not affected by fiducial volume selections which use the high self-shielding capacity of LXe. For the design goals of the XENON100 and XENON1T experiments, a reduction of the krypton in xenon concentration down to tens of ppt (XENON100) or hundreds of ppq (XENON1T) is necessary. This is approached by the collaboration by cryogenic distillation of commercially available xenon (purity in the ppm or ppb regime). Equally important are the corresponding analytics, giving the opportunity to check the performance of any purification system and monitoring the operating conditions of the detectors.

In chapter 2 a brief explanation of the astrophysical and cosmological evidences for the existence of dark matter and a presentation of the XENON dark matter search experiments is given. Additionally, the effect of the ^{85}Kr background is characterized. It is shown that the almost constant ratio of ^{85}Kr/$^{\mathrm{nat}}$Kr allows a ^{85}Kr concentration determination by measuring only the stable krypton isotopes.

Chapter 3 introduces in one possible technique of measuring the $^{\mathrm{nat}}$Kr concentration in xenon: the RGMS set-up at MPIK in Heidelberg. This off-line krypton analytics system is based on a combination of a cryogenic gas-chromatographic pre-separation device and an analyzing sector field mass spectrometer. The assay of xenon samples is described, showing major improvements on the signal stability. A relative uncertainty for a single RGMS measurement of 17.2 % is determined, almost limited by the systematics only. A reduction of the RGMS background, estimated by the procedure blank, down to $(0.013 \pm 0.003) \cdot 10^{-12}$ ccmSTP ^{nat}Kr is reported. This results in the so far unprecedented sensitivity limit of the device at the level of 3 ppq.

In chapter 4, xenon assay results are presented. The very stable operating conditions of the RGMS allowed to monitor the latest science run of the XENON100 experiment with several samples. An increasing krypton concentration was observed, which helped to identify an air leak in the gas system of the detector. This increase is even be linked to an observed higher radon rate during this run, giving the possibility to correlate the radon and krypton evolution in the presence of an air leak. This results in an estimate of the krypton evolution during the

225 live-days science run [25], although only one krypton measurement is available. This evolution is considered in an analysis searching for a modulation of the electronic recoil rate [39]. Moreover, the study of several krypton distillation runs by sample taking at the distillation column is shown. This results in a measurement of the lowest krypton in xenon concentration achieved so far by the XENON100 distillation column of (0.64 ± 0.11) ppt. Furthermore, the purification yield is determined three times for the same column, showing a maximum value of $y_p = (390 \pm 120)$. The measurements additionally indicate difficulties to reach concentrations lower than ~ 0.5 ppt with the current set-up of the XENON100 column. The demonstrator column of the XENON1T experiment was examined the same way. Here a purification yield of $y_p > 4500$ at 90 % C.L. is found. Moreover, the sample taken at the output of the column was measured to contain the very low value of < 26 ppq at 90 % C.L., which is to our knowledge the highest xenon purity in regard of krypton concentrations ever achieved and measured. The six measurements carried out at these low concentrations very close to the detection limit of the mass spectrometer agreed well within their statistical uncertainties. One batch was processed with a smaller batch size, resulting in a measurement comparable to the procedure blank. This assures that the estimation of the background for the RGMS by procedure blanks is a valid approach. It could be further concluded that systematic effects as residual krypton contributions from vacuum surfaces start to dominate in the ppq-regime and have to be studied further.

In the last part of this thesis, chapter 5, another krypton in xenon measurement technique is presented. This in-situ analysis searches in the available XENON100 datasets for delayed coincidence events of the secondary decay branch of the ^{85}Kr decay. By tagging the subsequent emission of a β particle and a γ ray delayed by a lifetime of $\tau = 1.46$ μs, ^{85}Kr disintegrations can be identified allowing to quantify the krypton concentration inside the XENON100 experiment. This work improves previous delayed coincidence studies, resulting in a more homogeneous response, quantifying systematic effects and increasing the background rejection power. Good agreement is reached for all science runs of the XENON100 experiment. This proofs that the absolute calibration of the RGMS system is correct within the quantified 16.5 % systematic uncertainty.

In Figure 6.1 the final results of the delayed coincidence analysis are compared to the RGMS measurements of chapter 4. It shows the increase in purity achieved by the XENON100 collaboration between the different science runs. This is only reached due to the feedback to the experimentalists from the two krypton in xenon measurement techniques.

The RGMS method has a low relative uncertainty of 17.2 % for a single measurement, mostly dominated by the 16.5 % systematic uncertainty of the absolute calibration. Thus, the RGMS measurements give very precise results especially for low concentrations. Here limited statistics start to reduce the precision of the in-situ delayed coincidence analysis. Furthermore the off-line RGMS technique always represents the detector status at the specific

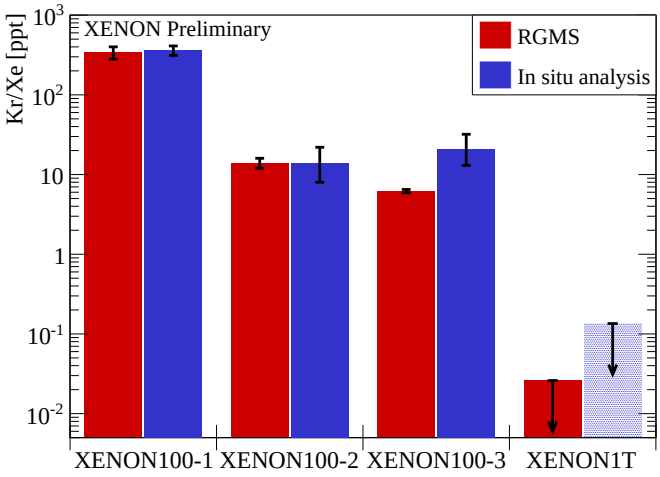

Figure 6.1.: The results of this analysis and the off-line analytics method for the three different science runs of the XENON100 experiment are compared. Furthermore an outlook for the XENON1T experiment is given, comparing the achieved krypton concentration by the new distillation column and the sensitivity limit of this analysis applied to the conditions of XENON1T.

time of sample taking, whereas the in-situ method only can give an averaged concentration for a hole run. This is demonstrated by the reconstruction of the krypton evolution by the RGMS measurement of several samples during the third science run of the XENON100 experiment. In contrast, the limited statistics of the delayed coincidence analysis prevent any statement about the time evolution of the krypton concentration.

Finally an outlook for the XENON1T experiment is shown in Figure 6.1. The achieved krypton concentration of the Münster distillation column, see section 4.2, is compared to the expected limit of sensitivity of the delayed coincidence analysis for the XENON1T experiment. The latter is calculated assuming zero observed delayed coincidence events in 1 tonne·year of data. At 90 % C.L. this corresponds to an expected downward fluctuation of a Poisson distribution with a mean of 3 events, which translates to the sensitivity limit of 135 ppq. This again shows the advantage of the RGMS: A sensitivity two orders of magnitude lower is achieved by this off-line method. Moreover, already one sample in this regime has been measured as displayed in Figure 6.1.

The availability of additional ultra pure xenon samples supplied by the nicely performing XENON1T distillation column will further improve the understanding of the RGMS system at concentrations close to its detection limit. Doping xenon samples below the detection limit with precise amounts of krypton in the ppq-regime could finally verify that the absolute calibration still holds for the very low krypton concentrations and proof the linearity of the complete system, including the gas-chromatographic separation procedure.

Finally, the importance of the RGMS system for the upcoming XENON1T experiment has

to be underlined. XENON1T is under construction since summer 2013 and its first commissioning is planned for 2015. Then the possibility to check the achieved conditions during distillation, detector filling and first test runs with the RGMS will become absolutely mandatory, as no other analytics method so far showed the sensitivity to such low concentrations. During this work the RGMS however proofed the potential of the new distillation column and demonstrated that the system is able to assay xenon samples with the krypton concentrations expected for XENON1T. This sets the basis for a successful dark matter search with XENON1T in regard of the dangerous intrinsic ^{85}Kr background.

A. RGMS Results - Overview

Name	Sampling date	Kr/Xe [ppt]		
SR1-1 [52]	20/06/2010	**340**	±	**60**
SR2-1 [52]	17/11/2011	**14**	±	**2**
KC2-In [45]	08/12/2011	**2800**	±	**500**
KC1-Out [45]	25/09/2012	**0.97**	±	**0.19**
KC1-In	01/10/2012	**123**	±	**21**
KC2-Out [45]	04/11/2012	**7.0**	±	**1.7**
SR3-1 [52]	14/12/2012	**0.71**	±	**0.22**
SR3-2	09/01/2013	**0.95**	±	**0.16**
SR3-ATTA	30/09/2013	**435**	±	**79**
SR3-3	21/10/2013	**8.7**	±	**1.5**
SR3-4	22/12/2013	**11.1**	±	**1.9**
KC3-Out	06/02/2014	**0.64**	±	**0.11**
KC3-In/SR3-Rec	10/02/2014	**25.7**	±	**4.3**
SR4-Fill1	12/02/2014	**2015**	±	**335**
MS-LiquidOut	27/02/2014	$<$ **0.026**	**at**	**90 % C.L.**
MS-InGas	27/02/2014	**136**	±	**22**
SR4-Fill2	28/03/2014	**1.4**	±	**0.3**

Table A.1.: Overview over the final results of all RGMS measurements relevant for this work in chronological order. The prefix SR indicates that this was a sample taken during a ongoing science run of the XENON100 experiment. The prefix KC indicates that the sample was taken in the context of the evaluation of the performance of the XENON100 distillation column. The prefix MS indicates that the sample was taken from the first XENON1T demonstrator column built by the Münster group of the collaboration. Measurements marked with a citation were not measured during this work but in the corresponding citation.

Bibliography

[1] F. Zwicky, "Die Rotverschiebung von extragalaktischen Nebeln," *Helvetica Physica Acta* **6** (1933) 110.

[2] V. Rubin, N. Thonnard, and W. F. Jr., "Extended rotation curves of high-luminosity spiral galaxies. IV - Systematic dynamical properties, SA through SC," *Astrophys. J.* **225** (1978) 107.

[3] K. G. Begeman, A. H. Broeils, and R. H. Sanders, "Extended rotation curves of spiral galaxies: dark haloes and modified dynamics," *Monthly Notices of the Royal Astronomical Society* **249** (1991) 523.

[4] A. Einstein, "Über den Einfluß der Schwerkraft auf die Ausbreitung des Lichtes," *Annalen der Physik* **340** (1911) 898.

[5] F. Dyson, A. Eddington, and C. Davidson, "A Determination of the Deflection of Light by the Sun's Gravitational Field, from Observations Made at the Total Eclipse of May 29, 1919," *Philosophical Transactions of the Royal Society of London A* **220** (1920) 291.

[6] F. Zwicky, "On the Masses of Nebulae and of Clusters of Nebulae," *Astrophys. J.* **86** (1937) 217.

[7] D. Clowe, M.Bradač, A. Gonzalez, M. Markevitch, S. Randall, C.Jones, and D. Zaritsky, "A Direct Empirical Proof of the Existence of Dark Matter," *Astrophys. J.* **648** (2006) 109, `arXiv:astro-ph/0608407`.

[8] D.Fixsen, "The Temperature of the Cosmic Microwave Background," *Astrophys. J.* **707** (2009) 916, `arXiv:0911.1955`.

[9] **Planck** Collaboration, P. Ade *et al.*, "Planck 2013 results. I. Overview of products and scientific results," `arXiv:1303.5062`.

[10] **Planck** Collaboration, P. Ade *et al.*, "Planck 2013 results. XVI. Cosmological parameters," `arXiv:1303.5076`.

[11] V. Springel, C. Frenk, and S. White, "The large-scale structure of the Universe," *Nature* **440** (2006) 1137, `arXiv:astro-ph/0604561`.

[12] **MACHO** Collaboration, C. Alcock *et al.*, "The MACHO project: Microlensing results from 5.7 years of LMC observations," *Astrophys. J.* **542** (2000) 281, arXiv:astro-ph/0001272.

[13] M. Milgrom, "A Modification of the Newtonian dynamics as a possible alternative to the hidden mass hypothesis," *Astrophys. J.* **270** (1983) 365.

[14] J. R. Bond, G. Efstathiou, and J. Silk, "Massive Neutrinos and the Large-Scale Structure of the Universe," *Phys. Rev. Lett.* **45** (1980) 1980.

[15] G. Gelmini and P. Gondolo, "Dark matter production mechanisms.". From Particle Dark Matter, G. Bertone, ed., ch. 7. Cambridge University Press, 2010.

[16] D. G. Cerdeño and A. M. Green, "Direct detection of WIMPs.". From Particle Dark Matter, G. Bertone, ed., ch. 7. Cambridge University Press, 2010.

[17] L. M. Widrow, B. Pym, and J. Dubinski, "Dynamical Blueprints for Galaxies," *Astrophys. J.* **679** (2008) 1239, arXiv:0801.3414.

[18] **RAVE** Collaboration, M. C. Smith *et al.*, "The RAVE survey: constraining the local Galactic escape speed," *MNRAS* **379** (2007) , arXiv:astro-ph/0611671v2.

[19] N. Evans, C. Carollo, and P. de Zeeuw, "Triaxial Haloes and Particle Dark Matter Detection," *MNRAS* **318** (2000) , arXiv:astro-ph/0008156.

[20] G. Plante, "The XENON100 Dark Matter Experiment: Design, Construction, Calibration and 2010 Search Results with Improved Measurement of the Scintillation Response of Liquid Xenon to Low-Energy Nuclear Recoils," PhD thesis, Columbia University, 2012.

[21] M. Schumann, "Dark Matter Search with liquid Noble Gases," arXiv:1206.2169.

[22] **XENON10** Collaboration, J. Angle *et al.*, "First Results from the XENON10 Dark Matter Experiment at the Gran Sasso National Laboratory," *Phys. Rev. Lett.* **100** (2008) 021303, arXiv:0706.0039.

[23] **XENON100** Collaboration, E. Aprile *et al.*, "The XENON100 dark matter experiment," *Astroparticle Physics* **35** (2012) 573, arXiv:1107.2155v2.

[24] **XENON100** Collaboration, E. Aprile *et al.*, "Dark Matter Results from 100 Live Days of XENON100 Data," *Phys. Rev. Lett.* **107** (2011) 131302, arXiv:1104.2549v3.

[25] **XENON100** Collaboration, E. Aprile *et al.*, "Dark Matter Results from 225 Live Days of XENON100 Data," *Phys. Rev. Lett.* **109** (2012) 181301, arXiv:1207.5988v2.

[26] **LUX** Collaboration, D. S. Akerib *et al.*, "First Results from the LUX Dark Matter Experiment at the Sanford Underground Research Facility," *Phys. Rev. Lett.* **112** (2014) 091303, arXiv:1310.8214v2.

[27] E. Aprile and T. Doke, "Liquid xenon detectors for particle physics and astrophysics," *Rev. Mod. Phys.* **82** (2010) 2053, arXiv:0910.4956v1.

[28] A. Lansiart, A. Seigneur, J.-L. Moretti, and J.-P. Morucci, "Development research on a highly luminous condensed xenon scintillator," *Nucl. Instrum. Meth.* **135** (1976) 47.

[29] **XENON100** Collaboration, E. Aprile *et al.*, "Material screening and selection for xenon100," *Astroparticle Physics* **35** (2011) 43, arXiv:1103.5831v2.

[30] **MACRO** Collaboration, M. Ambrosio *et al.*, "Vertical muon intensity measured with MACRO at the Gran Sasso laboratory," *Phys. Rev. D* **52** (1995) 3793.

[31] **XENON100** Collaboration, E. Aprile *et al.*, "Likelihood approach to the first dark matter results from XENON100," *Phys. Rev. D* **84** (2011) 052003, arXiv:1103.0303.

[32] **XENON100** Collaboration, E. Aprile *et al.*, "Limits on Spin-Dependent WIMP-Nucleon Cross Sections from 225 Live Days of XENON100 Data," *Phys. Rev. Lett.* **111** (2013) 021301, arXiv:1301.6620.

[33] M. Dine, W. Fischler, and M. Srednicki, "A Simple Solution to the Strong CP Problem with a Harmless Axion," *Phys. Lett. B* **104** (1981) 199.

[34] L. Visinelli and P. Gondolo, "Dark Matter Axions Revisited," *Phys. Rev. D* **80** (2009) 035024, arXiv:0903.4377.

[35] **XENON100** Collaboration, E. Aprile *et al.*, "First Axion Results from the XENON100 Experiment," arXiv:1404.1455.

[36] **DAMA/LIBRA** Collaboration, "Final model independent result of DAMA/LIBRA–phase1," *Eur. Phy. J. C* **73** (2013) 2648, arXiv:1308.5109.

[37] **CoGeNT** Collaboration, C. E. Aalseth *et al.*, "Search for an Annual Modulation in a p-Type Point Contact Germanium Dark Matter Detector," *Phys. Rev. Lett.* **107** (2011) 141301, arXiv:1106.0650.

[38] **CoGeNT** Collaboration, C. Aalseth *et al.*, "Search for An Annual Modulation in Three Years of CoGeNT Dark Matter Detector Data," arXiv:1401.3295.

[39] **XENON100** Collaboration, "Search for periodic rate variations in XENON100." In preparation.

[40] **SuperCDMS** Collaboration, A. Anderson *et al.*, "Constraints on Light WIMPs from SuperCDMS," `arXiv:1405.4210`.

[41] **XENON1T** Collaboration, E. Aprile *et al.*, "The XENON1T Dark Matter Search Experiment," `arXiv:1206.6288`.

[42] **XENON1T** Collaboration, E. Aprile *et al.*, "Conceptual design and simulation of a water Cherenkov muon veto for the XENON1T experiment," `arXiv:1406.2374`.

[43] J. Bieringer, C. Schlosser, H. Sartorius, and S. Schmid, "Trace analysis of aerosol bound particulates and noble gases at the BfS in Germany," *Applied Radiation and Isotopes* **67** (2009) 672.

[44] S. Lindemann, "Reinigung und Nachweis von Edelgasen mit miniaturisierten Proportionalzählrohren," Master thesis, Universität Heidelberg, 2009.

[45] S. Lindemann, "Intrinsic 85 Kr and 222 Rn Backgrounds in the XENON Dark Matter Search," PhD thesis, Max-Planck-Institut for Nuclear Physics Heidelberg, 2013.

[46] X. Du, R. Purtschert, K. Bailey, B. E. Lehmann, R. Lorenzo, Z.-T. Lu, P. Mueller, T. P. O'Connor, N. C. Sturchio, and L. Young, "A new method of measuring 81Kr and 85Kr abundances in environmental samples," *Geophysical Research Letters* **30** (2003) , `arXiv:physics/0311118`.

[47] **XENON100** Collaboration, E. Aprile *et al.*, "Analysis of the XENON100 dark matter search data," *Astroparticle Physics* **54** (2014) 11, `arXiv:1207.3458`.

[48] R. B. Firestone, V. S. Shirley, C. M. Baglin, S. F. Chu, and J. Zipkin, *Table of Isotopes, vol. I.* John Willey and Son, 1996.

[49] W. McCabe and J. Smith, *Unit Operations of Chemical Engineering.* 3rd Edition, McGraw-Hill, 1976.

[50] **XMASS** Collaboration, K. Abe *et al.*, "Distillation of liquid xenon to remove krypton," *Astroparticle Physics* **31** (2009) 290, `arXiv:0809.4413`.

[51] E. Aprile, T. Yoon, A. Loose, L. W. Goetzke, and T. Zelevinsky, "An atom trap trace analysis system for measuring krypton contamination in xenon dark matter detectors," *Review of Scientific Instruments* **84** (2013) , `arXiv:1305.6510`.

[52] S. Lindemann and H. Simgen, "Krypton assay in xenon at the ppq level using a gas chromatographic system and mass spectrometer," *Eur. Phy. J. C* **74** (2014) 1, `arXiv:1308.4806`.

[53] J. Hopp, M. Trieloff, and R. Altherr, "Noble gas compositions of the lithospheric mantle below the Chyulu Hills volcanic field, Kenya," *Earth and Planetary Science Letters* **261** (2007) 635.

[54] H. Simgen and G. Zuzel, "Ultrapure gases — from the production plant to the laboratory," *AIP Conference Proceedings* **897** (2007) 45–50.

[55] J. Hopp. Private Communication.

[56] "Determination of the characteristic limits (decision threshold, detection limit and limits of the confidence interval) for measurements of ionizing radiation – fundamentals and application," 2010. ISO 11929:2010.

[57] W. Wentworth, S. Vasnin, S. Stearns, and C. Meyer, "Pulsed discharge helium ionization detector," *Chromatographia* **34** (1992) 219.

[58] S. Vasnin, W. Wentworth, S. Stearns, and C. Meyer, "Pulsed discharge emission detector — application to analytical spectroscopy of permanent gases," *Chromatographia* **34** (1992) 226.

[59] D. Forsyth, "Pulsed discharge detector: theory and applications," *Journal of Chromatography A* **1050** (2004) 63.

[60] H. Simgen *et al.*, "Detection of 133Xe from the Fukushima nuclear power plant in the upper troposphere above Germany," *Journal of Environmental Radioactivity* **132** (2014) 94, `arXiv:1309.1618`.

[61] S. Rosendahl, "Xenon purification for the XENON1T dark mater search." PhD thesis, Westfälische Wilhelms Universität, Münster, expected for 2014.

[62] A. Loose. Private communication.

[63] M. Weber, "Gentle Neutron Signals and Noble Background in the XENON100 Dark Matter Search Experiment," PhD thesis, Max-Planck-Institut for Nuclear Physics Heidelberg, 2013.

[64] M. Weber. Private Communication.

[65] **LUX** Collaboration, Akerib, D. S. and others, "Radiogenic and Muon-Induced Backgrounds in the LUX Dark Matter Detector," `arXiv:1403.1299`.

[66] R. Brun and F. Rademakers, "ROOT — An object oriented data analysis framework," *Nucl. Inst. Meth. A* **389** (1997) 81.

[67] **XENON10** Collaboration, E. Aprile *et al.*, "Design and performance of the XENON10 dark matter experiment," *Astroparticle Physics* **34** (2011) 679, `arXiv:1001.2834`.

[68] M. Szydagis *et al.*, "NEST: a comprehensive model for scintillation yield in liquid xenon," *Journal of Instrumentation* **6** (2011) P10002, arXiv:1106.1613.

[69] M. Szydagis, A. Fyhrie, D. Thorngren, and M. Tripathi, "Enhancement of NEST capabilities for simulating low-energy recoils in liquid xenon," *Journal of Instrumentation* **8** (2013) C10003, arXiv:1307.6601.

[70] G. Plante *et al.*, "New measurement of the scintillation efficiency of low-energy nuclear recoils in liquid xenon," *Phys. Rev. C* **84** (2011) 045805, arXiv:1104.2587.

[71] A. Manzur *et al.*, "Scintillation efficiency and ionization yield of liquid xenon for monoenergetic nuclear recoils down to 4 keV," *Phys. Rev. C* **81** (2010) 025808, arXiv:0909.1063.

[72] J. H. Hubbell and S. M. Seltzer, "Tables of X-ray mass attenuation coefficients and mass energy-absorption coefficients 1 keV to 20 MeV for elements Z=1 to 92 and 48 additional substances of dosimetric interest," Tech. Rep. NISTIR-5632, 1995.

[73] **GEANT4** Collaboration, S. Agostinelli *et al.*, "Geant4—a simulation toolkit," *Nucl. Inst. Meth. A* **506** (2003) 250.

[74] T. Marrodán-Undagoitia. Private Communication.

[75] **XENON100** Collaboration, E. Aprile *et al.*, "Observation and applications of single-electron charge signals in the XENON100 experiment," *Journal of Physics G: Nuclear and Particle Physics* **41** (2014) 035201, arXiv:1311.1088.

[76] A. Rizzo. Private Communication.

[77] L. Rauch, "Detector characterization, electronic-recoil energy scale and astrophysical independent results in XENON100," Master thesis, Universität Heidelberg, 2014.

[78] G. J. Feldman and R. D. Cousins, "Unified approach to the classical statistical analysis of small signals," *Phys. Rev. D* **57** (1998) 3873, arXiv:physics/9711021.

Danksagung

Als erstes möchte ich Prof. Dr. Manfred Lindner danken für die Möglichkeit diese Arbeit auszuführen und Teil der XENON Kollaboration zu werden. Darüber hinaus bin ich sehr dankbar für seine Unterstützung mein Wissen auf spannenden Konferenzen und Meetings zu erweitern. Ein Dank geht auch an Prof. Dr. André Schöning für die Zweitkorrektur dieser Arbeit. Ganz besonders hervorheben möchte ich Dr. Sebastian Lindemann, der mir die Schönheit des RGMS gezeigt hat, darüberhinaus stets mit Rat zur Seite war und mir sämtliche Tricks beigebracht hat wie man mit dem *alten Ding* umzugehen hat.

Zusätzlich möchte ich mich bei der gesamten XENON Gruppe des MPIK bedanken, allen voran bei Dr. Teresa Marrodán-Undagoitia für die Hilfe bei der Lösung aller Schwierigkeiten, die eine komplizierte Datenanalyse erfordert und bei Dr. Hardy Simgen für sein offenes Ohr bei allen Fragen und der wunderbaren Einführung in die Welt der Gas-Analytik. Darüber hinaus seien vor allem meine Mitstudenten der Arbeitsgruppe Stefan Brünner, Meike Danisch, Constanze Hasterock, Ludwig Rauch und Natascha Rupp genannt, da mir durch sie stets klar geworden ist, dass wir alle die gleichen Probleme haben und Physik auch nur dann spannend ist, wenn man sie zusammen macht! Des Weiteren sind es vor allem Dr. Gerd Heusser und Dr. Marc Weber denen ein großer Dank gilt, da sie bei mir das Interesse an der Low-Level Physik geweckt haben. Ich werde die vielen Bleiziegel, die ich für GIOVE aufeinander gesetzt habe, immer in guter Erinnerung behalten.

Natürlich muss auch die ganze XENON Kollaboration genannt werden, die selbst dann noch mit Hilfe beiseite steht, wenn in langen Telefonkonferenzen ganz zum Schluss eine Krypton-Analyse präsentiert wird. Hervorheben möchte ich hier auch Stephan Rosendahl, sowie die ganze XENON Münster-Gruppe für die einzigartige Möglichkeit das sauberste Xenon der Welt vermessen zu können!

Zu guter Letzt gibt es aber auch noch zahllose Menschen abseits der Physik, die für mich unersetzlich sind und ohne die ich so eine Arbeit nie hätte anfertigen können. Durch mein Studium wurde ich von großartigen Leuten begleitet und unterstützt: Deshalb ein sehr großer Dank an Matthias Wimmer und die conduction band (Jan Nasse, Phillip Kreyenberg, Marian Weiss und Therese Weißbach)! Ein Dankeschön an meine Mitbewohnerinnen für die entspannte Atmosphäre zu Hause. Vor allem aber danke ich Christin Grote für ihre unendlich liebevolle Ablenkung von sämtlichen physikalischen Themen im letzten Jahr. Der letzte Dank geht an meinen Bruder Matthias und insbesondere an meine Eltern, Klemens und Angelika, für eine unglaubliche Unterstützung bei allem was ich je getan habe!

Erklärung:

Ich versichere, dass ich diese Arbeit selbstständig verfasst habe und keine anderen als die angegebenen Quellen und Hilfsmittel benutzt habe.

Heidelberg, den (Datum) .....